ABSTRACT

Title of dissertation: EXTREME PRECIPITATION PROJECTIONS IN A CHANGING CLIMATE

Huiling Hu
Doctor of Philosophy, 2019

Dissertation directed by: Professor Bilal M. Ayyub
Department of Civil and Environmental Engineering

Global climate is changing at an alarming rate, with an increase in heat waves, wildfires, extreme weather events, and rising sea levels, which could cost the United States billions of dollars in lost labor, reduced crop yields, flooding, health problems, and crumbling infrastructure. Reports by hundreds of US climate scientists from 13 federal agencies in the Fourth National Climate Assessment (2018) predict that the US economy will shrink by as much as 10% by the end of the century if global warming continues with current trends. Extreme precipitation, in particular, has led to significant damage through flooding, bridge scouring, land-slides, etc.; therefore, it is critical to develop accurate and reliable methods for future extreme precipitation projection. This dissertation proposes new methods of improved projections of such extremes by appropriately accounting for a changing climate.

First, this dissertation studies how to model extreme precipitation using Markov Chains and dynamic optimization. By incorporating day-to-day serial dependency and dynamic optimization, the model improves the accuracy of extreme precipita-

tion analysis significantly.

The dissertation also examines future projections of extreme precipitation. State-of-the-art methods for future precipitation projections are based on downscaled Global Climate Models (GCMs), which are not always accurate for extreme precipitation projection. This work studies accuracy when using downscaled GCMs for extreme precipitation and designed new methods based on copulas to improve the accuracy.

Finally, the above methods are applied to the analysis of future trends of intensity-duration-frequency (IDF) curves, which, in turn, have extensive applications in designing drainage systems. To incorporate geographic influence on local areas, a machine-learning-based solution is proposed and validated. The results show that the gradient boosting tree can be used to accurately project future IDF curves for short durations. It is also projected that short-duration intensity will increase up to 23% for the selected representative stations in this century.

In summary, this dissertation systemically studies different aspects of improvements and applications of extreme precipitation projection. By using mathematical models, such as copula and Markov Chains as well as various machine-learning models (i.e., gradient boosting tree), extreme precipitation projection can be made significantly more reliable for use.

EXTREME PRECIPITATION PROJECTIONS IN A CHANGING CLIMATE

by

Huiling Hu

Dissertation submitted to the Faculty of the Graduate School of the
University of Maryland, College Park in partial fulfillment
of the requirements for the degree of
Doctor of Philosophy
2019

Advisory Committee:
Professor Bilal M. Ayyub, Chair/Advisor
Professor Michelle Bensi
Professor Michael Kearney, Dean's Representative
Professor Brian Phillips
Professor Allison Reilly

Acknowledgments

I would like to express my gratitude to my advisor Dr. Bilal Ayyub, who has been incredibly supportive and has guided me continuously throughout my Ph.D. with great advice. His views and attitude on research and teaching have shaped my perspective on how to do research. He has been very patient especially when I encountered some research obstacles and constantly encouraged me to try different approaches to solve them. It is his belief in my ability that finally made this dissertation happen.

I also want to thank the dissertation committee members, Dr. Michelle Bensi, Dr. Michael Kearney, Dr. Brian Phillips, and Dr. Allison Reilly, for their time and valuable suggestions that significantly improved this dissertation.

Table of Contents

List of Tables

List of Figures

List of Abbreviations

ASCE	American Society of Civil Engineers
BCCA	Bias Corrected Constructed Analogue
BCSD	Bias Corrected Spatial Downscaling
CA	Constructed Analogue
CDF	Cumulative Distribution Function
CMIP	Coupled Model Intercomparison Project
CWD	Maximum number of consecutive wet days within a year
EM	Expectation Maximization
ENSOI	El Nino Southern Oscillation Index
ESGF	Earth System Grid Federation
ETCCDMI	Expert Team on Climate Change Detection and Indices
GBDT	Gradient Boosting Decision Tree
GCM	Global Climate Model
GEV	Generalized Extreme Value
GHG	Greenhouse Gas
IDF curve	Intensity-Duration-Frequency curve
IID	Independent and Identically Distributed
IPCC	Intergovernmental Panel on Climate Change
LLNL	Lawrence Livermore National Laboratory
LOCA	Localized Constructed Analogs
LoS	Level of Service
MACA	Multivariate Adaptive Constructed Analogs
ML	Machine Learning
NASA	National Aeronautics and Space Administration
NCA	National Climate Assessment
NCAR	National Center for Atmospheric Research
NCDC	National Climatic Data Center
NEX-GDDP	NASA Earth Exchange Global Daily Downscaled Projections
NMAE	Normalized Mean Absolute Error
NOAA	National Oceanic and Atmospheric Administration
NRMSE	Normalized Root Mean Square Error
RBF	Radial Basis Function
RCP	Representative Concentration Pathway
SVC	Support Vector Machines

Chapter 1: Introduction

1.1 Background

Global climate is changing at an alarming rate and scale. The recent release of the Fourth National Climate Assessment (NCA) report (2018) [2] alerted the community to the potential risks associated with climate change and the urgency to take action. As part of its conclusions, the report projected that, over the coming century, the increase of extreme climate events would continue and may become more severe. A special report [3] by the Intergovernmental Panel on Climate Change (IPCC), published in 2018, reached the same conclusion: human actives have caused global warming of about 1.2°C compared to the global temperatures prior to industrialization. In addition, the IPCC report further concluded that the impact will climb to 1.2°C in the next 20 to 40 years. Among the factors that contribute to climate change, human activity has dominated, especially since the 1960s. In particular, excessive use of fossil fuels has resulted in a significant increase in greenhouse gas (GHG) emissions, which, in turn, influences precipitation, temperature, etc.

Such an increase in global warming has led to a significant rise in the frequency of extreme weather events and has impacted human property and life in a variety of ways. Billions of dollars and thousands of lives have been lost due to climate

change directly or indirectly [4]. The IPCC also studied, in detail, the trend of extreme climate events in a recent special report [5]. In particular, it showed that extreme climate hazards have led to much more damage compared to the increases in non-extreme climate events. In particular, numerous works show that extreme precipitation is occurring at an increasing rate in recent decades [6, 7, 8, 9]. Such increases of extreme precipitation events have caused serious impacts on societies and the natural environment by means of flooding [10], bridge scouring [11], landsliding [12], the eradication of exotic species [13], etc.

1.2 Objectives and Goals

To be better prepared for future extreme precipitation, it is crucial to obtain accurate and reliable future projections or, in other words, an answer to the following question:

How can we obtain accurate future extreme precipitation projections and use them to improve practical design?

The main objective of this dissertation is to improve methods related to future projections of extreme precipitation. However, climate projection is a complicated topic, involving both theoretical foundation and practical design. Therefore, this dissertation takes a modular approach and studies three questions that can help to find an answer to the above question, namely:

1. *How can we accurately analyze extreme precipitation for a rich set of extreme events?*

2. *How can we conduct future extreme precipitation projection reliably?*

3. *How can we apply extreme precipitation projection to improve practical design?*

These questions are closely related to extreme precipitation projection since each of them corresponds to a different stage toward an answer to the question on how to obtain and apply future extreme precipitation projections to improve design in practice. They can be viewed as stepping stones to the main objective of this dissertation.

1.3 Methodology Review on Extreme Precipitation Research

As discussed in the previous section, there are primarily three questions to address. In the following, a detailed discussed on the background of each question as well as the approach taken in this dissertation are discussed.

1.3.1 Extreme Precipitation Analysis

To obtain an accurate projection of precipitation, it is important to first understand how it behaves and propose models that can be used to analyze its behavior. From a high-level view, there are two main goals in extreme precipitation analysis: 1) Understand the historical trend of extreme precipitation and find anomalies; 2) Use mathematical or empirical methods to summarize the pattern of extreme precipitation. Some previous works have focused on analyzing precipitation in general but not specifically for extreme precipitation [14, 15]. For example, Adler et al. [16] and Silva et al. [17] performed time-history analysis of precipitation data on a monthly

basis. Huffman et al. [18] performed tropical precipitation analysis using satellite data. Barros [19] studied characteristics of precipitation that are induced by mountainous factors. Various distributions are also studied to model precipitation for different areas [20, 21, 22]. However, extreme precipitation has many features that do not otherwise appear: extreme precipitation events are rare; thus, there are scant observations regarding them, even for a long period of time. This means that commonly used analysis methods for precipitation may not be suitable for extreme precipitation.

More recently, many researchers have started to focus on an improved analysis of extreme precipitation. For example, many have focused on trend analysis for maximum extreme precipitation events in different areas [23, 24, 25, 26]. Others proposed different models for extreme precipitation [27, 28, 29]. Min et al. [30] analyzed extreme precipitation of a Northern Hemisphere land area with a focus on its correlation with human activities in recent decades. O'Gorman and Schneider [31] focused on the physical basis of climate models for extreme precipitation analysis. Furthermore, Pfahl et al. [32] studied the regional pattern of extreme precipitation considering both thermodynamics and dynamics factors. Easterling et al. [6] analyzed total rainfall distribution and its tail distribution. Libertino et al. [33] proposed a robust methodology for extreme rainfall estimation with regional-scale analysis. They, again, confirmed that both precipitation and temperature are becoming more extreme due to climate change.

The most popular approach in extreme precipitation analysis is to use generalized extreme value (GEV) analysis for maximum precipitation analysis. More details

of GEV analysis are discussed in Chapter 2. For example, Bertoldo et al. [34] performed GEV analysis on four areas in Italy with different geographic features using 30 years of rain gage data. Cheng et al. [35] performed non-stationary extreme value analysis and return periods using Bayesian inference. Sveinsson et al. [36] studied maximum precipitation distribution assuming that the precipitation distribution is stationary. More recent works improved the analysis by introducing non-stationarity to reflect the effects of climate change [37, 35, 38]. In particular, Jalbert et al. [39] proposed a spatio-temporal model for extreme precipitation based on GEV. Other works focused on performing GEV analysis in various regions [40, 41, 42]. In addition to maximum precipitation, other extreme events have also been proposed, For example, by the Expert Team on Climate Change Detection, Monitoring, and Indices (ETCCDMI).

1.3.2 Extreme Precipitation Projection

Due to the effect of climate change, precipitation is highly non-stationary. This means that the analytical results of historical extreme precipitation may not reflect future extreme precipitation. It is an important and complicated task to make projections of future extreme precipitation. Due to complex climate dynamics as well as the involvement of human activities, future trends of climate change can hardly be directly described by any mathematical model. On the other hand, an accurate projection of future climate, especially future extreme climate, is crucial to mitigate its future risk. To this end, the Coupled Model Intercomparison Project

(CMIP) was initiated to incorporate climate change in the design of GCMs for the next century.

GCMs are climate models that incorporate climate dynamics as well as various emission levels into the analysis. Numerous GCMs have been proposed and studied as part of CMIP [43, 44, 45]. These GCMs provide results for four Representative Concentration Pathways (RCPs), each of which represents one possible GHG emission level in the future. GCM results significantly improve state-of-the-art of climate science. However, there are still important problems that remain unsolved: 1) GCM results provide coarse-grained climate trend at the state level only but not an accuracy projection that requires a fine-grained trend; 2) GCM results present the average climate trend in a large area; therefore, extreme events are less frequent than in reality.

To solve these issues, researchers have been focused on designing different downscaling methods for GCM results. Downscaling from a high-level description is a method that maps global climate trend to a climate trend that is specific to a local area. Downscaling of a GCM model can be achieved roughly by two different methods: 1) dynamic downscaling [46, 47], which refers to the use of high-resolution regional simulations to dynamically extrapolate the effects of large-scale climate processes to a region; 2) statistical downscaling [48, 47], which refers to the use of statistical tools to understand the relationship from global model to a region and apply such transformation to a local area. Due to the stringent requirements of data and computational resources in dynamic downscaling, statistical downscaling has become a more practical approach. Popular statistical downscaling methods in-

clude NASAs Earth Exchange Global Daily Downscaled Projections (NEX-GDDP), Localized Constructed Analogs (LOCA), and Multivariate Adaptive Constructed Analogs (MACA) [49, 50, 51].

1.3.3 Extreme Precipitation Application

Applying the results of extreme precipitation projection to design standards is important, as it can directly impact practice design and reduce the future risks associated with extreme precipitation. One of the most widely used tools in extreme precipitation is the intensity-duration-frequency (IDF) curve. Most of the current risk management solutions for water infrastructures and drainage systems are designed in accordance to the level of service (LoS) as well as the extremity of rainfall, often described by IDF curves [52]. As the name suggests, an IDF curve shows probability in terms of the return period, that a rainfall with an intensity at least i inches per hour occurs for a duration of t minutes. IDF curves are one of the most popular tools to quantify the extremity of rainfall in a region. They are particularly good at representing extreme rainfall for short durations, which is highly relevant in determining the strength of many areas of drainage systems. Due to this, IDF curves have become a standard tool in the design of drainage systems.

Most drainage systems are designed with a long service life-cycle of many decades; however, not all of the designs take into consideration the effects of climate change [53]. Most design standards used in practice for future infrastructure are based on IDF curves computed from historical data, which, essentially, assumes

that climate is stationary. That is, the historical statistics on extreme rainfall remain unchanged for future use. However, such a stationary assumption is becoming more and more ungrounded as human interference in the climate increases: a worsening climate causes more co-occurrences of multiple extreme rainfalls, as well as cascading extreme events, posing an unprecedented risk to existing and future water infrastructures, which can then cause social and economic catastrophes. Therefore, incorporating the instability of climate into the design of IDF curves is both necessary and a popular ongoing work.

1.4 Gaps in Existing Works

Extreme precipitation projection is important and involves research on modeling extreme precipitation, how to perform projection accurately, and how to apply the projection results to real design. Prior works have advanced state-of-the-art solutions to these aspects, which have greatly improved engineering practices and risk reduction in regard to extreme precipitation. However, there are still challenges and gaps in the existing work, prohibiting further improvements. These research gaps as well as solutions to solve them are discussed in detail below.

1.4.1 Gaps in Modeling Extreme Precipitation

Most existing works that study extreme precipitation analysis are based on the GEV method [34, 37, 35, 38]. In GEV analysis, daily precipitations are treated as independent and identically distributed random variables. The maximum value of a

set of these random variables can then be computed precisely if the daily distribution is known. When the maximum is taken over a large number of random variables, the distribution converges to a specific form regardless of the daily precipitation distribution. Such an approach is effective on computing maximum precipitation of a certain duration; however, it may not be as effective in some settings:

1. This method can analyze the maximum precipitation over any length of duration but not other, more complicated events [23, 24, 25]. This is mainly due to the limitation in GEV analysis, which can only analyze the maximum of a set of random variables. However, since precipitation is a complex stochastic process, maximum precipitation may not always be adequate to describe the extremity of precipitation. For example, GEV cannot effectively study the number of continuous rainy days

2. The use of GEV analysis also requires that precipitations from different days follow the same distribution and are independent of each other [34, 35, 40]. This requirement cannot be satisfied in practice. Indeed, it is long observed and studied that daily precipitation is dependent on each other [54, 55, 56, 57, 58]; for example, a heavy rainy day is more likely to occur after another heavy rain day. Although this fact is recognized in some papers, adequate models are unavailable to take this fact into consideration. Some techniques can be used to avoid independence assumption based on sampling, but many works have not applied these methods

3. Another challenge in using GEV analysis is the lack of data for formula fitting.

There are several factors contributing to the lack of data. First, in GEV analysis, only the maximum value of extreme precipitation is used, and all other values are discarded since they are not related to the maximum value distribution. For example, when extreme precipitation is computed annually, one data point can be obtained from each station per year. The underlying cause stems from its fundamental methodology, i.e., these models directly consider the distribution of extreme events Second, GEV analysis is accurate when the number of random variables to be taken is large, due to the nature of its asymptotic analysis. Therefore, even more data is required to ensure that the GEV analysis is applicable As a result, the applicability of GEV analysis is rather limited to those cases with large amounts of data for the same location, which is often difficult to meet.

1.4.2 Gaps in Extreme Precipitation Projection

Due to the high variability of future climate, most existing works for future extreme precipitation projection are based on GCM models, which are, in turn, constructed based on different RCPs. Although these GCMs are accurate on a global scale, the resolution is not sufficient to study a local region. There are many different approaches that can increase the resolution of GCM simulation results [59, 60, 61, 62, 63]. Although these works are based on downscaled GCMs and simulation can be accurate for the expected or average rainfall distribution, they are far from perfect when it comes to extreme precipitation. First, no systematic evaluation has been

conducted to validate the accuracy of downscaled GCMs when used for extreme precipitation; therefore, it is not clear how reliable downscaled GCMs can be for extreme precipitation or what the applicability is in terms of the location. More importantly, there are some issues in the design of downscaled GCMs that affect the accuracy when used for extreme precipitation projection.

First, most works are based on repeated averaging, which significantly reduces the number of extreme events in the output. Such an effect has also been studied and verified by prior works [64, 65], which show that downscaling methods can significantly affect extreme precipitation analysis. In more detail, one popular method that is used by many works related to downscaling is called constructed analog (CA) [66, 67, 50, 51]. In this method, for each day and location, a set of historical days are selected that can represent different precipitation cases. A set of weights are also trained, which minimize the error between actual local precipitation and the weighted average of precipitation using this set of weights. CA methods assume that this set of weight values do not change from past to future; therefore, the same set can be used for future downscaling. More precisely, future downscaled precipitation is computed as the weighted average of a set of global precipitation values. This method, according to previous works, is able to provide high accuracy for non-extreme precipitation. However, when it comes to extreme precipitation, the accuracy is not as high. The biggest difference is that when applying the weighted average to computing the extreme precipitation, the distribution is reshaped by the average: the expectation is unchanged, but the variance is much lower. As a result, downscaled precipitation values are much less extreme

Furthermore, in many existing downscaling methods, the results of different days are computed independently, which reduces the dependency between different days for extreme precipitation. However, as demonstrated in Chapter 2, such day-to-day dependency in daily precipitation is important, especially when studying climate events that span a duration of time; for example, a number of continuous rainfall days. For the CA method and others, each day of downscaling is computed without considering day-to-day dependency. However, such dependency is important in many extreme events that involve multiple days of precipitation. Due to this, there is a significant gap between existing downscaling methods and the requirement from useful extreme precipitation applications

1.4.3 Gaps in Using Extreme Precipitation Projection in Practical Design

Applying extreme precipitation analysis and projection for engineering design is a complex task, involving both a practical need for simplicity as well as accuracy. Existing frameworks and methods for this topic requires highly complicated analysis. On the other hand, those that are used in practice tend to be oversimplified. For example, flooding is one major cause of damage by extreme precipitation [68, 69, 70, 71]. Currently, the best practice that applies extreme precipitation analysis and projection for drainage systems is based on the IDF chart [72, 73, 74]. Both the American Society of Civil Engineers (ASCE) 24 standard [75] and the Federal Highway Administration [76] discussed the basics of using the IDF chart for flood

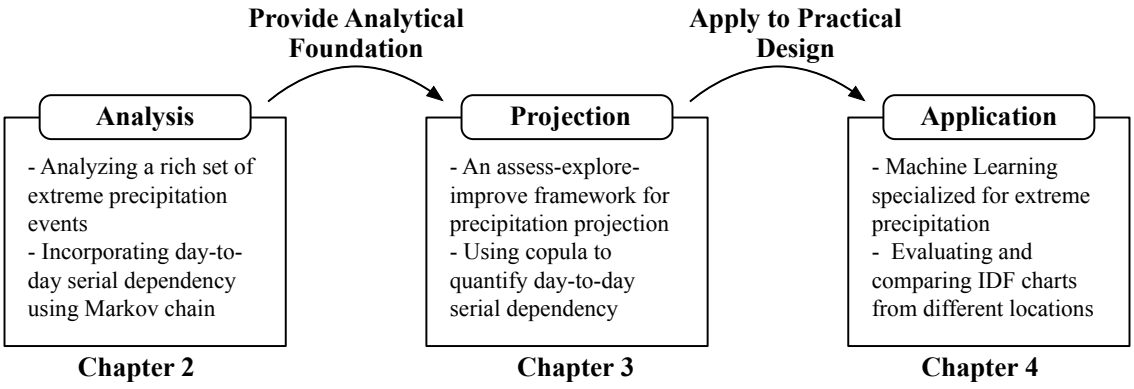

Figure 1.1: Outline of this dissertation.

events analysis. For each time period (for example, from 30 minutes to 6 hours), an IDF chart shows the maximum precipitation that can happen in this period. Various levels of confidence, i.e., different return periods, can be illustrated as different curves in the IDF chart.

Currently, one of the best practices is to use downscaled GCM simulations to compute IDF curves for future trends, but it also has some issues, as most existing GCM simulations provide rainfall data on a daily basis only. Almost all downscaling methods improve the resolution on the spatial aspect but not on the temporal aspect; therefore, it is difficult to use this method to obtain IDF curves on small hour-long or even sub-hour intervals, which is needed for many applications based on IDF for drainage design.

In summary, the root of the issue is that existing IDF projection methods are limited in capability because they cannot be used to project IDF relation for a short duration for all downscaling GCM simulations. It is a meaningful and important task to extend IDF curve projection methods to short durations using any downscaled GCM models desired.

1.5 Outline and Organization

The outline of this dissertation is summarized in Figure 1.1 and presented in three chapters. Some overview of each research outcome is introduce below, first. In Chapter 2, a mathematical model based on the Markov Chain is proposed to improve extreme precipitation analysis. It is observed that many existing analytical works assume that the precipitation for consecutive time periods are independently distributed, which may not be true for short duration. To incorporate serial dependency in the analytical model, a Markov Chain is used to model the precipitation in each day. Dynamic optimization is further used to find concrete analytical results of the model.

In Chapter 3, the above result is taken one step further to future projection. Although downscaling incorporates geographic details instability for future projections, some downscaling methods are not optimal for producing accurate extreme projections. To enhance existing downscaling GCM results for better extreme projection, this work initiated a systematic study on using downscaled GCM for future extreme precipitation. It is found that existing downscaled GCM results can produce erroneous extreme precipitation results, and the main reason is the lack of dependency incorporation. A method based on copula was further designed to integrate dependency back to the downscaled GCM results for better projection results.

In Chapter 4, the projection methods, integrated with machine-learning techniques, is applied for future IDF curve projection, particularly for short durations. It is observed that many downscaling-based IDF curve projection solutions do not

work well when the duration are shorter than six hours due to lack of data and invalidity of assumptions. Temporal downscaling is used based on machine-learning algorithms to produce accurate projections of IDF curves for short durations. Finally, in Chapter 5, the above efforts are summarized with a discussion on future directions.

1.6 Implications

It is urgent to update existing design standards to reflect a changing climate. When it comes to extreme precipitation, a few practical efforts have been done, partially due to the unsatisfactory performance of future extreme projection. For example, New York state is beginning to work on updating IDF incorporating the effect of climate change, while even more effort has been spent in Canada. The result of this dissertation can potentially improve existing projections of extreme precipitation, particularly for IDF curves. As a result, they can be incorporated in future design standards to accurately reflect climate change.

Chapter 2: Extreme Precipitation Analysis: Serial Dependency and Markov Chains

2.1 Overview

An accurate extreme precipitation projection can be built on deep understanding and modeling of extreme precipitation process only. This chapter introduces a fundamental framework for improved extreme precipitation analysis of an extensive number of extreme precipitation events. To improve the accuracy and applicability of extreme precipitation analysis, the new approach uses a model with non-stationarity and serial-dependency. From a high-level view, non-stationarity is incorporated into the analysis to reflect potential changes in the trend of extreme climate; serial dependency makes the model much more realistic. The proposed model is verified by two case studies on different areas and extreme precipitation events in the US. The content of this chapter is based on the materials from a paper published in the ASCE-ASME Journal of Risk and Uncertainty in Engineering Systems, Part A: Civil Engineering [77].

This study aims to provide enhanced models and analysis for extreme precipitation events with consideration of non-stationarity and serial dependency between

days. In detail, new methods are proposed to overcome the challenges discussed earlier and can be used to analyze and predict various extreme precipitation events with high accuracy. These new methods are based on characteristics of non-extreme precipitation, which have been well studied in the recent 20 years. This study also examines and incorporates serial dependency to further improve the accuracy. Finally, the effectiveness of the methods is verified using 10 decades of data in the Washington, DC metropolitan area. Predictions are also given for some selected years in the future till 2100.

Figure 2.1 shows the flowchart to analyze and predict extreme precipitation events in this chapter. There are three main approaches considered with different stationarity and dependency assumptions. The non-stationary model with serial dependency has the highest complexity but also highest accuracy, which is the main focus of this work. In the next section, more details of some background knowledge is introduced. Details of the proposed methods are provided after summarizing such related works, followed by two case studies to examine the accuracy of the proposed model.

2.2 Background and Literature Review

Extreme events are commonly characterized using generalized extreme value analysis (e.g., [78]). The goal of extreme value analysis is to find the distribution of the

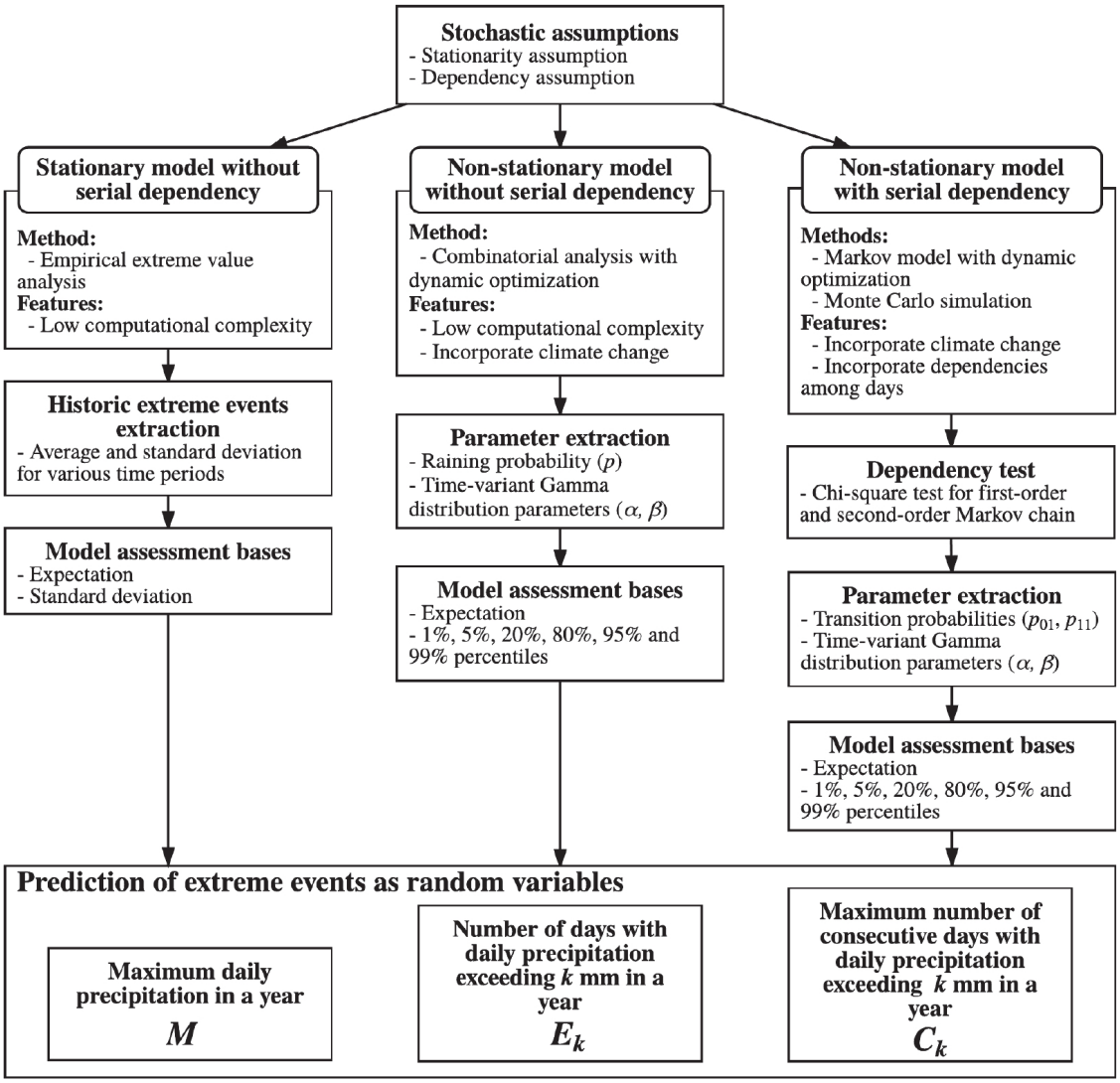

Figure 2.1: Flowchart of methods to analyze and predict extreme precipitation events.

maximum value of a set of random variables, namely

$$M_n = \max_{1 \le i \le n} \{X_i\}. \tag{2.1}$$

In particular, it considers n independent and identically distributed (IID) random variables that are all sampled from the same distribution with cumulative density function (CDF) as $F(\cdot)$. The CDF of M_n depends on the CDF of X_i according to

the following:

$$\begin{aligned} \Pr\left(M_n \leq x\right) &= \Pr\left(\max_{1\leq i\leq n}\{X_i\} \leq x\right) \\ &= \prod_{1\leq i\leq n} \Pr\left(X_i \leq x\right) = \left(F(x)\right)^n \end{aligned} \tag{2.2}$$

According to Fisher-Tippett-Gnedenko theorem [79], when n goes to infinity, the CDF of M_n always converge to the following form regardless of the CDF of X_i.

$$\begin{aligned} \lim_{n\to+\infty} \Pr\left(M_n \leq x\right) &= F(x;\mu,\sigma,\xi) \\ &= \exp\left\{-\left[1+\xi\left(\frac{x-\mu}{\sigma}\right)\right]^{-1/\xi}\right\} \end{aligned} \tag{2.3}$$

where μ is location parameter; σ is scale parameter; and ξ is shape parameter. GEV provides a general approach to find the asymptotical distribution of a set of *IID* random variables. There are three families of GEV distributions that are commonly used:

1. Gumbel distribution, where the CDF is

$$F(x) = \exp\left\{-e^{[-(x-\mu)/\sigma]}\right\} \tag{2.4}$$

2. Frechet distribution, where the CDF is

$$F(x) = \exp\left\{-(1+\xi(x-\mu)/\sigma)^{-1/\xi}\right\} \tag{2.5}$$

3. Reversed Weibull distribution, where the CDF is

$$F(x) = \exp\left\{-(-1-\xi(x-\mu)/\sigma)^{1/\xi}\right\} \tag{2.6}$$

The preceding GEV analysis can be improved to be more realistic by replacing GEV parameters with functions that vary according to time, namely μ, σ and ξ. Now the cumulative distribution function of GEV is also parameterized by time, shown as follows:

$$F(x;\mu(t),\sigma(t),\xi(t)) = \exp\left\{-\left[1+\xi(t)\left(\frac{x-\mu(t)}{\sigma(t)}\right)\right]^{-1/\xi(t)}\right\} \tag{2.7}$$

Previous works have explored this approach assuming $\mu(t), \sigma(t)$ as polynomials of t, and that $\xi(t)$ is a constant. Villafuerte and Matsumoto studied combining El Nino Southern Oscillation Index (ENSOI) with GEV parameters [80]. Some other related works used GEV with parameters changing linearly with time [81, 82, 35, 83]. Katz et al. instead used sinusoidal and log-sinusoidal functions for GEV parameters [84]. Panagoulia et al. used GEV parameters as third degree polynomials in mountainous area [85].

Feng et al. [40] used GEV models to study daily and weekly maximum precipitation from 1951 to 2000. Four different locations in China were studied. Koutsoyiannis [86] compared the effectiveness of different GEV models to analyze extreme precipitation in Europe and the United States. A comparison is also provided to discuss the accuracy of different fitting algorithms. Bertoldo et al. (2015) [34] studied

the difference when applying GEV to different geographic locations. In particular, mountains, hills, and flatlands area are studied. The study shows that all three parameters depend a lot on the type of geographic locations.

2.3 Methodology

This section discusses methods using the stationary model without serial dependency and newly proposed methods based on non-stationary models for the cases with or without serial dependency. These methods are able to analyze three extreme precipitation events in a period of n days. Extreme daily precipitation events in a year can be obtained by setting n as the number of days in a year, that is, 365 (or 366 for leap years). The analysis can also be used for other periods: if n were set as 30, the result would be extreme daily precipitation in a month; similarly for a season.

2.3.1 Extreme Precipitation Events

The main focus of this work is to analyze probabilistic behaviors of extreme daily precipitation for periods with different numbers of days. Many previous works only focused on analyzing maximum daily precipitation in a year. However, extreme precipitation is a complex stochastic process, which requires more than one statistic to summarize its impact. In this work, two additional extreme precipitation events that are of interest to engineers are also studied. They are summarized as follows:

1. Maximum daily precipitation in a year. It is denoted using the random variable

M. More generally, M_n is also used to represent maximum daily precipitation in a period of n days.

2. Number of days with daily precipitation exceeding k mm in a year. It is denoted using the random variable E_k. More generally, $E_{k,n}$ is used to represent number of days with daily precipitation exceeding k mm in a period of n days.

3. Maximum number of consecutive days with daily precipitation exceeding k mm in a year. It is denoted using random variable C_k. More generally, $C_{k,n}$ is used to represent maximum number of consecutive days with daily precipitation exceeding k mm in a period of n days.

2.3.2 Models for Daily Precipitation

Daily precipitation can be viewed as a sequence of random variables each representing the precipitation of one day, namely $X_1, ..., X_i, ..., X_n$. In order to analyze these random variables, various assumptions can be made to model the relationship among them. In general, the following two key assumptions determine the applicability and complexity of a model.

- **Stationarity assumption.** This assumption specifies whether the precipitation distributions in different years are the same or not. For example, if climate change is considered, a non-stationary assumption is justifiable to model the trending change of precipitation.

- **Independence assumption.** This assumption specifies whether daily pre-

cipitation random variables are independent of each other or not. For example, it is more likely to have rain after a rainy day than after a dry day, which means that the precipitation distribution of one day depends on the precipitation of the previous days. Such dependency between different days is referred to as serial dependency in the rest of the work.

In this work, three models with different combinations of assumptions are studied:

1. Stationary model without serial dependency. Daily precipitation distribution is assumed to be stationary between different years, and precipitation on different days is independent.

2. Non-stationary model without serial dependency. Daily precipitation distribution is assumed to be non-stationary between different years, and precipitation on different days is independent.

3. Non-stationary model with serial dependency. Daily precipitation distribution is assumed to be non-stationary between different years, and precipitation of different days can be dependent on each other.

This work focuses on non-stationary models with or without serial dependency. A stationary model without serial dependency is used as a baseline. The choice of an appropriate model is a tradeoff between complexity and accuracy, requiring a case-by-case discussion. A non-stationary model with serial dependency is able to capture the interdependency of daily precipitation of different days, but the underlying stochastic model is complex to analyze. Models that do not account for serial

dependency, on the other hand, are easier to analyze but the results may not be as accurate. In the case study, the accuracy of the two non-stationary models is compared and discussed.

2.3.3 Stationary Model without Serial Dependency

As mentioned earlier, GEV is a popular method used in a stationary model without serial dependency. However, as also pointed out by Katz [54] and Kharin et al. [87], GEV is an asymptotical analysis, and is only accurate when n approaches $+\infty$. Therefore, when used in extreme precipitation analysis, it is only applicable when computing the maximum of a long period. Further, GEV inherently works to find the distribution of maximum values, and can only analyze extreme precipitation events that are expressed as the maximum of a set of *IID* random variables. Due to the above limitation, empirical extreme analysis [42, 88, 89] is adopted in the stationary model, so that all three extreme precipitation random variables, i.e., M_n, $E_{k,n}$, and $C_{k,n}$ can be analyzed. When data from multiple stations are available, the empirical analysis of extreme precipitation events is accomplished in two steps:

1. Compute the extreme precipitation events for each station and each year.

2. Take the average over all stations for each year.

When empirical analysis is used as a baseline for future extreme precipitation events, a stationary assumption is required. Although simple, such an assumption hardly models the reality accurately, especially over a long period of time. The discrepancy between this assumption and reality becomes particularly significant given recent

trends with climate-change attribution. Further, directly analyzing historical data may not be possible if the extreme events to study are rare. For example, with a 20-year historic record, it may not be statistically significant to analyze an event with a return period of 50 years.

2.3.4 Non-stationary Model without Serial Dependency

In this section, a general method is discussed to compute various extreme precipitation events (M_n, $E_{k,n}$, and $C_{k,n}$) with climate change considered, assuming no serial dependency among days. The proposed method produces the distribution of extreme events, taking the distribution of the daily precipitation as input. The analysis is mainly based on combinatorial techniques and dynamic optimization [90]. One advantage of this method is that the derivation of the distribution of extreme events only depends on the CDF of non-extreme daily precipitation, which is generally available.

The analysis in this section can also be used in the inverse to compute design values of M_n, $E_{k,n}$, and $C_{k,n}$, with exceedance probabilities of 0.1, 0.02, 0.01, 0.002, 0.001, etc., which correspond to periods of 10, 50, 100, 500, and 1,000 years.

2.3.4.1 Probabilistic Distribution of Daily Precipitation

It is assumed that the precipitation distribution within each year does not change; therefore, $F(k)$ is used to denote the CDF of daily precipitation, that is, $F(k) = \Pr(X \leq k)$. Further, since no serial dependency is assumed, daily precipitation for each day can be viewed as independent. In this case, extreme precipitation analysis

is based on a list of *IID* random variables for daily precipitation. Existing probabilistic analysis is only applied on days with precipitation, ignoring days with no precipitation [91, 20]. However, the analysis here requires a CDF for daily precipitation, including days with rain and days without any rain. In order to achieve this, a transformation is performed. If the CDF of rainy days is denoted as $F^*()$, and assuming the probability that one day is rainy is p, then $F(k)$ can be calculated as

$$F(k) = p \times F^*(k) + (1 - p) \tag{2.8}$$

Assessment and prediction require obtaining the CDF for rainy days using, for example, gamma distribution, and the probability of having rain (See Appendix A for more details). The distribution of $F(k)$ can then be computed using Eq. 2.8.

2.3.4.2 Computation of Extreme Precipitation Events

Distribution of $\mathbf{M_n}$. The computation of M_n basically follows the definition. When the CDF is known, no asymptotical approximation is necessary, and the CDF of the maximum is:

$$\Pr(M_n \leq k) = (F(k))^n \tag{2.9}$$

Distribution of $\mathbf{E_{k,n}}$. The computation of $E_{k,n}$ is slightly more complicated. The n-day random process for daily precipitation can be viewed as a sequence of Bernoulli trials, where the i-th Bernoulli trial determines if the i-th days has precipitation

greater than k mm or not. Since all Bernoulli trials are identical, $I_{k,i}$ is introduced to indicate if the i-th day has precipitation greater than k mm. It can be observed that $\sum_{i=1}^{n} I_{k,i} \sim Bin(n, 1 - F(k))$, where $Bin()$ means binomial distribution. Then the following can be obtained:

$$\begin{aligned} \Pr\left(E_{k,n} \leq t\right) &= \Pr\left(\sum_{i=1}^{n} I_{k,i} \leq t\right) \\ &= \sum_{i=0}^{t} \binom{n}{i} (1 - F(k))^i (F(k))^{n-i} \end{aligned} \tag{2.10}$$

Distribution of $C_{k,n}$. While serial dependency is not considered, the previous calculation of M_n and $E_{k,n}$ are fairly straightforward. However, the analysis of $C_{k,n}$ in the following case is much more complex. Indeed, to obtain the exact distribution of $C_{k,n}$, recursive relationships with dynamic optimization is necessary as detailed later. Mathematically speaking,

$$C_{k,n} = \max\left\{t | \exists j, \text{ s.t. } 1 \leq j < n - t \text{ and } X_i \geq k \text{ for all } j < i \leq j + t\right\}. \tag{2.11}$$

In order to determine the distribution of consecutive extreme events, the law of total probability (see for example, [78]) is used to first divide the problem into small disjoint problems, namely "$C_{k,n} = t$ and $E_{k,n} = i$." Now each of the simpler

problems can be solved in turn. Mathematically speaking

$$\begin{aligned}
&\Pr\left(C_n^k = t\right) \\
&= \sum_{i=t}^{n} \Pr\left(C_{k,n} = t \text{ and } E_{k,n} = i\right) \\
&= \sum_{i=t}^{n} \#(C_{k,n} = t \text{ and } E_{k,n} = i)(F(k))^{n-i}(1 - F(k))^{i}
\end{aligned} \tag{2.12}$$

In the preceding equation, # represents "number of". Therefore, "$\#(C_{k,n} = t$ and $E_{k,n} = i)$" denotes number of all possible cases that satisfy "$C_{k,n} = t$ and $E_{k,n} = i$." The CDF of this event can then be computed in a straightforward manner.

Computing $\#(C_{k,n} = t$ and $E_{k,n} = i)$ directly is still complex. Therefore, it is further partitioned into smaller cases, depending on how many consecutive days from the last day that have precipitation of at least k mm. In more detail, $N[n, t, r, i]$ is used to denote the number of cases such that $C_{k,n} = t$ and $E_{k,n} = i$, and that from the last day, there are consecutive r days, each with precipitation of at least k mm. These statements lead to the following:

$$\#(C_{k,n} = t \text{ and } E_{k,n} = i) = \sum_{j=0}^{i} N[n, t, j, i] \tag{2.13}$$

Now, $N[n, t, r, i]$ can be computed recursively using dynamic optimization with the

following recursive relationship

$$N[n,t,r,i] = \begin{cases} 0 & \text{if } t > i \text{ or } r > t \\ \sum_{j=0}^{t} N[n-1,t,j,i] & \text{if } r = 0 \\ N[n-1,t,r-1,i-1] & \text{if } t > r > 0 \\ N[n-1,t,r-1,i-1] + N[n-1,t-1,r-1,i-1] & \text{if } t = r > 0 \end{cases} \tag{2.14}$$

with the basic cases as follows:

$$N[1,t,r,i] = \begin{cases} 1 & \text{if } t = 1, r = 1, i = 1 \\ 1 & \text{if } t = 0, r = 0, i = 0 \\ 0 & \text{otherwise} \end{cases} \tag{2.15}$$

2.3.5 Non-stationary Model with Serial Dependency

The method introduced earlier assumes that there is no serial dependency; however, as shown in the case study, there is strong evidence that serial dependency exists commonly for precipitation. The method introduced herein is able to incorporate serial dependency into the analysis.

The main idea is based on a hybrid methodology in which random variables for daily precipitation are decomposed into two separate events and later combined. The dependency between different days is limited in some specific manner to be introduced in a subsequent section. As a result, the analysis is not overly complex but yields more accurate outcomes compared to ones introduced in the previous

sections. Similar to the previous section, the analysis in this section can also be used to compute the value of M_n, $E_{k,n}$, and $C_{k,n}$ for return periods of 10, 50, 100, 500, and 1,000 years.

2.3.5.1 Hybrid Model Based on Markov Chain

Because there is a serial dependency, each day can follow a different precipitation distribution. Therefore, all days are numbered starting from 1 and X_i is used to denote the amount of precipitation on the i-th day. X_i is a hybrid random variable, which consists of two components, namely J_i and Y_i: J_i is a random variable indicator that indicates if the i-th day is a wet day (with precipitation) or dry day (no precipitation). Mathematically speaking,

$$J_i = \begin{cases} 1 & \text{if } X_i > 0 \\ 0 & \text{if } X_i = 0 \end{cases} \tag{2.16}$$

Y_i represents the amount of precipitation on the i-th day conditioning on the fact that the i-th day is rainy, that is

$$\Pr\left(Y_i = k\right) = \Pr\left(X_i = k | J_i = 1\right) \tag{2.17}$$

The distribution of the precipitation on the i-th day, namely X_i, can then be computed easily with two cases according to the definition of conditional probabilities

as follows:

$$\Pr(X_i = k) = \begin{cases} \Pr(Y_i = k)\Pr(J_i = 1) & \text{if } k > 0 \\ \Pr(J_i = 0) & \text{if } k = 0 \end{cases} \tag{2.18}$$

Because Y_i and J_i fully describe the daily precipitation, they can be used to calculate the extreme behavior of daily precipitation. Further, both random variables are simpler than X_i. Nevertheless, there are still additional challenges in evaluating the hybrid model for extreme events, which is the focus of the subsequent subsections.

The decomposition discussed earlier does not introduce serial dependency into the model. In order to capture the serial dependency, a Markovian assumption is added (See Appendix B). Further, instead of directly assuming that X_i's are dependent on each other, it is assumed that there are serial dependencies for Y_i's and J_i's, respectively.

As mentioned previously, J_i is not independent over different days: raining after a wet day is more likely to happen than raining after a dry day. One common way to model such dependency is to use a Markov chain. In general, the probability that a particular day is a rainy day can be modeled as a function of all previous days, that is, $\Pr(J_i|J_{i-1}, ..., J_1, J_0)$, where J_0 is the initial state. A m-order Markov chain assumes that such dependency stops after backtracking m days, that is

$$\Pr(J_i|J_{i-1}, ..., J_1, J_0) = \Pr(J_i|J_{i-1}, ..., J_{i-m}) \tag{2.19}$$

A reasonable assumption for precipitation modeling is to use J_i as a first order

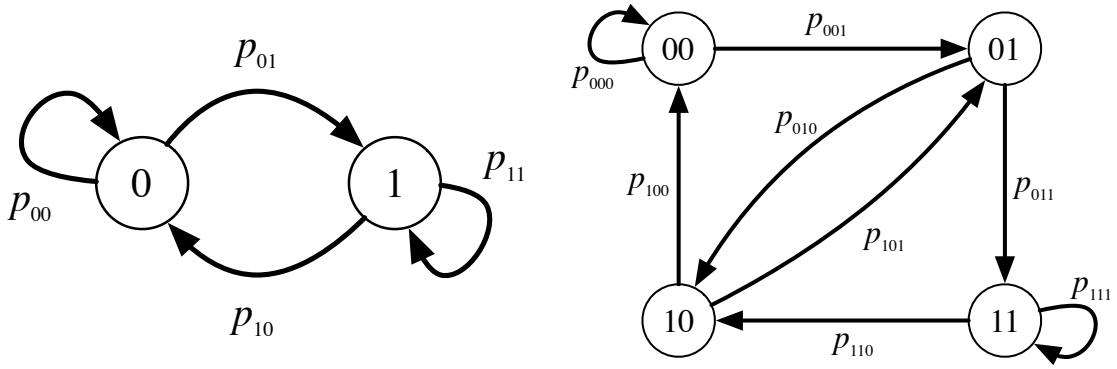

(a) First order Markov model for J_i.

(b) Second order Markov model for J_i.

Figure 2.2: Markov models for J_i.

Markov chain ($m = 1$) for daily precipitation.

Graphic depictions of the first and second Markov chains for J_i are included in Figure 2.2. To simplify the notation, p_{10} is used to denote the transition probability $\Pr(J_i = 0|J_{i-1} = 1)$, and similarly for all other transition probabilities. Similar notations are also used to denote second order transition probabilities: Using p_{100} to denote the probability $\Pr(J_i = 0|J_{i-1} = 0, J_{i-2} = 1)$. Note that not all transition probabilities are dependent. In particular, the first order Markov chain in Figure 2.2a can be described using only p_{01} and p_{11}, since $p_{00} = 1 - p_{01}$ and that $p_{10} = 1 - p_{11}$. The second order Markov chain in Figure 2.2b can be described fully using only p_{110}, p_{100}, p_{010}, and p_{000}, since, for example, $p_{110} = 1 - p_{111}$.

Some Markovian behavior can also be observed from Y_i. For example, it is more likely to have heavier precipitation if the previous day has a lot of precipitation. However, since the value of Y_i is not binary, such dependency can be complex. In this work, a restrictive assumption is made: the conditional precipitation of the i-th day depends on $J_{i-1}, ..., J_0$. This means the amount of precipitation only depends on if previous days are wet of dry.

In detail, the conditional probability of interests is $\Pr(Y_i|J_{i-1}, ..., J_0)$. Applying the similar idea from J_i to here, the assumption can be expressed as: Y_i only depends on previous m days, i.e.

$$\Pr(Y_i|J_{i-1}, ..., J_0) = \Pr(Y_i|J_{i-1}, ..., J_{i-m}) \tag{2.20}$$

Note that Y_i does not exactly corresponds to a Markov chain because the event to study is Y_i while it is conditioned on J_i, which is not of the same type. Following notations are introduced for simplification:

$$F_0(k) = \Pr(Y_i \leq k|J_{i-1} = 0) \tag{2.21}$$

and

$$F_1(k) = \Pr(Y_i \leq k|J_{i-1} = 1) \tag{2.22}$$

for first order relations.

Note that Katz [54] also modeled daily precipitation as a Markov chain. However, it was only used to obtain the asymptotical behavior of maximum precipitation. In this work, an enhanced distribution is computed using dynamic optimization without asymptotical approximation. Further, distributions of three different extreme precipitation events are studied.

2.3.5.2 Computation of Extreme Precipitation Events

In the following paragraphs, three extreme precipitation events are analyzed based on the model introduced previously. Since there is a serial dependency, simple combinatorial methods do not work anymore, because the analysis needs to incorporate the precipitation in previous days.

Distribution of $\mathbf{M_n}$. Since Markov process relies on the status of the initial state, the original problem $\Pr(M_n \leq k)$ can be decomposed into two sub-problems $\Pr(M_n \leq k|J_0 = 0)$ and $\Pr(M_n \leq k|J_0 = 1)$. Assuming that the initial state has probability of p to be a dry day, the final result can be computed using the law of total probability as follows:

$$\Pr(M_n \leq k) = (1-p) \times \Pr(M_n \leq k|J_0 = 0) + p \times \Pr(M_n \leq k|J_0 = 1) \quad (2.23)$$

Because the computations of the two terms are similar, the focus herein is on computing $\Pr(M_n \leq k|J_0 = 0)$, without loss of generality. To facilitate the computation, some new random variables are introduced: W_n and D_n, which indicate number of wet-wet days (i.e., a wet day followed by another wet day) and number of dry-wet days (i.e., a dry day followed by a wet day) across the period to study (n days).

According to law of total probability, it can be obtained that

$$\begin{aligned}
&\Pr\left(M_n \leq k | J_0 = 0\right) \\
&= \sum_{i=0}^{n} \sum_{j=0}^{n} \Pr\left(W_n = i \text{ and } D_n = j | J_0 = 0\right) \times \Pr\left(M_n \leq k | W_n = i, D_n = j, J_0 = 0\right)
\end{aligned} \tag{2.24}$$

Note that the distribution of daily precipitation does not depend on the order of the days. It only depends on if the previous days are rainy days or dry days. For any different day i and day j, with precipitation k_i and k_j, it is true that

$$\begin{aligned}
&\Pr\left(Y_i = k_i | J_{i-1}\right) \Pr\left(Y_j = k_j | J_{j-1}\right) \\
&= \Pr\left(Y_i = k_i | J_{i-1} \text{ and } Y_j = k_j | J_{j-1}\right)
\end{aligned} \tag{2.25}$$

Therefore, the second term can be computed as follows:

$$\begin{aligned}
&\Pr\left(M_n \leq k | W_n = i, D_n = j, J_0 = b\right) \\
&= \Pr\left(X_1 \leq k, ..., X_n \leq k | W_n = i, D_n = j, J_0 = b\right) \\
&= \Pr\left(Y_l \leq k | J_{l-1} = 1\right)^i \Pr\left(Y_l \leq k | J_{l-1} = 0\right)^j \\
&= F_1(k)^i F_0(k)^j
\end{aligned} \tag{2.26}$$

The focus now is to compute $\Pr\left(W_n = i \text{ and } D_n = j | J_0 = b\right)$. To simplify the notation, $P[i, j, b, n]$ is used to denote the probability that across n days, there are i number of wet-wet days and j number of dry-wet days conditioning on that the

initial state is b, or mathematically

$$P[i, j, b, n] = \Pr\left(W_n = i \text{ and } D_n = j | J_0 = b\right) \tag{2.27}$$

Because of the memoryless property of Markov chain, *shifting* the initial state does not change the probability. Inspired by this observation, this probability can be computed recursively using dynamic optimization. Depending on the initial state, the following two equations can be used

$$P[i, j, b, n] = \begin{cases} P[i, j, 0, n-1]p_{00} + P[i, j-1, 1, n-1]p_{01} & \text{if } b = 0 \\ P[i, j, 0, n-1]p_{10} + P[i-1, j, 1, n-1]p_{11} & \text{if } b = 1 \end{cases} \tag{2.28}$$

The base cases are

$$P[i, j, b, 1] = \begin{cases} p_{11} & \text{if } b = 1, i = 1, j = 0 \\ p_{01} & \text{if } b = 0, i = 0, j = 1 \\ p_{10} & \text{if } b = 1, i = 0, j = 0 \\ p_{00} & \text{if } b = 0, i = 0, j = 0 \\ 0 & \text{otherwise} \end{cases} \tag{2.29}$$

The intuition of this recursion is to consider different cases according to the precipitation on the first day. Without loss of generality, let's focus on $P[i, j, 0, 1]$. Recall that $P[i, j, 0, 1]$ represents the probability that there are i wet-wet days and j dry-wet days in a n-day period with $J_0 = 0$ as the initial state. There are two subcases to consider: (1) the 1st day is a dry day and (2) the 1st day is a wet day. Later they

are combined together using the law of total probability, as shown in the following equations and Figure 2.3.

$$\begin{aligned}
&\Pr\left(W_n = i, D_n = j | J_0 = 0\right) \\
&= \Pr\left(W_n = i, D_n = j | J_1 = 0, J_0 = 0\right) \Pr\left(J_1 = 0 | J_0 = 0\right) \\
&\quad + \Pr\left(W_n = i, D_n = j | J_1 = 1, J_0 = 0\right) \Pr\left(J_1 = 1 | J_0 = 0\right) \\
&= \Pr\left(W_n = i, D_n = j | J_1 = 0, J_0 = 0\right) p_{00} + \Pr\left(W_n = i, D_n = j | J_1 = 1, J_0 = 0\right) p_{01}
\end{aligned} \tag{2.30}$$

If the first day is a dry day, then in the next $n-1$ days, there needs to be i wet-wet days and j dry-wet days. This essentially means that

$$\Pr\left(W_n = i, D_n = j | J_1 = 0, J_0 = 0\right) = \Pr\left(W_{n-1} = i, D_{n-1} = j | J_0 = 0\right) \tag{2.31}$$

If the first day is a wet day, then in the next $n-1$ days, there needs to be i wet-wet days and $j-1$ dry-wet days. That is

$$\Pr\left(W_n = i, D_n = j | J_1 = 1, J_0 = 0\right) = \Pr\left(W_{n-1} = i, D_{n-1} = j-1 | J_0 = 1\right) \tag{2.32}$$

Using this recursive relationship, the exact value of $P[i, j, b, n]$ can be computed. The maximum precipitation can then be computed accurately for this scenario.

Distribution of $\mathbf{E_{k,n}}$. It is also possible to obtain the exact distribution for the random variable $E_{k,n}$. By using the law of total probability, the original probability

is partitioned into smaller ones:

$$\Pr\left(E_{k,n}=t|J_0\right)=\sum_{i,j}\Pr\left(W_n=i,D_n=j|J_0\right)\Pr\left(E_{k,n}=t|W_n=i,D_n=j\right) \quad (2.33)$$

Since $\Pr\left(W_n=i,D_n=j|J_0=b\right)=P[i,j,b,n]$ is already computed in the previous discussion, the focus herein is how to compute the second term. To compute the second term, it is further divided into cases, depending on how many extreme days happen in wet-wet cases and how many extreme days happen in dry-wet days. The detail is shown in the following equation:

$$\Pr\left(E_{k,n}=t|W_n=i,D_n=j\right)= \quad (2.34)$$
$$\begin{cases} 0 & \text{if } i+j<t \\ \sum_s \binom{i}{s}\binom{j}{t-s}F_1(k)^{i-s}(1-F_1(k))^s F_0(k)^{j-t+s}(1-F_0(k))^{t-s} & \text{otherwise} \end{cases}$$

Distribution of $\mathbf{C_{k,n}}$. The analysis for consecutive extreme events becomes even more complex. To simplify the computation while still obtaining accurate results, Monte Carlo simulation is used to find the results. In detail, in each run of simulation, one year of precipitation is generated according to the non-stationary model with serial dependency, as mentioned in previous sections. The final distribution can be obtained by running the simulation for a large enough number of times. Note that the Markov chain has a small number of states; therefore, the effect of local-trap is not significant.

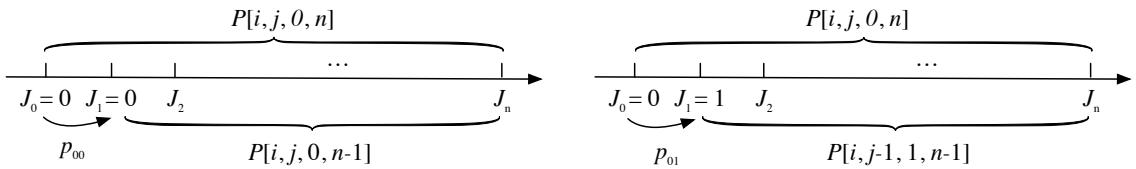

Figure 2.3: Reducing $P[i, j, 0, n]$ into two sub problems.

2.4 Case Study: Extreme Precipitation Events Prediction in Washington D.C. Area

In this section, a case study is conducted using ten decades of data from the Washington metropolitan area, centered on Washington, D.C., the capital of the United States. Both of the proposed methods are applied and compared with stationary empirical analysis based on the annual extreme daily precipitation events, including M, E_{15}, E_{30}, and C_{10}. The probability distributions of ratios among selected cases are also computed showing that serial dependency is able to further improve the accuracy of analysis, avoiding underestimation in many cases.

2.4.1 Data Selection

Data are obtained from National Oceanic and Atmospheric Administration (NOAA) [1]. More description can be found in Appendix E. Ten decades of data are collected consisting of more than 350 stations, which includes rainfall and melted snow. Due to historical reasons, some stations contain more years of data than other stations and many stations are relatively recent (with less than 20 years of data). In Figure 2.4, the spatial and temporal distributions of the stations are shown. Figure 2.4a shows

the locations of all stations studied. NOAA associates this set of stations to this area according to the U.S. Climatological Division [92]. These stations are all located in the climate division MD-3, MD-4, MD-6, VA-4 and the District of Columbia. In Figure 2.4b, each horizontal bar represents the time duration of one station. For example, a bar from 1960 to 2000 means that data is available in this station from the year 1960 to the year 2000. It can be observed that many stations are set up after the year 2000.

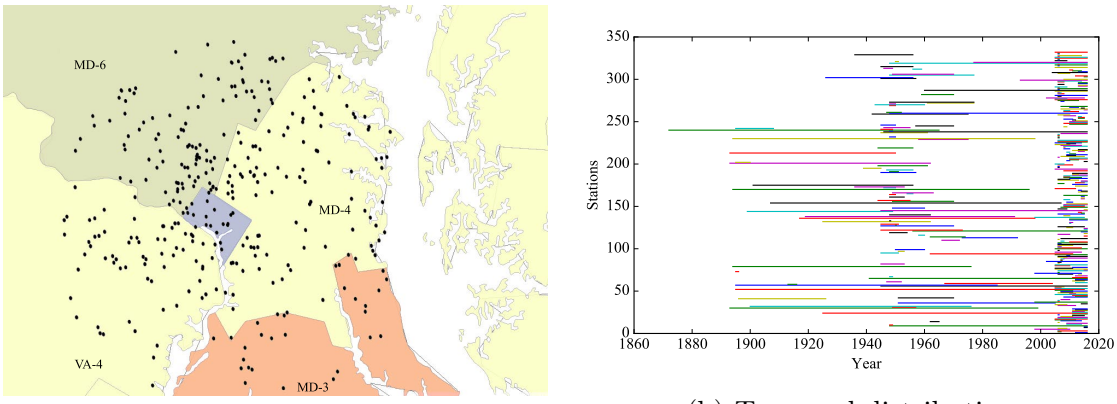

(a) Spatial distribution

(b) Temporal distribution

Figure 2.4: Spatial and temporal distributions of stations in the Washington metropolitan area.

	M (mm)		E_{15} (day)		E_{30} (day)		C_{10} (day)	
Time period	Mean	SD	Mean	SD	Mean	SD	Mean	SD
2006-2015	73.74	30.60	25.10	5.99	8.00	2.28	3.00	1.55
1991-2015	68.02	24.46	26.56	5.49	8.56	3.23	2.68	1.09
1960-2015	66.30	22.10	22.35	5.46	7.13	2.81	2.35	0.93

Table 2.1: Stationary analysis: extreme precipitation events based on data from selected time periods. (SD stands for standard derivation.)

2.4.2 Analysis under Stationary Model without Serial Dependency

As mentioned in previous sections, statistics from empirical data can be used to make estimations for the future under the stationary assumption. The results of the stationary empirical analysis are shown in Table 2.1. Three historical time periods are selected. For each time period, average values of M, E_k, and C_k are presented. One can observe from the table that, for example, the average value of M is higher if the averages are taken over a shorter period. This is because the overall trending of M is increasing in the past 50 years. When comparing with non-stationary analysis in the following discussion, values based on the period 1960 - 2015 are used as a baseline. It can be seen that the number of stations (sample size) is different from different years. In order to eliminate the effect of time-varying sample size, the results in Table 2.1 are obtained in two steps. First, the averages of extreme precipitation events are computed across different stations for each year. Then for different time periods, the averages of different years are computed. This is an unbiased estimator for the extreme precipitation events considered in this work.

2.4.3 Analysis and Prediction under Non-stationary Model without Serial Dependency

2.4.3.1 Parameter Extraction

The first step in the proposed analysis is to obtain $F(k)$, that is, the CDF of daily precipitation for each year. This is obtained by aggregating all data from all stations

according to year. The probability of raining (p) and gamma distribution parameters (α, β) can then be obtained. CDF can be computed using Eq. 2.8. In Figure 2.5, the trends of shape (α) and scale (β) parameters from the year 1900 are shown. The decrease of shape and increase of scale indicates a trend toward more extreme precipitation.

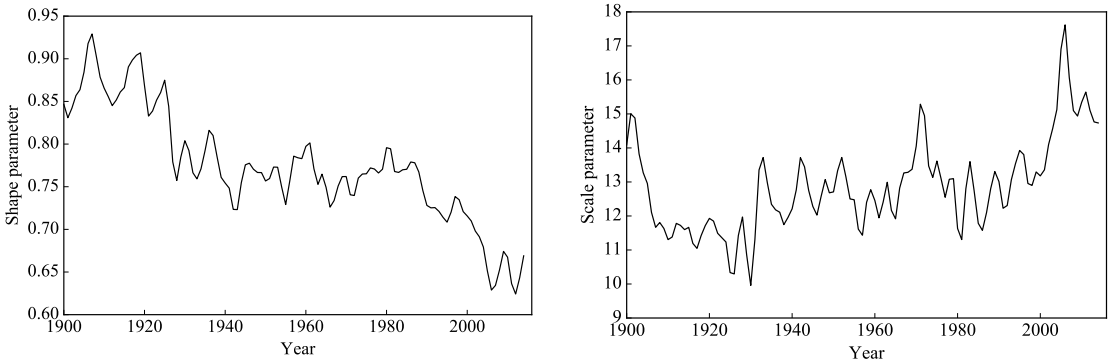

(a) decreasing trend of shape parameter

(b) increasing trend of scale parameter

Figure 2.5: Trend of gamma distribution parameters from 1900 to 2015.

2.4.3.2 Analysis Assessment

To assess the accuracy of the analysis, a comparison is conducted between the observed extreme precipitation and the distribution computed from the analysis. In detail, all data but those from station USC00185111 are aggregated and used to compute $F(k)$, which is further used to compute extreme precipitation distributions. Figures 2.6a, 2.6c, and 2.6e show the results for different events. It can be observed that the extreme precipitation events from station USC00185111 are close to the expectation computed from the analysis. This indicates that the model is of high accuracy.

Figure 2.6a shows the analysis results for distribution of annual maximum

daily precipitation (M). Light area represents the range with probability 5% - 95%; Dark area represents the range with probability 20% - 80%. The expectation from the analysis is shown as the solid line, whereas the dotted line shows the observed annual maximum daily precipitation observed from station USC00185111. This station is chosen for validation because the data is available for a long time from 1900 to 2015. As shown in the figure, the solid line and dotted line are close to each other for most of the years, and it falls into the 20 - 80% range for almost all years. Therefore, the result under the non-stationary model without serial dependency is accurate for computing extreme event M.

Figure 2.6c shows the analysis result for extreme events E_{15} and E_{30}. Similar to the previous figure, the expectation and the actual results are also shown as solid lines and dotted lines, which indicate that the accuracy of the model is high in the last decades.

Similar analysis is also conducted for extreme event C_{10}, as shown in Figure 2.6e. The expected value alters between 2 and 3 days during the past decades. There is no obvious increasing or decreasing trend according to the distribution. It can also be observed that there is an underestimation: the observed results from the selected station go beyond 1 - 99% for many years. The main reason is that in the analysis of continuous extreme events, the dependency between different days plays an important role. In this model, such dependency is ignored, leading to an underestimation in the analysis. In the next section, it is shown that non-stationary model with serial dependency is able to provide better analysis.

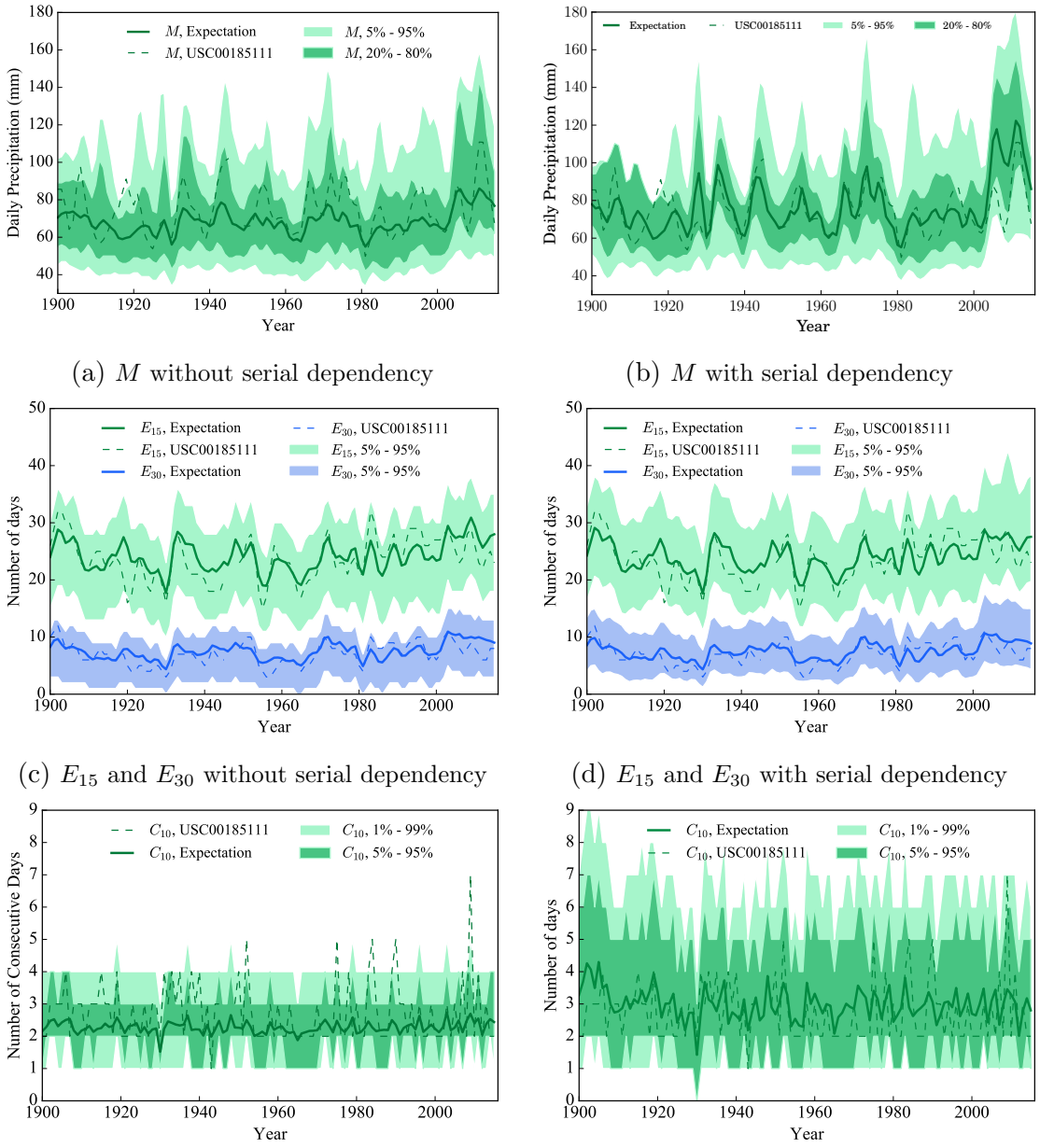

(a) M without serial dependency

(b) M with serial dependency

(c) E_{15} and E_{30} without serial dependency

(d) E_{15} and E_{30} with serial dependency

(e) C_{10} without serial dependency

(f) C_{10} with serial dependency

Figure 2.6: Analytical distribution of different events under non-stationary models vs. observation from the selected station.

2.4.3.3 Prediction of Extreme Events

The preceding validation means that if $F(k)$ for each year is predicted accurately, then the result from the proposed non-stationary model without serial dependency

Year	Shape (α)	Scale (β)	Raining Prob. (p)
Baseline	-	-	-
2020	0.65	14.97	0.369
2050	0.58	16.32	0.419
2080	0.51	17.67	0.468
2100	0.46	18.56	0.502

Table 2.2: Prediction of parameters (α, β, p) linearly in future years based on non-stationary model without serial dependency. (SD stands for standard derivation.)

	M (mm)		E_{15} (day)		E_{30} (day)		C_{10} (day)	
Year	Mean	SD	Mean	SD	Mean	SD	Mean	SD
Baseline	66.30	22.10	22.35	5.46	7.13	2.81	2.35	0.93
2020	68.25	18.34	29.23	5.16	9.08	2.93	4.08	1.17
2050	72.83	19.15	32.03	5.36	10.52	3.18	4.02	1.12
2080	77.68	21.29	33.75	5.49	11.54	3.30	3.89	1.07
2100	78.93	21.54	33.82	5.56	11.76	3.39	3.73	1.02

Table 2.3: Prediction of extreme events $(M, E_{15}, E_{30}, C_{10})$ in future years based on non-stationary model without serial dependency. (SD stands for standard derivation.)

is close to the observed value. Therefore, in order to obtain accurate results, one needs to obtain the prediction of $F(k)$. For each year, related parameters (p, α, β) are obtained from the precipitation in that year. As an initial approximation, a linear trend is used for future prediction of parameters, based on data since 1960. These parameters, in turn, determine the future precipitation distribution.

In Table 2.2 Table 2.3 and , the result of the prediction along with the baseline from Table 2.1 is shown. The baseline in Table 2.2 is based on Table 2.1. Compared with stationary analysis, predictions under the non-stationary model are higher. For example, the M value for the year 2050 is about 9% higher compared with the stationary baseline and the value for the year 2100 is about 18% higher.

2.4.4 Analysis and Prediction under Non-stationary Model with Serial Dependency

2.4.4.1 Chi-square Test for Serial Dependency

Statistical hypothesis testing is firstly performed to assess the accuracy of modeling J_i as a first order Markov chain. The first step is to check if J_i and J_{i-1} are independent or not. In particular, the chi-square test is used, which is a popular statistical hypothesis test for dependency of two random variables. For each year, the occurrence of precipitation for all consecutive two days are collected and counted. Chi-square tables are constructed and the values are computed out of the tables using standard method. The 2×2 contingency table for the year 2000 is shown in Table 2.4.

	$J_i = 0$	$J_i = 1$	Total
$J_{i-1} = 0$	184	59	243
$J_{i-1} = 1$	59	64	123
Total	243	123	366

Table 2.4: The 2x2 contingency table for year 2000.

The chi-square value can be calculated as follows. Here, $O_{i,j}$ are observed values; $E_{i,j}$ are expected values. More details about chi-square test can be found in

(see, for example, [93]).

$$\begin{aligned}\chi^2 &= \sum_{i=1}^{2}\sum_{j=1}^{2}\frac{(O_{i,j}-E_{i,j})^2}{E_{i,j}} \\ &= \frac{(184-161.3)^2}{161.3}+\frac{(59-81.7)^2}{81.7}+\frac{(59-81.7)^2}{81.7}+\frac{(64-41.3)^2}{41.3} \\ &= 28.3\end{aligned} \tag{2.35}$$

Figure 2.7a shows chi-square values of each year calculated from station USC00185111. The same test is also applied to other stations, where the results are similar. Three thresholds are also shown for comparison. For example, if the chi-square value is greater than the threshold for 99%, then with at least 99% confidence, J_i and J_{i-1} are not independent. The figure shows that for almost all years, confidences of 99% are obtained and that for more than half of all years, such confidence is as high as 99.9%. These are strong evidence that serial dependency exists between J_i and J_{i-1}.

The next step is to check if a first order Markov chain is sufficient, that is if a second Markov chain is needed. In detail, the goal is to compute the dependency between J_i and J_{i-2}, with J_{i-1} fixed. In Figure 2.7b, results for this chi-square test are shown when J_{i-1} is fixed as 0 and 1, respectively. The results indicate that there is no strong evidence to conclude that J_i and J_{i-2} have dependency even only for 90% confidence. When comparing with the values in Figure 2.7a, the values in Figure 2.7b are also much smaller. This means that the dependency between J_i and J_{i-2}, if exists, is much less than the dependency between J_i and J_{i-1}.

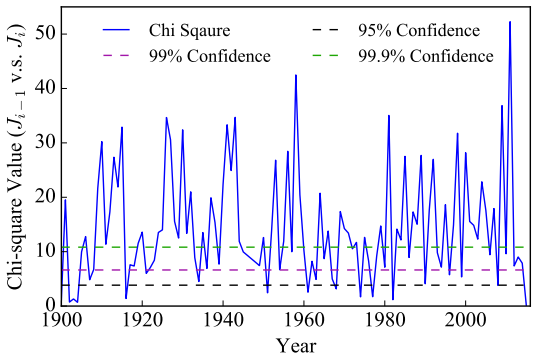

(a) Chi-square values between J_i and J_{i-1} for station USC00185111

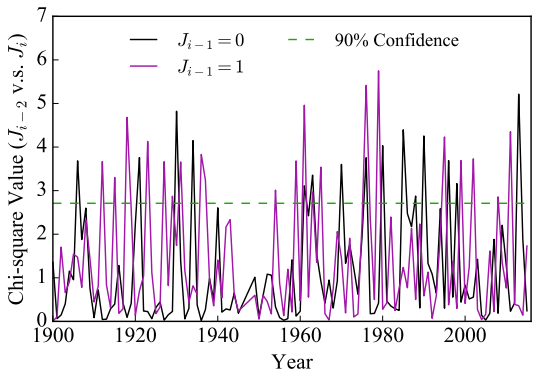

(b) Chi-square values between J_i and J_{i-2} for station USC00185111

Figure 2.7: Chi-square tests.

2.4.4.2 Parameter Extraction

Gamma distribution parameters and Markov transition probabilities (p_{11}, p_{01}) are needed for each year in the non-stationary model with serial dependency. In Figure 2.8, the observed values of p_{01} and p_{11} are shown, aggregated from all stations for each year. According to the figure, there is a significant difference between the chances of rain after a rainy day compared to one after a dry day. This again shows that the precipitation of one day depends on whether the previous day is rainy or not. It can also be observed that there is an increasing trend for the probability of rain.

2.4.4.3 Analysis Assessment

In Figure 2.6b, Figure 2.6d, and Figure 2.6f, results are shown in a similar manner to verify the accuracy of non-stationary model with serial dependency. It can be seen that the computed distribution matches the real results closely. Further, by

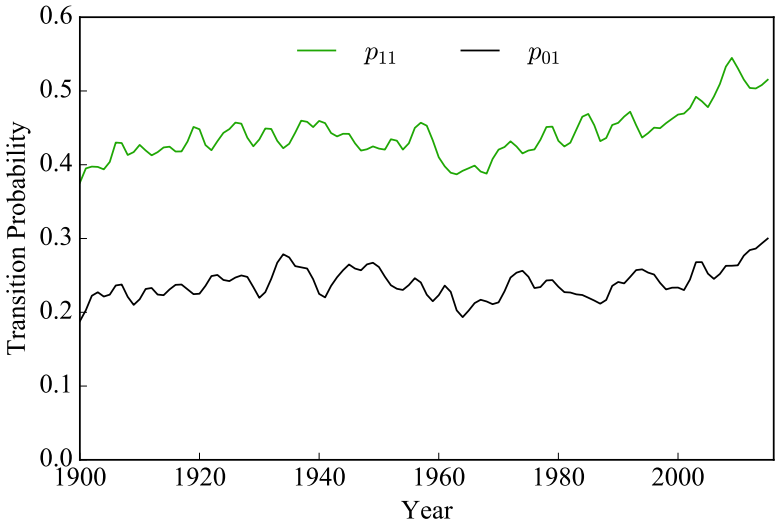

Figure 2.8: Trend of transition probabilities (p_{01}, p_{11}) from 1900 to 2015.

comparing with the results from non-stationary analysis without serial dependency, the new results match real extreme precipitation better. In particular, expectations for M and C_{10} are significantly better. The expected values for E_{15} and E_{30} are at the same level compared to the results from the non-stationary model without serial dependency. However, there is an observable difference in terms of the range for 5 - 95%.

The main reason why this model has higher accuracy stems from its ability to incorporate dependency. Such dependency causes more extreme precipitation, which is not captured in the non-stationary model without serial dependency.

2.4.4.4 Prediction of Extreme Events

Table 2.5 shows the prediction under the non-stationary model with serial dependency. As expected, the predicted values are slightly higher than the ones under the non-stationary model without serial dependency. When compared with the baseline,

a higher increase is also found. For example, the M value for the year 2100 is about 21% higher than the stationary baseline.

	M (mm)		E_{15} (day)		E_{30} (day)		C_{10} (day)	
Year	Mean	SD	Mean	SD	Mean	SD	Mean	SD
Baseline	66.30	22.10	22.35	5.46	7.13	2.81	2.35	0.93
2020	68.31	18.33	29.40	5.43	9.13	2.98	4.09	1.17
2050	73.11	19.18	32.75	5.69	10.77	3.26	4.04	1.13
2080	78.50	21.27	35.39	5.95	12.08	3.48	3.92	1.07
2100	80.00	21.61	36.26	6.07	12.62	3.58	3.78	1.02

Table 2.5: Prediction of extreme events ($M, E_{15}, E_{30}, C_{10}$) in future years based on non-stationary model with serial dependency. (SD stands for standard derivation.)

2.4.5 Contribution of Serial Dependency in Non-stationary Models

To explore the contribution of serial dependency to the analysis, distributions of ratios between extreme precipitation events with serial dependency and ones without serial dependency are computed. In general, it is difficult to compute the exact ratio distribution; therefore, Monte Carlo simulation is used to obtain an approximation. In detail, the analysis is first performed without considering serial dependency, and for the second time considering serial dependency using the proposed method. From the analysis results, a ratio on the contribution of serial dependency can be computed. The ratio distribution for M, E_{15} and C_{10} are shown in Figure 2.9. For M and C_{10}, when considering serial dependency, the resulted distribution is about 16% and 7% more extreme than the distribution computed without serial dependency respectively. Histograms summarizing all ratios from previous years are also provided. The ratio of E_{15} fluctuates around 1, meaning that serial dependency does

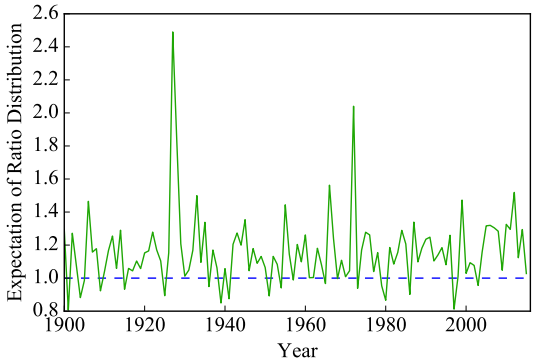

(a) Expected ratio distribution for M

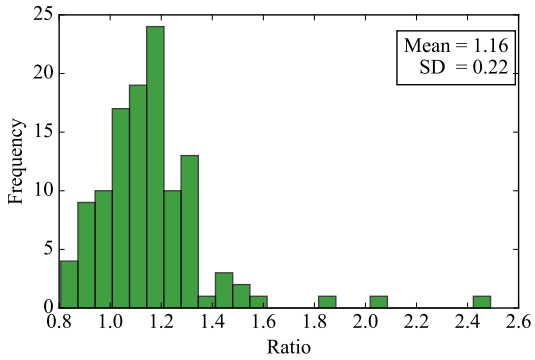

(b) Histogram of expected ratio for M

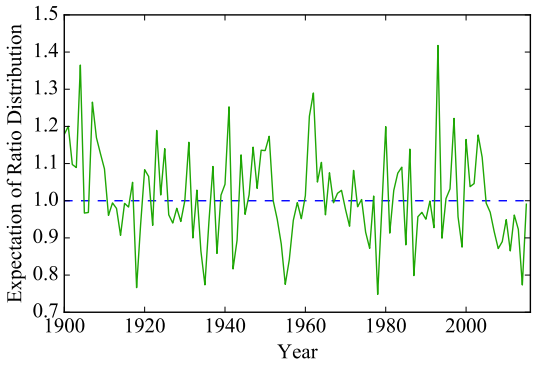

(c) Expected ratio distribution for E_{15}

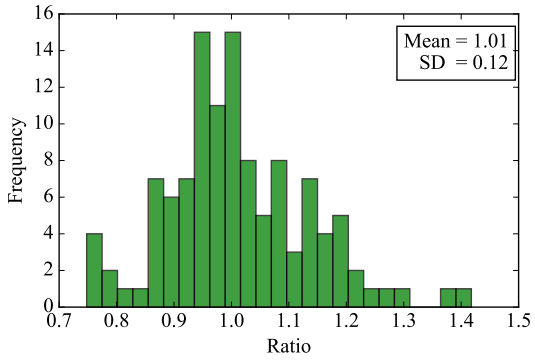

(d) Histogram of expected ratio for E_{15}

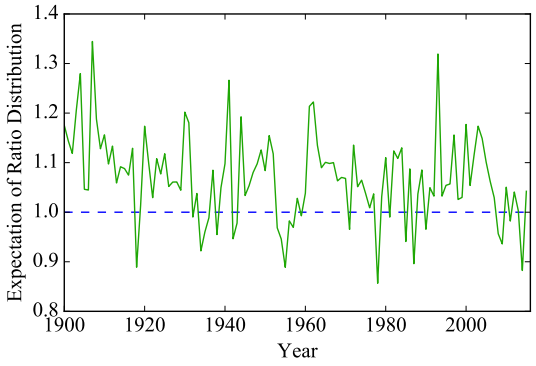

(e) Expected ratio distribution for C_{10}

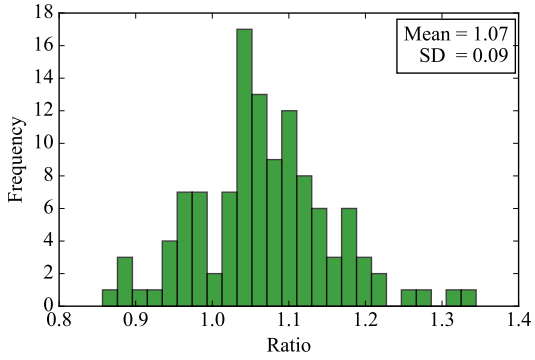

(f) Histogram of expected ratio for C_{10}

Figure 2.9: Contribution of serial dependency for three extreme precipitation events.

not affect the result a lot. Note that the contribution of serial dependency may vary depending on the area of study. Studying the serial dependency in other areas is an interesting future direction.

2.5 Case Study: Comparative Extreme Precipitation Analysis of Three US cities

In this section, a detailed comparative study is further performed on three cities across the US. The comparison is focused on 1) studying the differences of extreme precipitation between three cities, 2) analyzing new extreme precipitation events introduced with a focus on climate change, and 3) studying the effect of serial dependency on different events over different periods.

2.5.1 Representative Extreme Precipitation Events

Compared to the previous section, three additional extreme precipitation events, including T_l, D_p, and W_l, are studied, to fully study more aspects of extreme precipitation. All values are computed for each year and compared in time series to see how they change as the effect of climate change. The detailed definitions, units, and values used in the case study are also listed in Table 2.6.

It is worth noting that different events in the above table measure different aspects of the extremity of daily precipitation. For example, T_l shows the absolute extremity of an area: high value means heavier precipitation, regardless of the average precipitation level; on the other hand, D_p shows the relative extremity of an area. It shows how the precipitation is distributed in a year. Particularly, an area with a lower value of T_l may have a higher value of D_p; this corresponds to a case where an area has less precipitation but the daily precipitation distribution is highly

Event	Definition	Unit	Case Study
M	Maximum daily precipitation in a year	mm	M
T_l	Total amount of precipitation of top l most heavy-rain days in a year	mm	T_{15}
W_l	Maximum total precipitation from any consecutive l days in a year	mm	W_2,W_7
E_k	Number of days with daily precipitation exceeding k mm in a year	mm	E_{15},E_{30}
C_k	Maximum number of consecutive days with precipitation exceeding k mm in a year	day	C_{10}
D_p	Least number of days with total precipitation more than p percent of annual precipitation	day	$D_{0.5}$

Table 2.6: Definitions of extreme precipitation events studied.

skewed. Due to this fact, the overall extremity of an area is application-dependent and requires a case-by-case evaluation.

2.5.2 Data Selection

Three areas are selected for analysis, including the Washington metropolitan area (DC), New York City (NYC), and San Francisco (SFO). All data are downloaded from the National Oceanic and Atmospheric Administration (NOAA) and further cleaned up for this analysis. Data from all stationed in the past 11 decades are used for the analysis to show the applicability of the methods in a long period of time. Missing and invalid data are excluded from the analysis. For each area, a representative station is selected, of which the data is excluded from the analysis. Instead, it is used to compare against the analysis. Excluding it from the analysis makes sure that our analysis is valid and that it does not "use the data to analyze itself". Data from other stations are used to fit a single set of parameters per year,

which later were used in the analysis. Important details of the data used are shown in Table 2.7. The geographic distributions of all stations used in this study are also shown in Figure 2.10.

Area	New York (NYC)	Washington (DC)	San Francisco (SFO)
Number of station	205	332	149
Longitude Range	[-74.483, -73.317]	[-77.6, -76.443]	[-122.717, -121.875]
Latitude Range	[40.267, 41.15]	[38.467, 39.633]	[37.375, 38.210]
Representative Station ID	USW00094728	USC00185111	USW00023272
Analysis Period	1900 - 2015	1900 - 2015	1921 - 2015

Table 2.7: Detailed information about the areas and stations to study.

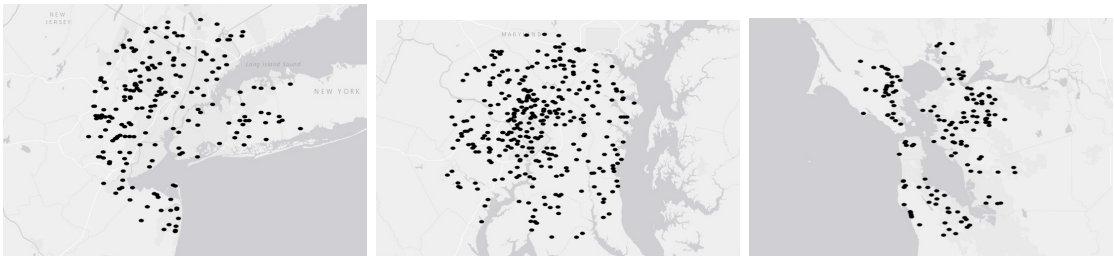

(a) New York (NYC) (b) Washington (DC) (c) San Francisco (SFO)

Figure 2.10: Geographic distributions of stations in areas studied.

2.5.3 Comparative Analysis

For each area and each year, all daily precipitation data except the representative station are selected to compute parameters in the non-stationary with serial dependency model. The comparison between the model with serial dependency and the one without serial dependency is studied at the end of this section. The analysis presented here does not consider seasonal variations. Exploring the effect of seasonal variations on the results can be an interesting future pursuit. These parameters include the probability that one day is wet, the conditional probability of raining

given the state of the previous day, as well as the cumulative distribution of the daily precipitation given the state of the previous day. The distributions of various extreme events are then computed or simulated. To evaluate the accuracy of the model, the outcome is then compared to the representative station: if the distribution from the analysis is close to the distribution from the representative station, then it indicates that the methods are accurate and suitable for future projection.

The characteristics of extreme precipitation between NYC, DC and SFO are also studied. In particular, three basic extreme events and three newly defined extreme events as described above are studied and compared on these areas. In summary, it is found that the extremity of precipitation is about the same level between NYC and DC. However, due to the difference in geographic characteristics, the extreme precipitation in SFO behaves differently. In the remainder of this section, detailed analysis and comparison are discussed for all six extreme precipitation events, assuming a non-stationary model with serial dependency. In Figure 2.11, the solid line and shaded areas represent the analytical distribution of annual maximum daily precipitation (M) in history in the DC area. In detail, the solid line is the expected maximum daily precipitation in a year. The light and dark areas indicate 5th to 95th percentile and 20th to 80th percentile respectively. The dash line shows the observed data from the representative station in the area. From this figure, the dash line matches the expectation closely and falls within the range of 20th to 80th percentile. This validates the accuracy of the non-stationary with serial dependency model. Figure 2.11 (b) can be interpreted similarly to Figure 2.11 (a) except that it is generated using the data from New York City. Comparing the observation from

the representative station and the analytical distribution, it is found that they also match closely. Comparing Figure 2.11 (a) and Figure 2.11 (b), it is found that generally speaking, the annual maximum daily precipitation for both DC and NYC are within a similar range. However, the variation of observed data is higher in NYC than DC. Figure 2.11 (c) shows extreme precipitation event M for SFO, which has much lower value compared to the results in NYC and DC.

Figure 2.12 shows the total amount of precipitation of the top 15 most heavy-rain days in each previous year (T_{15}) for the three selected areas. These figures again prove the accuracy of the non-stationary with serial dependency model. On an average level, the total amount of top 15-day precipitation is in the range between 400 mm and 600 mm for both DC and NYC. The values in NYC, however, are slightly higher than DC, which indicates that the precipitation is more extreme. SFO has much lower values due to the geographical difference.

The last extreme precipitation indicator W_l is shown in Figure 2.13. In particular, W_2 and W_7 are picked for analysis for these three areas. From these figures, it is found that the variation of representative data in NYC is a little bit higher than that in DC and SFO. Further, the 2-day and 7-day total precipitation in SFO is much less extreme than the other two cities.

Figure 2.14 presents another extreme precipitation event E_k. Specifically, two thresholds are selected for analysis: E_{15} and E_{30}, representing the number of days with daily precipitation greater than 15 mm and 30 mm on an annual basis, respectively. On average, the number of days with daily precipitation greater than 30 mm is 12 days for the past 11 decades in both DC and NYC. The same indicator has

values around 5 days, much lower than DC and NYC. This means that from the absolute sense, the precipitation in SFO is less extreme. However, since SFO has less precipitation on average, it does not mean that the distribution is less uniform.

Similarly, Figure 2.15 shows the maximum number of consecutive days with daily precipitation greater than 10 mm (C_{10}). From these figures, one can observe that on an average level, the maximum number of consecutive days with precipitation greater than 10 mm is 2 to 5 days, for NYC, DC, and SFO. There is no obvious increasing trend in the time history.

Figure 2.16 shows the least number of days with total precipitation more than half (50%) of annual total precipitation ($D_{0.5}$) in each year. Somewhat surprisingly, for most years studied, precipitation from less than 18 days in a year contributes to more than half of the total annual precipitation. The values for DC and NYC are within the same range on average, and the values for SFO is lower than these two areas. This indicates that the precipitation in SFO is distributed less uniformly than the other two cities, and thus relatively more extreme than the other two cities.

Summary of Key Observations. From the above analysis, the following key observations can be made:

1. For all events examined, the model performs well and is able to produce accurate results in general for all cities for different precipitation extremity.

2. It is observed that, for all three cities and all extreme precipitation events, an increasing trend can generally be observed starting from the year 1960, although the rate of increase varies. It means that the effect of climate change

also impacts the extremity of precipitation.

3. It is known that the average precipitation in SFO is much lower than the other two cities. However, it does not necessarily mean that the precipitation in SFO is less extreme. It can be observed that for some extreme precipitation events, for example, M and C_{10}, SFO is as extreme as other cities. For other events, for example, E_{15}, $D_{0.5}$, and W_2, SFO has a lower value.

4. Although climate change is observed in all cities, different cities are affected to different extent in terms of how extremity of precipitation changes.

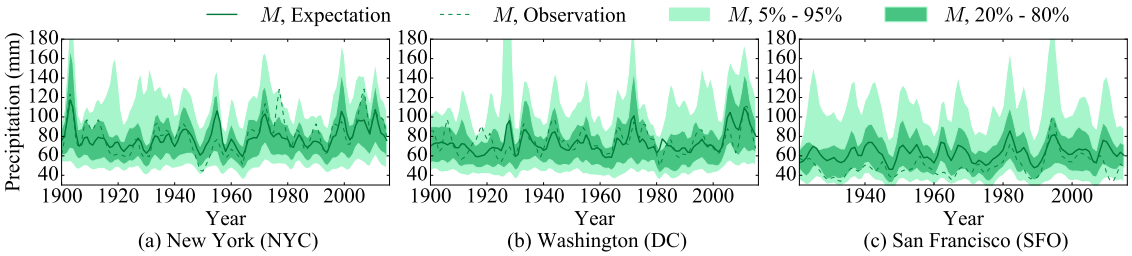

Figure 2.11: Analytical distribution of M generated from model vs. observation from the selected station.

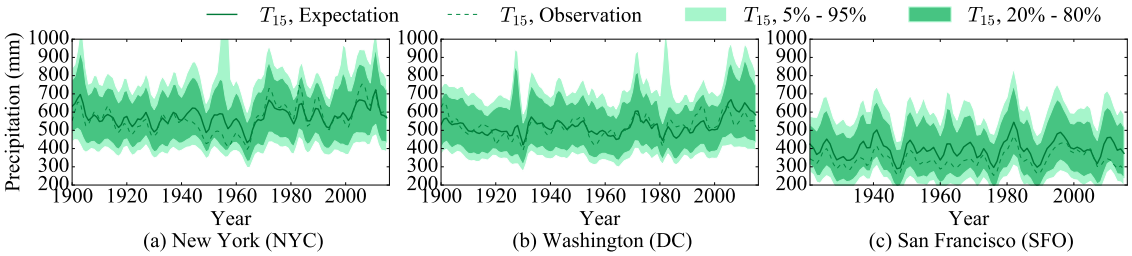

.

Figure 2.12: Analytical distribution of T_{15} generated from model vs. observation from the selected station

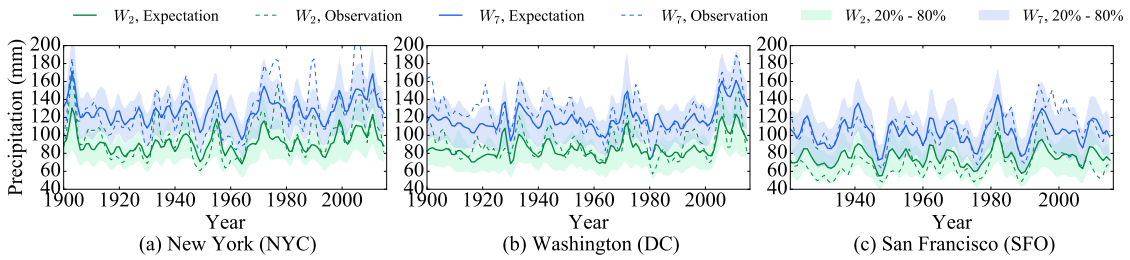

Figure 2.13: Analytical distribution of W_2 and W_7 generated from model vs. observation from the selected station.

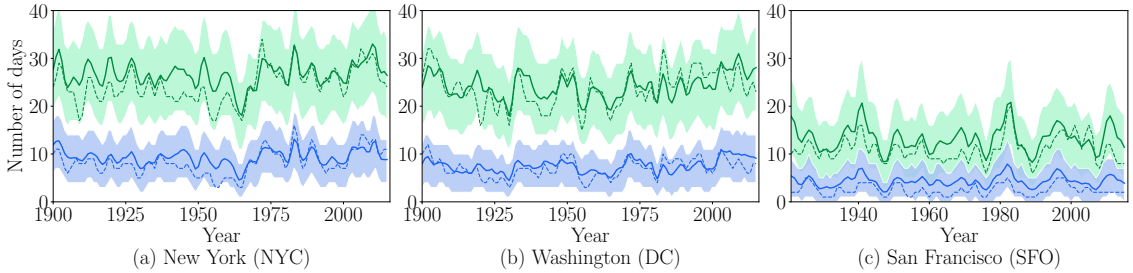

Figure 2.14: Analytical distribution of E_{15} and E_{30} generated from model vs. observation from the selected station.

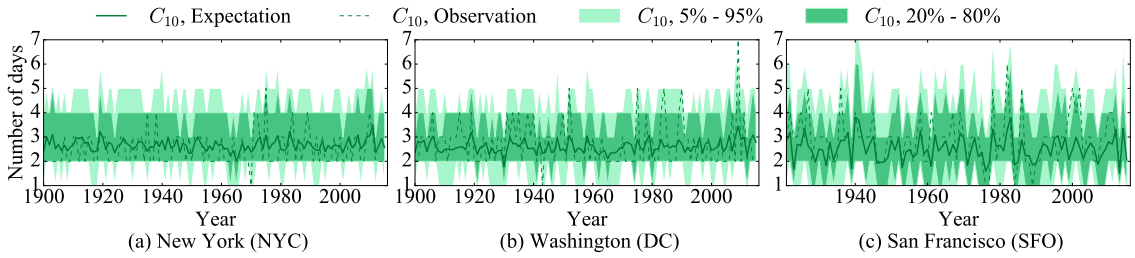

Figure 2.15: Analytical distribution of C_{10} generated from model vs. observation from the selected station.

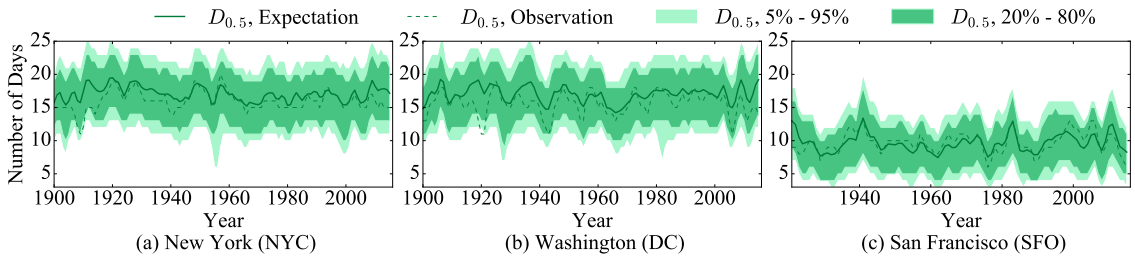

Figure 2.16: Analytical distribution of $D_{0.5}$ generated from model vs. observation from the selected station.

2.5.4 Effectiveness of Serial Dependency

To look into how serial dependency affects the accuracy of the analysis, the ratio of impact are calculated and studied.

$$\text{ratio} = \frac{\text{Results with serial dependency}}{\text{Results without serial dependency}} \tag{2.36}$$

Ratios for all six extreme precipitation events from three cities are calculated and summarized in the Table 2.8. From the table, it can be observed that, for some extreme events, serial dependency does not have a huge impact on the accuracy of the analysis, while for some other extreme events, serial dependency is crucial to be included. In detail, M, E_{15}, T_{15}, $D_{0.5}$ do not rely on serial dependency, where considering serial dependency only improves the results by a small margin. On the other hand, for C_{10} and W_2, considering serial dependency is important for an accurate analysis: up to 50% improvement is observed for SFO, and 10% improvement can be observed for other cities or events too. Compare these two sets of extreme precipitation events, an important difference can be observed: the first set of indicators describe extreme daily precipitation at the scale of a year; while the second set of indicators focus more on a short period, for example, 2-day extreme precipitation or weekly extreme precipitation. When a short period of time is concerned, serial dependency is of huge importance.

To further study how serial dependency affects the accuracy of the analysis, an additional analysis is performed. For different value of l, the analysis on W_l both

with serial dependency and without serial dependency is performed and the ratio of impact is calculated. Figure 2.17 shows the ratio of impact with different value of l for all three cities. It can be seen that when considering W_l for a short period of time, for example within a week, the ratio of impact is high, indicating that the serial dependency affects the analysis a lot. When considering a period of 3 months or more, such effect is much less. Since for most cases, the main concern of extreme precipitation is when a great amount of precipitation happens in a short period of time, serial dependency is generally important.

	New York (NYC)		Washington (DC)		San Francisco (SFO)	
	Mean	SD	Mean	SD	Mean	SD
M	1.0017	0.0148	0.9984	0.0201	1.0021	0.0175
T_{15}	1.0005	0.0075	0.9996	0.008	1.0019	20.0092
W_2	**1.0408**	0.0249	**1.0559**	0.0284	**1.1262**	0.0305
E_{15}	1.0018	0.0091	1.0011	0.0093	1.0126	0.0137
C_{10}	**1.1283**	0.0461	**1.141**	0.051	**1.5138**	0.1164
$D_{0.5}$	1.0012	0.0061	1.0018	0.0074	1.0093	0.0119

Table 2.8: Prediction of extreme events $(M, E_{15}, E_{30}, C_{10})$ in future years based on non-stationary model with serial dependency. (SD stands for standard derivation.)

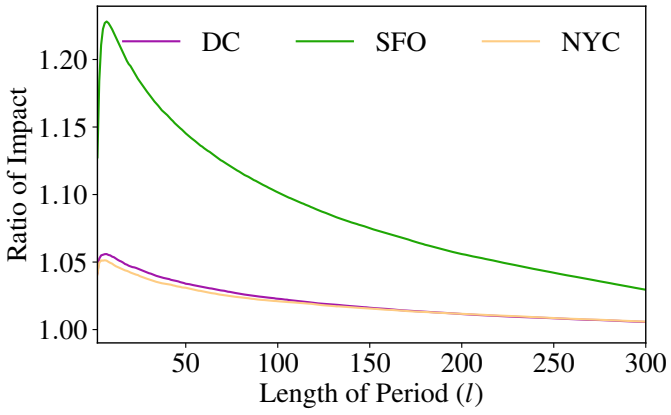

Figure 2.17: Ratio of impact of W_l for different values of l and all three cities.

2.6 Discussions and Conclusions

This chapter focus on how to accurately analyze various extreme precipitation events using information based on non-extreme precipitation, which is much easier to obtain. The proposed methods are based on a non-stationary assumption with or without serial dependency, both of which capture the effect of changing climate. The methods use Markov models and techniques related to dynamic optimization so that exact distributions of various extreme events can be computed.

The proposed methods provide accurate analysis for the last 10 decades and future prediction. The case study shows that non-stationary models capture changing climate much better than the stationary model. Further evaluation also reveals strong evidence about the existence of serial dependency in the area of study. It shows that the non-stationary model with serial dependency further increases the accuracy for extreme analysis by up to 16%.

Chapter 3: Extreme Precipitation Projection: Copula and Downscaling

3.1 Overview

Chapter 2 discussed how serial dependency helps to improve extreme precipitation analysis. This chapter instead focuses on improving extreme precipitation projection using copulas for serial dependency. Most existing works on future extreme precipitation are based on the Global Climate Models (GCMs), or downscaled GCMs, none of which are designed specifically for extreme climate. The results of this chapter improve the accuracy for extreme precipitation from downscaled GCMs using copulas. The content of this chapter is based on a paper accepted to ASCE Journal of Hydrologic Engineering [94].

As mentioned in Chapter 1, climate change influences human life in every aspects [5, 95]. One important countermeasure to mitigate impacts of extreme precipitation and reduce its potential risk is preventative protection, e.g., strengthening design standards to factor in the effect of increasing extreme precipitation[96]. However, this approach is effective only if an accurate and long-term projection of extreme precipitation is available as a guideline. To address this issue, the Coupled

Model Intercomparison Project (CMIP) was initiated to incorporate climate change in the design of Global Climate Models (GCMs) for the 21-th century. Since then, numerous GCMs have been proposed and studied [43, 44, 45, 97, 98]. These GCMs provide results for each Representative Concentration Pathways (RCPs).

The primary goal of this chapter is to propose a systemic way to evaluate, analyze and improve existing downscaling GCMs results for better analysis of extreme precipitation. The method relies on the underlying GCMs to consider physical effect of the climatology. In the following sections, details of the methodology are discussed with necessary background knowledge. To validate this method, it is further applied to historical observed data in the Washington metropolitan area. It is shown that the assumptions based in this work are true even over a long period of time, and that the improvement leads to a huge reduction on the analysis error.

3.2 Background and Literature Review

Climate downscaling refers to the procedure that maps global trend of climate to a local trend with more geographic-related details. Most of these approaches can be categorized into two classes: 1) dynamic downscaling, where high solution simulation is performed on the region of interests to extrapolate the fine-grind effect from global GCMs [99, 100, 101]; and 2) statistical downscaling, where different statistical methods are used to capture the statistical relationship between global climate models and the behavior in the local area. [102, 66, 103] These two methods have different features:

- Dynamic downscaling is able to incorporate physical principles into the analysis easily, but are computationally intensive and sensitive to bias.

- Statistical downscaling are much efficient but requires that the statistical model learned from history applies to the future climate .

This chapter mainly focuses on methods based on statistical downscaling. A lot of different statistical downscaling methods has been proposed in the recent years [49, 50, 51], including bias correction with spatial disaggregation (BCSD), bias correction with constructed analogs (BCCA), global daily downscaled projections (GDDP), localized constructed analogs (LOCA), multivariate adaptive constructed analogs (MACA), etc. Note that other classification of downscaling methods also exists. For example, [104] categorizes downscaling techniques as deterministic [105], semi-deterministic [106] and stochastic approaches.

All downscaling methods follow a similar high-level approach as follows [49, 50, 51]:

1. Regridding. This step reinterprets GCM results and maps them into a smaller scale directly.

2. Bias correction. Results in all grids are aligned using observed history as a baseline. One popular method for bias correction is quantile mapping.

3. Spatial Downscaling. This step incorporates geographic influence into consideration. The three downscaling methods studied in this work mainly differ in this step.

3.3 Methodology

This study presents a new framework to project extreme precipitation based on downscaled GCM and mathematical concept called copulas (See Appendix C for more details on copulas). Figure 3.1 illustrates the overall structure of methodology. The high-level ideas are summarized as follows.

1. First, eighteen state-of-the-art downscaled GCM results are compared against observed data in the context of extreme precipitation. The assessment reveals that existing downscaled GCMs do not reproduce observed extreme precipitation, and therefore do not project appropriately future extremes.

2. Then, a copula-based method is applied to explore possible ways to improve downscaled GCM results for better analysis and projection of extreme precipitation. The results show that marginal distributions of daily precipitation extracted from downscaled GCM results are relatively accurate. However, the day-to-day serial dependency copulas from downscaled GCMs differ significantly compared to the one from observed data.

3. Finally, further analysis of observed data shows that, although the distribution of daily precipitation changes over years, the underlying copula model stays unchanged even over a long period. Based on this observation, a proposed model that combines marginal distribution from downscaled GCM results and the copula from observed data. This new model reduces the error for extreme precipitation analysis and is used to perform future extreme precipitation pro-

jection.

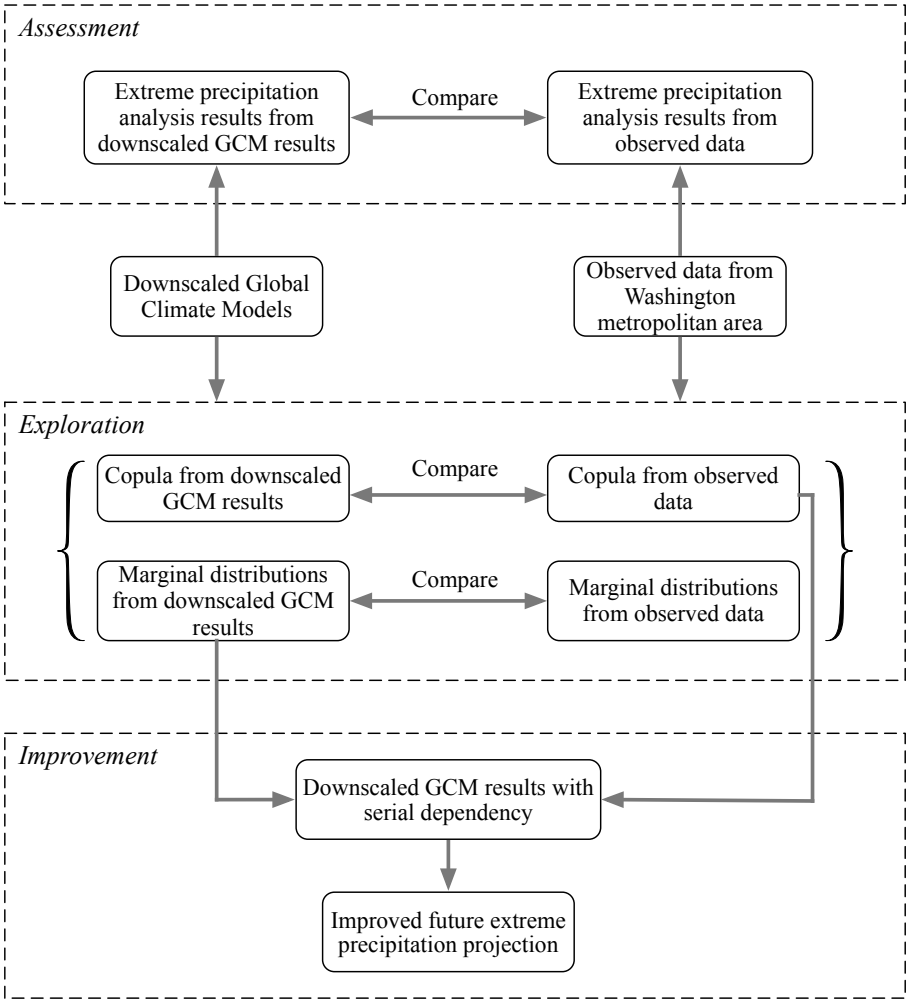

Figure 3.1: The assessment-exploration-improvement framework for extreme precipitation analysis and projection with serial dependency. **Assessment**: Downscaled GCM results and observed data are both used for extreme precipitation analysis, and the analysis results are compared to assess the accuracy. **Exploration**: Marginal distributions and day-to-day serial dependency copulas are extracted from downscaled GCM results separately. Their accuracy are compared against real ones. **Improvement**: Historical copulas and projected marginal distributions are combined for better analysis and projecting extreme precipitation.

3.3.1 Historical Assessment

3.3.1.1 GCMs and Downscaling GCMs

The assessment is based on three downscaling methods: GDDP, MACA, and LOCA with datasets available to access from different sources. Details about the three datasets can be found in Appendix E. Although there are more than 15 GCMs in CMIP5, each downscaling method studies a different subset of them. To be able to compare across all three GCMs, this work focuses on GCMs that have downscaled results available for all three methods. As a result, six GCMs are selected, and the details of them are summarized in Table 3.1.

Model acronym	Model full name	Institution
CCSM4	CCSM4	National Center for Atmospheric Research (NCAR), USA
MIROC	MIROC-ESM-CHEM	The University of Tokyo and National Institute for Environmental Studies, Japan
GFDL	GFDL-ESM2G	Geophysical Fluid Dynamics Laboratory, USA
CNRM	CNRM-CM5	Centre National de Recherches Meteorologiques, Meteo-France, France
CSIRO	CSIRO-Mk3-6-0	Commonwealth Scientific and Industrial Research Organization, Australia
CanESM2	CanESM2	Canadian Centre for Climate Modeling and Analysis, Canada

Table 3.1: Six Global Climate Models studied

3.3.1.2 Extreme Precipitation Indices

Previous work studied various aspects of precipitation by comparing methods for downscaling GCM results. Wilby et al. [107], for example, studied the average,

median, and standard deviation of daily precipitation, and different conditional and unconditional probabilities of raining. These precipitation indices do not represent extreme precipitation cases. Even for those that studied extreme precipitation [40, 85], it was largely restricted to maximum daily precipitation. However, it describes one of its aspects only and multiple indices are necessary in order to fully characterize extreme precipitation events. For example, in the context of flooding, the amount of precipitation across multiple days is a more important indicator of the underlying risk.

To this end, the assessment in the work is based on six different extreme precipitation indices: Max, M2d, R20mm, CWD, LDP0.5 and LDP0.25. Details of these indices are summarized in Table 3.2. Among these six indices, R20mm and CWD are also used in the Expert Team on Climate Change Detection and Indices (ETCCDI) [108]. The first four indices do not fully describe how extreme the precipitation is within a year. For example, the index value of a tropical city may be much higher than a city near a desert. However, it does not necessarily mean that the tropical city has more extreme precipitation. A more meaningful index should show how concentrate the precipitation is in a year. To reflect this fact, another two indices (LDP0.5 and LDP0.25) are also studied.

In addition to maximum daily precipitation (Max) that is commonly used in previous works, other indices also describe key aspects of extreme precipitation. For example, M2d represents scenarios where a large amount of precipitation happening in a short period of time (2 days). R20mm measures the number of days in a year with heavy daily precipitation. LDP0.5 and LDP0.25 measure in one year the

Index	Explanation
Max	Maximum daily precipitation within a year
M2d	Maximum 2-consecutive day precipitation within a year
R20mm	Annual count of days when precipitation $\geq$ 20mm
CWD	Maximum number of consecutive wet days within a year
LDP0.5	Least number of days with total precipitation more than half of annual precipitation
LDP0.25	Least number of days with total precipitation more than 25% of annual precipitation

Table 3.2: Six extreme precipitation indices studied

extent of skewness in the daily precipitation distribution is. Lower values of these latter indices mean that the distributions are more skew, which means that the precipitation is more extreme with higher variance.

3.3.1.3 Error Metrics for Quantitative Comparison

To completely assess extreme precipitation results across all combinations of GCMs and downscaling methods, relative error metrics across time series are computed. Note that by computing error metrics across the whole time series, it integrates the uncertainty in the prediction for the whole history. Two error metrics are used to measure the accuracy of each downscaled GCM in the context of extreme precipitation. Denoting the observation value for each year in time series as $o_1, \ldots, o_n$ and the downscaled values in time series as $d_1, \ldots, d_n$, the normalized mean absolute error (NMAE) is defined as follows:

$$\text{NMAE} = \frac{\frac{\sum_{i=1}^{n} |d_i - o_i|}{n}}{\frac{\sum_{i=1}^{n} o_i}{n}} \tag{3.1}$$

The normalized root-mean-square error (NRMSE) is defined as follows:

$$\text{NRMSE} = \frac{\sqrt{\frac{\sum_{i=1}^{n}(d_i - o_i)^2}{n}}}{\frac{\sum_{i=1}^{n} o_i}{n}} \tag{3.2}$$

Both NMAE and NRMSE are popular measures of the differences between values predicted by a model and the values actually observed. The values of these two error metrics have a range from 0 to positive infinity, with smaller values indicating higher accuracy. Note that these error calculations are also important metrics to measure goodness-of-fit between analytical results and the observed results [109, 110, 111]. For example, compared to R^2, NRMSE uses the average of observation values as the normalization factor instead of the variance.

3.3.2 Exploration of Marginal Distribution and Serial Dependency

This work features in a creative way to use copula to analyze precipitation distribution. In addition to the marginal distribution of the precipitation, day-to-day dependency is also taken into consideration. The dependency is incorporated into the analysis based on copula.

There are many applications of copula for hydrological analysis [112, 113, 114, 115]. Here copula is used to study serial dependency in extreme precipitation analysis. Note that all properties of extreme precipitation can be fully described using a joint distribution of all daily precipitation random variables in a year. However, such a 365-dimension joint distribution (assuming non-leap year) is too complex to analyze. In this study, it is assumed that the precipitation in a day depends on

its previous day, therefore day-to-day serial dependency represented as a bivariate copula, and marginal distribution of the whole year together can describe the whole process. Previous works [77] have demonstrated that two-day dependency can already lead to high accuracy. However, the method proposed here can be generalized to copula with higher dimensions if necessary.

Note that here copulas are computed on a yearly basis, which assumes that the copula stays stationary within a year. It is left as a future work to extend the analysis to a seasonal basis and study the variation between different seasons.

3.3.3 Improvements of Extreme Precipitation Projection based on Copulas

This section focuses on the approach used to improve the accuracy of extreme precipitation analysis based on downscaled GCM results, using theories of copula.

3.3.3.1 Stationarity of Historical Copulas

The key idea behind the improvement is the observation that copula and marginal distribution are completely decoupled. Therefore, if copula stays stationary over the time, it is possible to replace the inaccurate copula by the historical copula, which is accurate. To be more specific, for any bivariate distribution between X_1 and X_2, the marginal distributions are completely decoupled and independent from the copula of X_1 and X_2. Therefore, a bivariate distribution can be determined from the marginal distribution and the copula. The previous section demonstrated that

it is mainly the copula that causes inaccuracy in the results. Therefore one effective way to improve the downscaling results is to replace the inaccurate copula model to an accurate copula model as determined in this work.

In more detail, let $F_{X_1,X_2}(x_1, x_2)$ be the joint distribution between first-day precipitation and second-day precipitation. Let $F(x)$ be the marginal distribution of the first day and the second day. Note that this work does not consider a seasonal variation of precipitation within a year, therefore the marginal distribution of any day follows the same distribution. Now the copula for X_1 and X_2 can be written as

$$C_{X_1,X_2}(u_1, u_2) = \Pr(F(X_1) \leq u_1, F(X_2) \leq u_2) \tag{3.3}$$

Assuming that an unbiased and accurate projection of marginal distribution is $F'(\cdot)$ and that the real copula is $C_{X_1,X_2}(u_1, u_2)$, an approximation of the joint distribution can be obtained via:

$$F'_{X_1,X_2}(x_1, x_2) = C_{X_1,X_2}(F'(x_1), F'(x_2)) \tag{3.4}$$

$F'_{X_1,X_2}(\cdot, \cdot)$ is an unbiased and accurate approximation of $F_{X_1,X_2}(\cdot, \cdot)$, which means that replacing the copula in the downscaling methods to the generated one in this work results in an accurate approximation of the joint distribution.

3.3.3.2 Overall Improvement Procedure

The proposed overall procedure is defined by the following steps:

1. Compute marginal distribution. For each year of interests, the marginal distribution is computed using downscaled GCM results. Note that an empirical marginal distribution is usually not accurate enough for prediction due to lack of data, therefore, interpolation based on Gamma distribution is used to enhance accuracy. The Gamma distribution is a commonly used tool in statistical analysis of precipitation to model the marginal distribution of precipitation. [91, 116]. It is popularly used in modeling precipitation due to its accuracy and applicability.

2. Compute an empirical copula. Given the historical data at a small region, compute an empirical copula based on the data. This empirical copula can be used both for validation as well as future projection.

3. Monte Carlo simulation. Now given the above result, Monte Carlo simulation can be used to produce an improved projection for each GCM. The crucial part here is how to simulate the second-day precipitation given the first-day precipitation. This is done further in three steps:

   (a) Perform probability integral transformation on the first-day precipitation to obtain transformed values.

   (b) Using these values to find the corresponding marginal distribution from the empirical copula computed in the previous step. Sample uniformly one value from that marginal distribution.

   (c) Perform an inverse transform sampling using the marginal distribution

and the value obtained above.

3.4 Case Study and Results

3.4.1 Details of the Study Area

Our study focuses on the Washington metropolitan area and the observation station is located at Ronald Reagan Washington National Airport (DCA), with station number USW00013743. Daily precipitation data are obtained from the National Oceanic and Atmospheric Administration (NOAA). Although observed station data is available up to the year 2017, downscaling results are available only up to the year 1995, therefore this study focuses on the period from 1950 to 1995. According to the data explanation document from NOAA, the daily precipitation data collected by NOAA include rainfall and melted frozen rainfall but not snowfall. Figure 3.2 shows the location of the selected observation station.

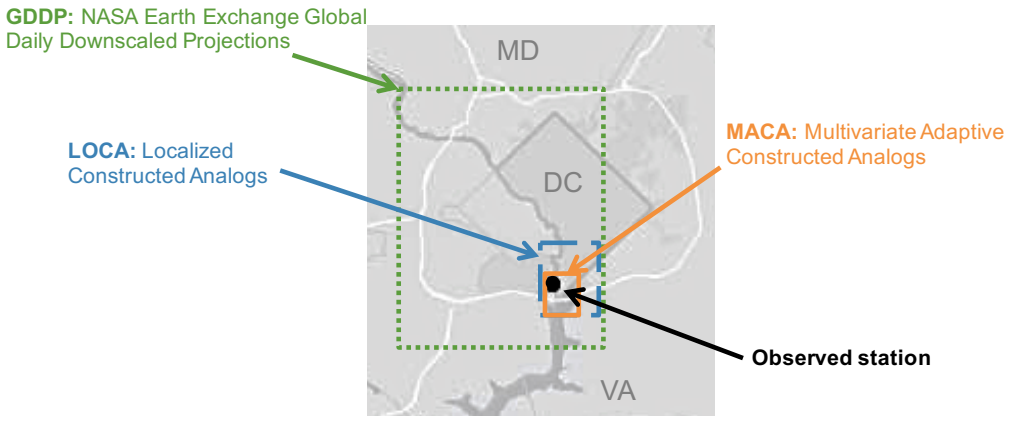

Figure 3.2: Spatial locations of observed station and three different downscaled grids in the Washington metropolitan area.

Figure 3.2 also shows the grid sizes of the three downscaled model mentioned

above. The observation station is covered by all three downscaled grids with different sizes. In particular, MACA method provides the highest resolution while GDDP method provides the lowest resolution among three downscaling methods.

3.4.2 Historical Assessment

3.4.2.1 Time Series Comparison

This work analyzes three downscaling methods each combined with six GCMs. Due to space limitation, the presentation focuses on the time series comparison of two GCMs: CCSM4 and MIROC, that is, 6 combinations of downscaled GCMs: CCSM4-GDDP, CCSM4-LOCA, CCSM4-MACA, MIROC-GDDP, MIROC-LOCA, and MIROC-MACA. For example, CCSM4-GDDP refers to GDDP downscaling method applied on top of CCSM4 Global Climate Model.

Figure 3.3 shows the comparison among observed results and each downscaled GCM results based on CCSM4 model. Similar results based on MIROC model is shown in Figure 3.4. In each figure, solid lines represent an extreme precipitation index computed from the observed data; dotted lines represent the same extreme precipitation index computed from the downscaled GCM results.

For all combinations of downscaling methods and GCMs, the analysis results differ greatly compared to the observed results especially for extreme precipitation indices CWD, LDP0.5 and LDP0.25. Some combination of GCM and downscaling method produces particularly inaccurate results, for example, MIROC-GDDP has the lowest accuracy for almost all indices compared to others. Some other combina-

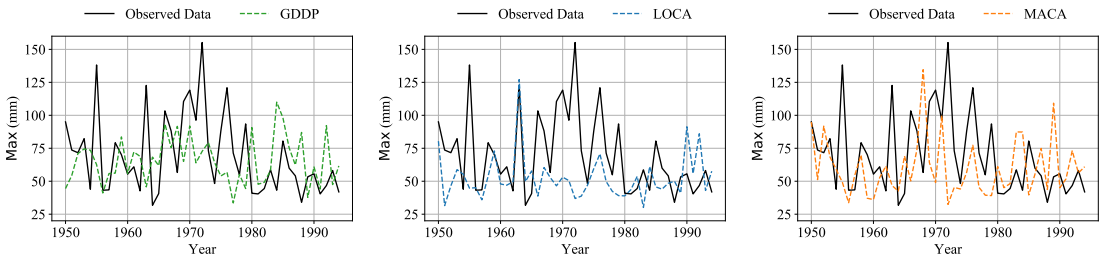

(a) Annual maximum daily precipitation (Max)

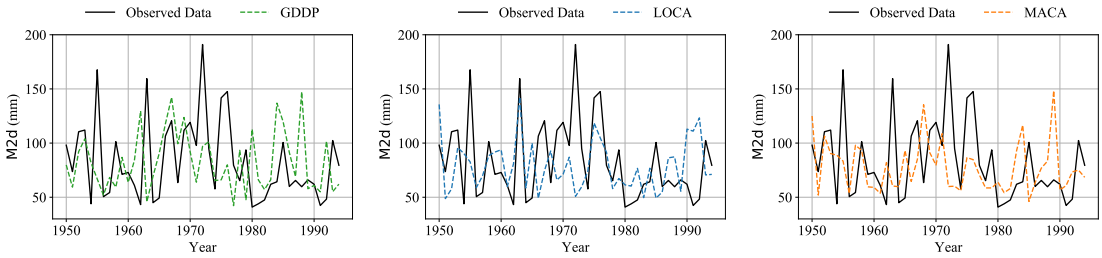

(b) Annual maximum 2-consecutive day precipitation (M2d)

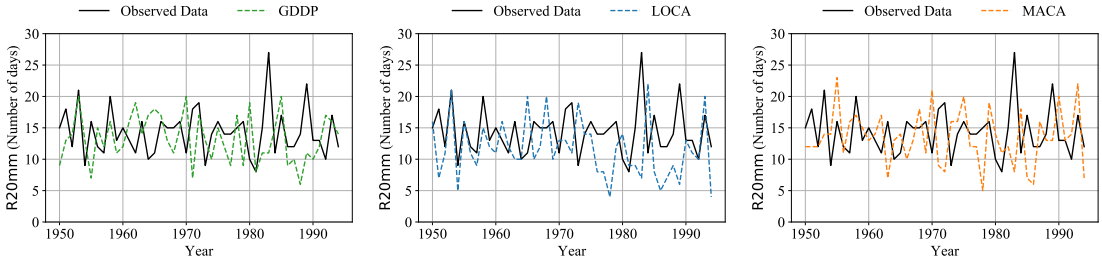

(c) Annual count of days when precipitation $\geq$ 20mm (R20mm)

Figure 3.3: Comparison of historical extreme precipitation performance among observed data (solid lines) and three different downscaled data (dashed lines) from CCSM4 Global Climate Model.

tion, for example, MIROC-MACA, produces overall better results than other cases. In the remainder of this section, four figures are analyzed in detail and interpreted for illustration. Other figures can be interpreted similarly.

Figure 3.3a shows the annual maximum daily precipitation (Max) computed from observed data and three downscaled GCM data. In these three figures, CCSM4-MACA combination produces the closest results to observed values compared to CCSM4-GDDP and CCSM4-LOCA. In the middle figure, it can also be noted that

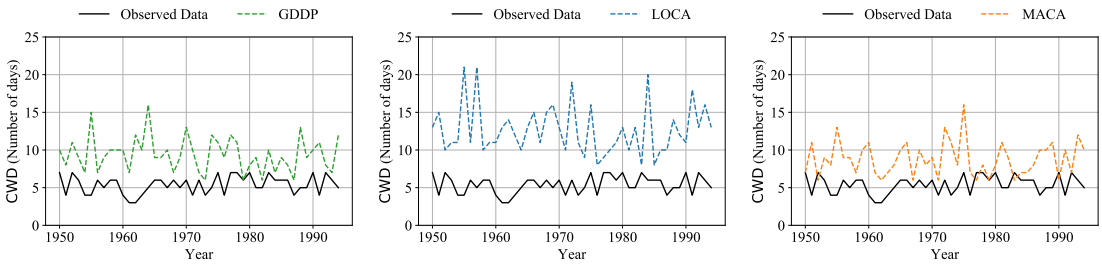

(d) Annual maximum number of consecutive wet days (CWD)

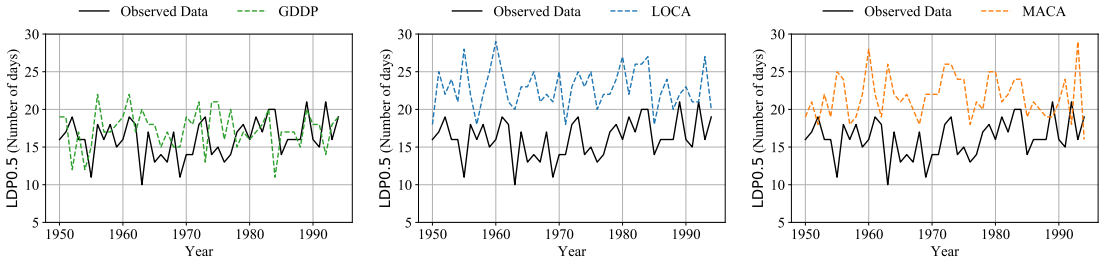

(e) Least number of days with total precipitation more than half of annual precipitation (LDP0.5)

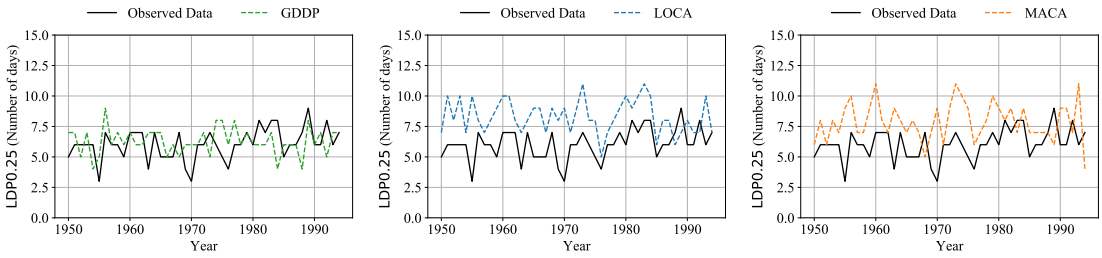

(f) Least number of days with total precipitation more than 25% of annual precipitation (LDP0.25)

Figure 3.3: Comparison of historical extreme precipitation performance among observed data (solid lines) and three different downscaled data (dashed lines) from CCSM4 Global Climate Model.

CCSM4-LOCA is not able to predict many peak annual maximum daily precipitations from the year 1950 to 1980. For example, the actual maximum precipitation in 1972 is more than 150 mm; however, the projected annual maximum precipitation from CCSM4-LOCA is round 50 mm. This is an error of about 100 mm. Figure 3.3b shows the annual maximum two-day precipitation and can be interpreted in a similar way as Figure 3.3a.

Figure 3.3c shows the total number of days in a year with precipitation greater than 20 mm, and it shows that all model combinations show great consistency compared to the observed results. However, when it comes to the annual maximum number of wet days as shown in Figure 3.3d, the results is different. Both GDDP and MACA slightly overestimate the results, while LOCA overestimates the results by a huge margin.

Figure 3.3e shows the analysis results of LDP0.5 computed from observed data and from three downscaled GCM data. As shown in the left figure, the results from observed data and CCSM4-GDDP data are closely aligned, which means the combination CCSM4-GDDP produces relatively accurate results for LDP0.5. However, as shown in the middle and right figures, CCSM4-LOCA and CCSM4-MACA do not provide good results for this extreme precipitation index.

Similar analysis can be performed on MIROC and results are presented in Figure 3.4. It is found that the analysis results in Figure 3.4a, Figure 3.4b and Figure 3.4c are similar to the results for CCSM4 as discussed above. However, the results in the other three indices are different. For CWD, it can be found in Figure 3.4d that GDDP is far off the observed results while LOCA and MACA are slightly over-estimated. This is also the case for LDP0.5 and LDP0.25 that GDDP is significantly worse when downscaling MIROC models.

In summary, the accuracy of downscaled GCM results is not high when used for extreme precipitation. The comparison also indicates that the accuracy of extreme analysis highly depends on the combination of downscaling methods and GCMs. Therefore, using existing downscaled GCMs to analyze extreme precipitation is in-

sufficient and can lead to inaccurate results.

GCMs	Downscaling Methods	Max	M2d	R20mm
CanESM2	GDDP	0.49 (0.64)	0.49 (0.64)	0.38 (0.53)
	LOCA	0.47 (0.63)	0.50 (0.64)	0.41 (0.55)
	MACA	0.39 (0.53)	0.40 (0.56)	0.38 (0.50)
CCSM4	GDDP	0.38 (0.50)	0.41 (0.54)	0.38 (0.51)
	LOCA	0.38 (0.52)	0.39 (0.49)	0.42 (0.53)
	MACA	0.41 (0.55)	0.38 (0.51)	0.37 (0.48)
CNRM	GDDP	0.47 (0.62)	0.43 (0.63)	0.46 (0.60)
	LOCA	0.41 (0.56)	0.43 (0.57)	0.44 (0.56)
	MACA	0.45 (0.57)	0.46 (0.61)	0.39 (0.53)
CSIRO	GDDP	0.35 (0.46)	0.38 (0.48)	0.38 (0.49)
	LOCA	0.46 (0.58)	0.47 (0.57)	0.43 (0.55)
	MACA	0.41 (0.54)	0.42 (0.52)	0.37 (0.49)
GFDL	GDDP	0.46 (0.63)	0.46 (0.60)	0.37 (0.52)
	LOCA	0.45 (0.57)	0.49 (0.58)	0.43 (0.55)
	MACA	0.44 (0.58)	0.42 (0.54)	0.37 (0.51)
MIROC	GDDP	0.48 (0.63)	0.44 (0.62)	0.38 (0.55)
	LOCA	0.37 (0.51)	0.45 (0.54)	0.43 (0.50)
	MACA	0.49 (0.64)	0.45 (0.59)	0.40 (0.53)

Note: Underlined values indicate the least error cases per extreme precipitation index.

Table 3.3: Performance of 18 different downscaled GCMs in the context of extreme precipitation using two error metrics: Normalized mean absolute error (NMAE) and normalized root-mean-square error (NRMSE)

3.4.2.2 Quantitative Comparison

Table 3.3 and Table 3.4 shows these two errors metrics for all 18 downscaled GCMs and all six extreme precipitation indices. For each downscaled GCM, the two error metrics for six extreme precipitation indices are computed and presented in the form of NMAE (NRMSE). The results in the CCSM4 and MIROC rows are consistent with results shown in Figure 3.3 and Figure 3.4. For example, GDDP-MIROC

GCMs	Downscaling Methods	CWD	LDP0.5	LDP0.25
CanESM2	GDDP	0.59 (0.66)	6.44 (6.93)	1.35 (1.40)
	LOCA	0.33 (0.44)	1.68 (1.89)	0.42 (0.50)
	MACA	0.31 (0.37)	0.82 (1.00)	0.32 (0.42)
CCSM4	GDDP	0.30 (0.38)	0.75 (0.89)	0.19 (0.24)
	LOCA	0.34 (0.46)	1.34 (1.50)	0.41 (0.46)
	MACA	0.35 (0.43)	0.66 (0.79)	0.37 (0.43)
CNRM	GDDP	0.26 (0.33)	1.25 (1.44)	0.28 (0.36)
	LOCA	0.35 (0.42)	1.47 (1.68)	0.48 (0.55)
	MACA	0.26 (0.33)	0.62 (0.76)	0.34 (0.39)
CSIRO	GDDP	0.33 (0.42)	1.80 (2.04)	0.39 (0.45)
	LOCA	0.34 (0.41)	1.40 (1.55)	0.41 (0.47)
	MACA	0.30 (0.37)	0.61 (0.73)	0.34 (0.41)
GFDL	GDDP	0.43 (0.53)	2.72 (2.93)	0.68 (0.74)
	LOCA	0.30 (0.38)	1.40 (1.66)	0.41 (0.46)
	MACA	0.29 (0.37)	0.59 (0.75)	0.33 (0.38)
MIROC	GDDP	0.57 (0.65)	6.14 (6.59)	1.25 (1.29)
	LOCA	0.33 (0.42)	1.40 (1.57)	0.41 (0.47)
	MACA	0.33 (0.40)	0.58 (0.76)	0.33 (0.38)

Note: Underlined values indicate the least error cases per extreme precipitation index.

Table 3.4: Performance of 18 different downscaled GCMs in the context of extreme precipitation using two error metrics: Normalized mean absolute error (NMAE) and normalized root-mean-square error (NRMSE)

has the highest error for many extreme precipitation indices CWD, LDP0.25, and LDP0.5.

3.4.3 Exploration

3.4.3.1 Marginal Distributions

For each downscaled GCM, the marginal distribution of daily precipitation obtained from downscaled GCM data is compared against the one obtained from the observed

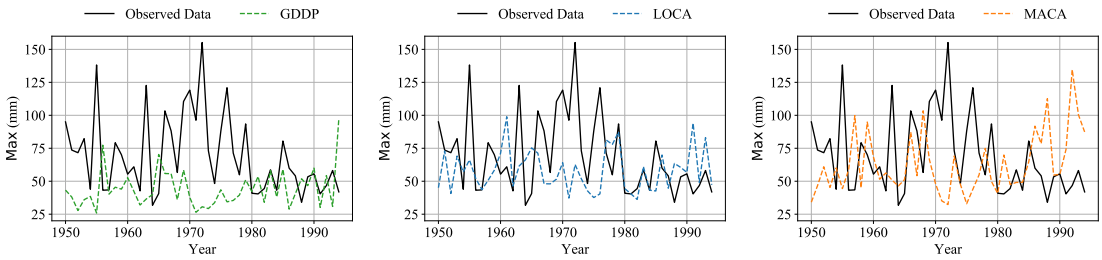

(a) Annual maximum daily precipitation (Max)

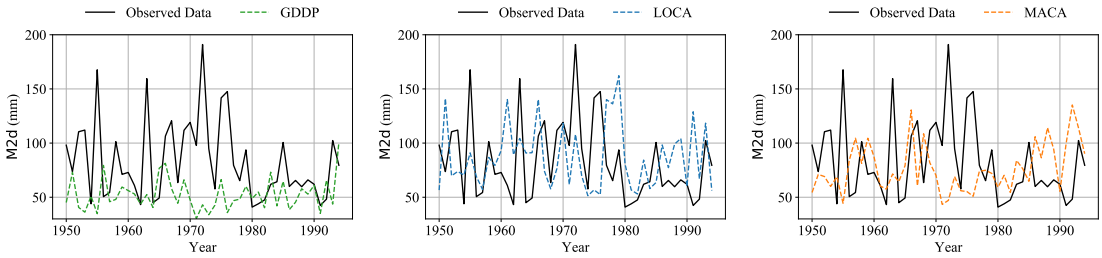

(b) Annual maximum 2-consecutive day precipitation (M2d)

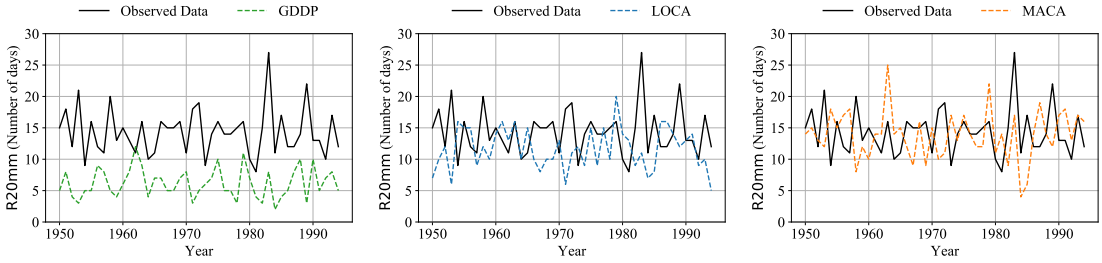

(c) Annual count of days when precipitation $\geq$ 20mm (R20mm)

Figure 3.4: Comparison of historical extreme precipitation performance among observed data (solid lines) and three different downscaled data (dashed lines) from MIROC Global Climate Model.

data. Similar to the previous section, two downscaled GCMs (CCSM4 model and MIROC model) are presented, in Figure 3.5 and Figure 3.6. Each figure is a quantile-quantile plot of daily precipitation for the period from the year 1950 to the year 1995.

According to these figures, dotted lines are slightly below the solid lines, which means that the marginal distributions extracted from downscaled GCM results are slightly less extreme compared to the one obtained from the observed data. However, overall marginal distributions from the downscaled GCM align well with the one

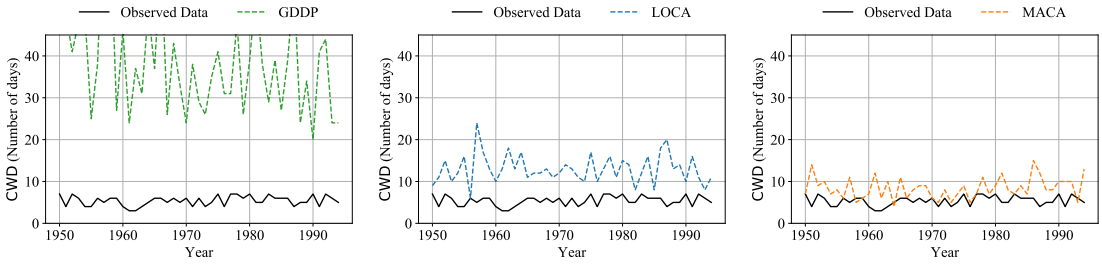

(d) Annual maximum number of consecutive wet days (CWD)

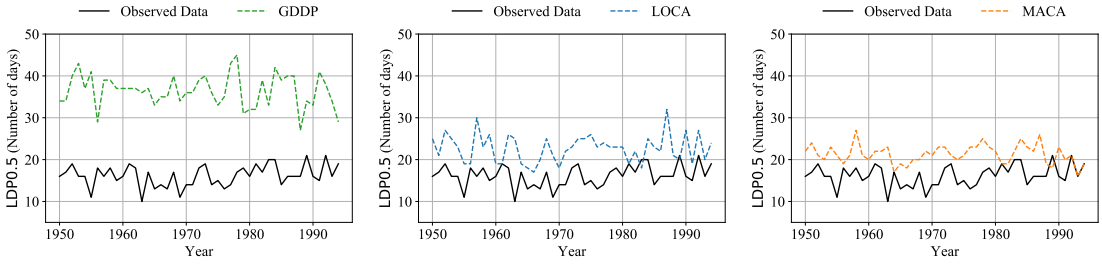

(e) Least number of days with total precipitation more than half of annual precipitation (LDP0.5)

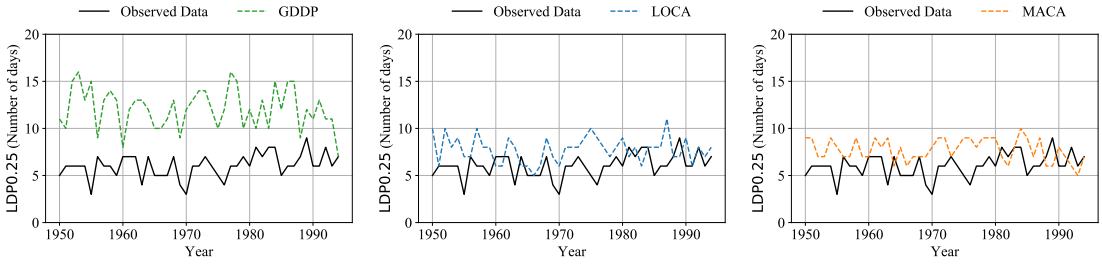

(f) Least number of days with total precipitation more than 25% of annual precipitation (LDP0.25)

Figure 3.4: Comparison of historical extreme precipitation performance among observed data (solid lines) and three different downscaled data (dashed lines) from MIROC Global Climate Model.

from observation. The exception is MIROC-GDDP, which differs significantly from the observation. The comparison indicates that marginal distribution is unlikely to be the main reason for the observed inaccuracy in extreme precipitation results in the previous section.

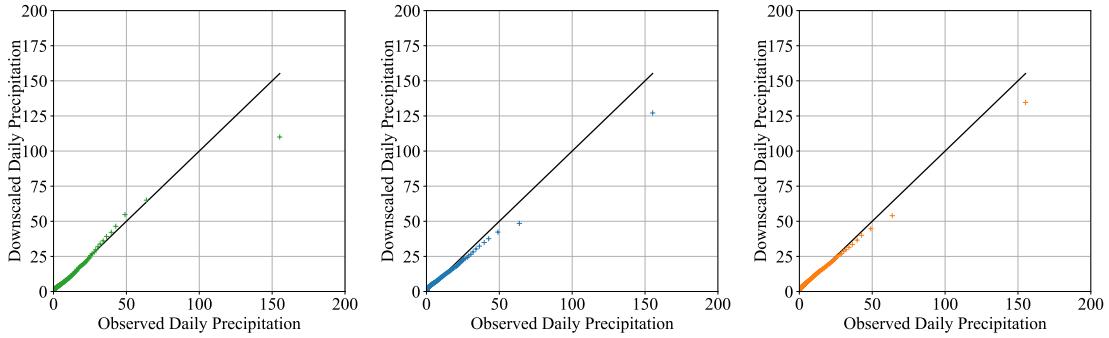

(a) (b) (c)

Figure 3.5: Historical Quantile-Quantile plots of daily precipitation from: (a) observed data vs. CCSM4-GDDP downscaled data; (b) observed data vs. CCSM4-LOCA downscaled data; and (c) observed data vs. CCSM4-MACA downscaled data.

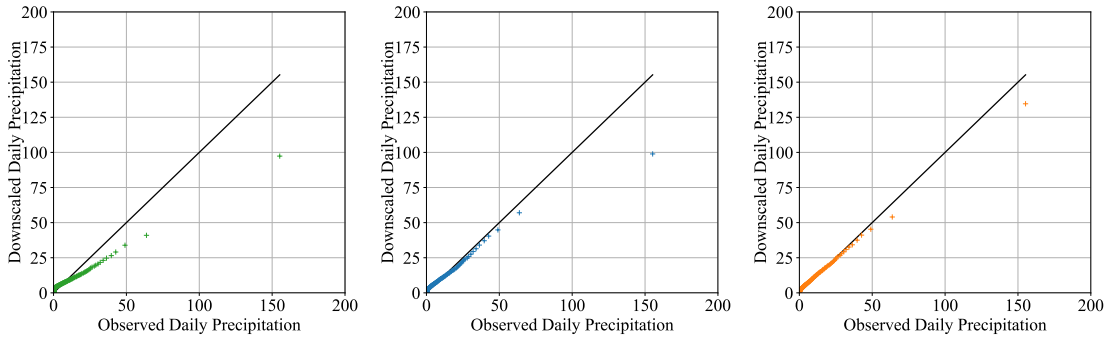

(a) (b) (c)

Figure 3.6: Historical Quantile-Quantile plots of daily precipitation from: (a) observed data vs. MIROC-GDDP downscaled data; (b) observed data vs. MIROC-LOCA downscaled data; and (c) observed data vs. MIROC-MACA downscaled data

3.4.3.2 Serial Dependency

Figure 3.7 and Figure 3.8 show the copulas obtained from CCSM4 model and MIROC model, respectively. The results from models (in green, blue and orange curves) are compared with results from observed historical data (in black curves). From these figures, it can be found that copulas obtained from downscaled GCMs are significantly different from the ones obtained from the observation. For MIROC-

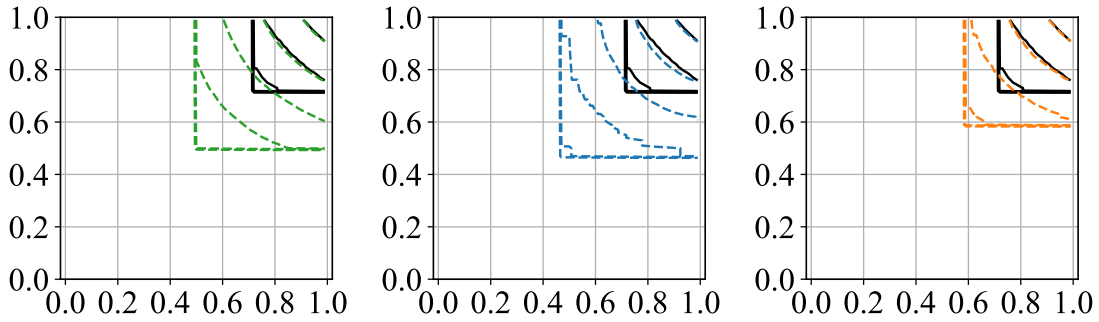

Figure 3.7: Historical copulas extracted from: (a) Observed data vs. CCSM4-GDDP downscaled data; (b) Observed data vs. CCSM4-LOCA downscaled data; and (c) Observed data vs. CCSM4-MACA downscaled data

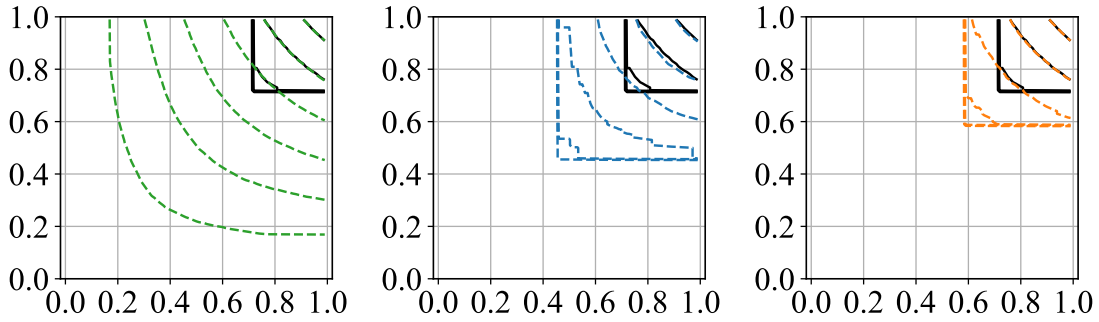

Figure 3.8: Historical copulas extracted from: (a) Observed data vs. MIROC-GDDP downscaled data; (b) Observed data vs. MIROC-LOCA downscaled data; and (c) Observed data vs. MIROC-MACA downscaled data

LOCA, even the shape is deformed, which may partially explain why this combination leads to worse results than others. Another observation is that CCSM4-GDDP is closer to the observation than CCSM4-LOCA model, but MIROC-GDDP is worse than MIROC-LOCA model. This also indicates that different downscaling methods can yield higher accuracy for a specific GCM. As for similarities, it can be observed that the copula values are close when values are higher than 0.75, which corresponds to a small region in the whole copula.

In summary, most copulas obtained from downscaled GCM results differ sig-

nificantly from the one obtained from observed data. The inaccuracy of copula is the major contributor to the inaccuracy of the extreme precipitation results from these models.

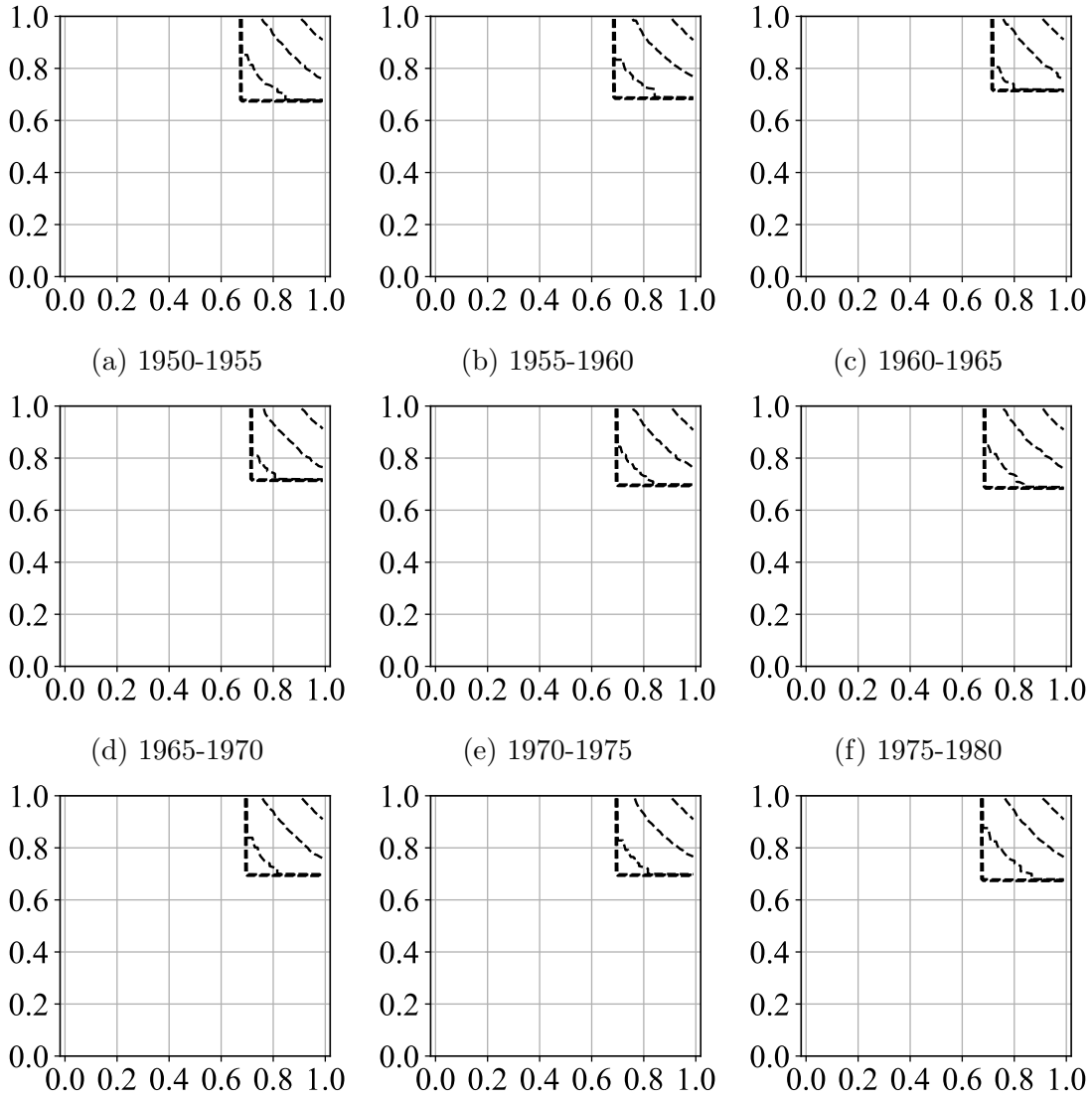

(a) 1950-1955 (b) 1955-1960 (c) 1960-1965

(d) 1965-1970 (e) 1970-1975 (f) 1975-1980

(g) 1980-1985 (h) 1985-1990 (i) 1990-1995

Figure 3.9: Historical copulas extracted from different periods of observed data.

3.4.4 Improvement of Downscaling Results via Copula

3.4.4.1 Validation on Stationarity of Historical Copulas

As mentioned in the previous section, it is crucial to validate the assumption if the historical copula stays stationary over a long period of time. Figure 3.9 shows historical copulas from 1950 for each 5-year period obtained from observed data. Although the amount of precipitation changes, this figure shows that the day-to-day serial dependency stays mostly the same for the past 45 years from 1950 to 1995.

To further explore the amount of change in copulas quantitatively, the relative difference between copula in each 5-year period and the overall 45-year copula is also computed. The computation is based on NMAE and NRMSE as applied previously. Table 3.5 presents the results. It can be observed that the variation of copulas in different period is small. Therefore, it is appropriate to assume that the day-to-day serial dependency is time-invariant with the projection timeframe.

Start Year	1950	1955	1960	1965	1970	1975	1980	1985	1990
NMAE	0.008	0.004	0.007	0.007	0.0004	0.004	0.0003	0.0003	0.008
NRMSE	0.066	0.047	0.066	0.066	0.002	0.046	0.001	0.001	0.065

Table 3.5: Normalized mean absolute error (NMAE) and normalized root-mean-square error (NMRSE) between copulas from every five years and the overall copula

3.4.4.2 Assessment of the Improved Analysis

Similar to the previous section, the same assessment is also repeated on downscaled GCMs with improved serial dependency. In addition, the NMAE and NRMSE are

computed in the same manner over the same historic period. The improvement ratio is further computed as the improvement in terms of NMAE and NRMSE. In detail, denoting $NMAE_1$, $NRMSE_1$ as the relative error before improvement and $NMAE_2$, $NRMSE_2$ as the relative error computed after applying the improvements mentioned, improvement ratio is defined to be the ratio of these values respectively. For example, if a downscaled GCM has NMAE decreased from $NMAE_1 = 0.6$ to $NMAE_2 = 0.3$, and NRMSE decreased from 1.2 to 0.8, the improvement ratio of NMAE is computed as $\frac{0.6}{0.3} = 2$, and the improvement ratio of NRMSE is computed as $\frac{1.2}{0.8} = 1.5$.

	Improvement ratio of NMAE (NRMSE) for all indices					
Methods	Max	M2d	R20mm	CWD	LDP0.5	LDP0.25
GDDP	8.13 (7.09)	1.44 (1.39)	2.06 (2.02)	2.7 (2.55)	3.99 (3.64)	7.94 (6.88)
LOCA	2.66 (2.53)	2.3 (2.11)	2.57 (2.41)	2.52 (2.32)	2.36 (2.3)	2.34 (2.18)
MACA	1.72 (1.75)	1.66 (1.58)	1.62 (1.57)	1.62 (1.57)	1.57 (1.57)	1.6 (1.6)

Table 3.6: Improvement ratio of the improved downscaling results in terms of two error metrics: Normalized mean absolute error (NMAE) and normalized root-mean-square error (NRMSE)

In Table 3.6, the improvement ratio for downscaled CCSM4 models, which represent the best results after improvement. From the table, it can be concluded that, by incorporating historical serial-dependency, the accuracy of different models are increased ranging from 1.2× to 8×, depending on the combination of GCMs and downscaling methods. For more than half of the model, at least 2× improvement can be observed. This verifies the effectiveness of the method proposed. Table 3.7 and Table 3.8 shows the same error metrics for improved downscaling results after applying the improvement described in this work. From the tables, one can see

that for Max, M2d, and R20mm, the error stays roughly the same compared to the results before the improvement. However, huge improvement can be found for CWD, LDP0.5, and LDP0.25, where the events are more related to the dependency.

GCMs	Downscaling Methods	Max	M2d	R20mm
CanESM2	GDDP	0.65 (0.78)	0.65 (0.79)	0.92 (0.98)
	LOCA	0.44 (0.62)	0.47 (0.64)	0.66 (0.74)
	MACA	0.37 (0.54)	0.38 (0.56)	0.40 (0.50)
CCSM4	GDDP	0.37 (0.51)	0.39 (0.52)	0.52 (0.62)
	LOCA	0.45 (0.60)	0.46 (0.62)	0.66 (0.74)
	MACA	0.39 (0.55)	0.39 (0.55)	0.40 (0.52)
CNRM	GDDP	0.42 (0.57)	0.43 (0.58)	0.59 (0.65)
	LOCA	0.43 (0.59)	0.44 (0.61)	0.65 (0.72)
	MACA	0.36 (0.51)	0.36 (0.50)	0.40 (0.49)
CSIRO	GDDP	0.43 (0.59)	0.43 (0.59)	0.70 (0.77)
	LOCA	0.46 (0.59)	0.46 (0.63)	0.64 (0.71)
	MACA	0.38 (0.53)	0.39 (0.55)	0.40 (0.48)
GFDL	GDDP	0.55 (0.70)	0.55 (0.72)	0.82 (0.88)
	LOCA	0.45 (0.61)	0.46 (0.64)	0.64 (0.72)
	MACA	0.39 (0.53)	0.41 (0.56)	0.4 (0.51)
MIROC	GDDP	0.64 (0.77)	0.65 (0.79)	0.91 (0.97)
	LOCA	0.44 (0.61)	0.46 (0.63)	0.64 (0.72)
	MACA	0.4 (0.56)	0.39 (0.55)	0.42 (0.53)

Table 3.7: Performance of 18 different downscaled GCMs in the context of extreme precipitation using two error metrics after improvement: Normalized mean absolute error (NMAE) and normalized root-mean-square error (NRMSE)

3.5 Discussions and Conclusions

Global warming has led to an increase of extreme precipitation in recent years, which increases the risk of damage in various form. This chapter presents a complete study of extreme precipitation analysis and future projection based on downscaled

GCMs	Downscaling Methods	CWD	LDP0.5	LDP0.25
CanESM2	GDDP	0.19 (0.24)	0.15 (0.18)	0.16 (0.22)
	LOCA	0.18 (0.23)	0.13 (0.16)	0.17 (0.23)
	MACA	0.18 (0.25)	0.17 (0.21)	0.19 (0.25)
CCSM4	GDDP	0.21 (0.26)	0.28 (0.32)	0.29 (0.34)
	LOCA	0.18 (0.23)	0.13 (0.16)	0.16 (0.22)
	MACA	0.20 (0.25)	0.18 (0.23)	0.22 (0.27)
CNRM	GDDP	0.20 (0.24)	0.18 (0.23)	0.23 (0.28)
	LOCA	0.18 (0.23)	0.13 (0.17)	0.18 (0.22)
	MACA	0.18 (0.24)	0.18 (0.22)	0.21 (0.27)
CSIRO	GDDP	0.18 (0.23)	0.21 (0.25)	0.24 (0.28)
	LOCA	0.18 (0.22)	0.14 (0.18)	0.18 (0.23)
	MACA	0.18 (0.25)	0.16 (0.20)	0.2 (0.26)
GFDL	GDDP	0.18 (0.24)	0.17 (0.21)	0.22 (0.26)
	LOCA	0.19 (0.24)	0.15 (0.18)	0.19 (0.24)
	MACA	0.18 (0.24)	0.17 (0.21)	0.22 (0.27)
MIROC	GDDP	0.17 (0.22)	0.13 (0.17)	0.16 (0.21)
	LOCA	0.17 (0.22)	0.11 (0.15)	0.17 (0.21)
	MACA	0.18 (0.24)	0.17 (0.22)	0.22 (0.27)

Table 3.8: Performance of 18 different downscaled GCMs in the context of extreme precipitation using two error metrics after improvement: Normalized mean absolute error (NMAE) and normalized root-mean-square error (NRMSE)

Global Climate Models. It first assesses the accuracy of existing downscaled Global Climate Models when used for extreme precipitation analysis. The results show that existing models are not accurate for several extreme precipitation indices considered. In order to explore ways to improve analysis accuracy, this work uses copulas to separately study marginal distribution and day-to-day serial dependency. It shows that the day-to-day serial dependency, represented as a copula, is the major cause of inaccuracy.

Based on this, this work proposes a method to improve the accuracy of down-

scaled GCMs when used for extreme precipitation projection. The main observation is that although precipitation changes over years, the serial dependency between days stays stationary. The results show that using copulas is an effective way to incorporate serial dependency into downscaled Global Climate Models.

Chapter 4: Extreme Precipitation Application: Machine Learning and Intensity-Duration-Frequency Curves

4.1 Overview

Intensity-Duration-Frequency Curves are crucial in infrastructure design, but existing works of IDF curve projection are not capable of producing reliable IDF curves especially for durations shorter than 12 hours. This chapter proposed a framework to fill this gap with two important features: 1) it integrates the projection procedures using machine learning to reduce the error; 2) it performs temporal downscaling on the data to generate IDF curves for short duration. The results are validated across two thousand stations across the US. The content of this chapter is based on a paper published to Geosciences: Special Issue on Climate Prediction of Extreme Events [117].

A method based on machine learning is proposed, which enables reliable IDF curve projection with resolution as small as 30 minutes. See Appendix D for more details on Machine Learning. The key observation is to adopt the idea of geographical downscaling to temporal downscaling of the data. To ensure high accuracy, machine learning is used to automate and integrate the process, producing future

IDF curves directly. In the next section, a technical discussion of the method is presented. Then, this method is applied to study the IDF curves of four different cities in the US. The trend of IDF curves is analyzed and summarized.

4.2 Background

4.2.1 Intensity–Duration–Frequency Curves

As discussed in the introduction section, IDF curves are fundamental to the design of water infrastructures and drainage systems to make them resilient to extreme precipitation and flash floods. However, it is a non-trivial task to obtain IDF curves that reflect the intensity of extreme precipitation accurately. There are primarily two approaches to compute IDF curves, each with different advantages.

The first method used to produce IDF curves is to make assumptions on the precipitation distribution and then use mathematical tools to derive a formula for the IDF curves [118]. This method has become a popular way to compute IDF curves, and it is widely used in practice. Many prior works have explored what types of distribution can be used to use to get a higher accuracy when this method is applied to analyze IDF curves. One important family of distribution is the Generalized Extreme Value (GEV) distribution family. For example, Tfwala et al. [119] assumed that the precipitation distribution for each time interval follows the GEV distribution. Then, they computed the IDF curve based on the assumed distribution for each intensity and duration. Bougadis and Adamowski [120] studied scale invariances for disaggregating daily rainfall to hourly rainfall based on the scaling

of GEV. Blanchet et al. [121] developed a GEV simple-scaling model to correct extremes of aggregated hourly rainfall. The use of GEV assumes that the precipitation levels over consecutive time intervals are independent of each other. This can be guaranteed by, for example, using a subsampling method [122, 123].

The second method is based on empirical analysis. The empirical analysis of an IDF curve directly makes assumptions about the formulas of IDF curves, which are summarized from historical observations. These formulas usually come with two or more degrees of freedom. Then, empirical results are gathered from historical results to fit the above formulas and determine the parameters in the formulas. There are many IDF empirical formulas, and some of the popular ones are listed below:

$$I(t) = \frac{a}{(t+c)^n} \tag{4.1}$$

$$I(t) = \frac{a}{t^n + c} \tag{4.2}$$

$$I(t,p) = \frac{ap^m}{(t+c)^n}. \tag{4.3}$$

In the above equations, I represents the intensity of the precipitation, t represents the duration, and p is the return period. Other parameters must be decided and can vary depending on the time and location. Equation 4.1 was initially proposed

by Sherman [124] when studying precipitation in the Boston area. Equation 4.2 was studied by Chow et al. [125]. Note that these two equations do not have a return period as the input and thus can be used for a specific return period only. If more than one of the IDF curves is needed, then multiple fitting using their respective historical data is required.

The most widely used formula was initially proposed by Bernard [126] and is shown in Equation 4.3. Different from Equations 4.1 and 4.2, it also incorporates the return period and thus, needs one fitting to model all return periods. This equation is based on the fact that the tail distribution of the intensity follows the power law. When it comes to short durations, Haerter et al.[127] studied when such assumption is true. They concluded that power law holds when the duration is longer than 30 minutes. This study mainly focuses on durations longer than 30 minutes when Equation 4.3 is reliable. If using this equation for durations much shorter than 30 minutes, a higher error is more likely to appear. The empirical approach has attracted much attention in the computing of IDF curves. For example, Singh and Zhang [128] explored the use of Equation 4.3 for empirical analysis in the context of urban drainage design. Jain and Pandey [129] reviewed numerous empirical methods, including both Equation 4.1 and Equation 4.3; they also studied a copula-based method for IDF curve formation. Dar et al. [130] studied the application of Equation 4.3 with fitted parameters to study various areas in India.

4.2.2 Spatial Downscaling

Projecting future climate is a difficult task because it depends on the human activity level, which is highly unpredictable. Additionally, the global climate system is complicated, and it is difficult to model all variables in the system. Therefore, future projection of climate requires a significant amount of effort, which has led to the formation of the Coupled Model Intercomparison Project (CMIP), where numerous GCMs have been proposed. These models usually make a set of global simulations that are openly available to download for each Representative Concentration Pathway (RCP), and these simulations are one of the most reliable sources for the future projection of climate. One major drawback of these GCM simulations is that they are usually available on a daily basis and at a coarse spatial resolution, which limits their usage to the study of local areas. Downscaling is a commonly used procedure to incorporate localized spatial influence to the GCM simulation to obtain future projections with high spatial resolution. One popular approach is dynamic downscaling, where a simulation of high resolution is performed on the regions of interest to extrapolate details from global GCMs [99, 100, 101]. It is able to incorporate physical principles into the analysis easily, but it is computationally intensive and sensitive to bias.

Statistical downscaling is another popular approach for downscaling, which views the downscaling process from a statistical perspective to find the relational properties between global climate and local climate. Most existing statistical downscaling methods adopt an ad-hoc way to find the downscaling relationship. Existing

statistical downscaling methods all follow a similar paradigm, as summarized below:

1. Find a parameterized model to abstract the downscaling relationship between the global climate and local climate. The model is usually parameterized by a set of values.

2. Use historical data to fit the model and find the parameters for the model. These parameters are assumed not to change over time. Perform bias correction to the results using methods like the Constructed Analogue method [103].

3. Compute the local climate data using the model with fitted parameters and the future global climate.

This paradigm has been used by many popular downscaling works, including the Bias Corrected Constructed Analogue (BCCA) [103], the Multivariate Adaptive Constructed Analogs (MACA) [51], LOCA [50, 131], and NEX-GDDP [49]. They are mainly different in the way of bias correction. This study uses downscaled GCM simulation results from the NEX-GDDP downscaling project to improve the geographic resolution. Other downscaling methods and GCM simulations can be used by the proposed method in a similar way.

4.3 Methodology

4.3.1 Overview

The main goal of this study was to compute precipitation intensity over a short duration using only daily downscaled GCM simulation data by means of temporal

downscaling. Because the complexity of temporal downscaling can be high and that temporal data is not as abundant as spatial data, some extra procedures are required. First, instead of obtaining downscaled hourly precipitation data for the duration of study, the downscaling is designed such that it can directly output the intensity of the precipitation for different lengths of time. This simplification hugely eliminates unnecessary steps. To compute such a mapping from projected daily data to the intensity of short durations, machine learning algorithms are adopted that can perform non-linear learning efficiently. A summary of the comparison among machine learning, spatial downscaling, and the proposed temporal downscaling is provided in Table 4.1.

Method	**Known property**	**Known target**	**Projection property**	**Projection target**
Machine Learning	Train data features	Train data label	Test data features	Test data label
Statistical downscaling	Historical GCM data	Historical downscaled data	Future GCM GCM data	downscaled GCM data
Temporal downscaling	Historical downscaled GCM daily data	Historical 15-minute intensity	Future downscaled GCM daily data	Future 15-minute intensity

Table 4.1: Comparison of machine learning, statistical downscaling, and the proposed temporal downscaling.

All three procedures follow a similar sequence of steps, as follows:

1. Obtain some number of entries with both properties and targets. Taking these entries as the input, compute a description of the relationship between the entry properties and the targets.

2. Make the assumption that the relationship between properties and targets holds for the projected entries.

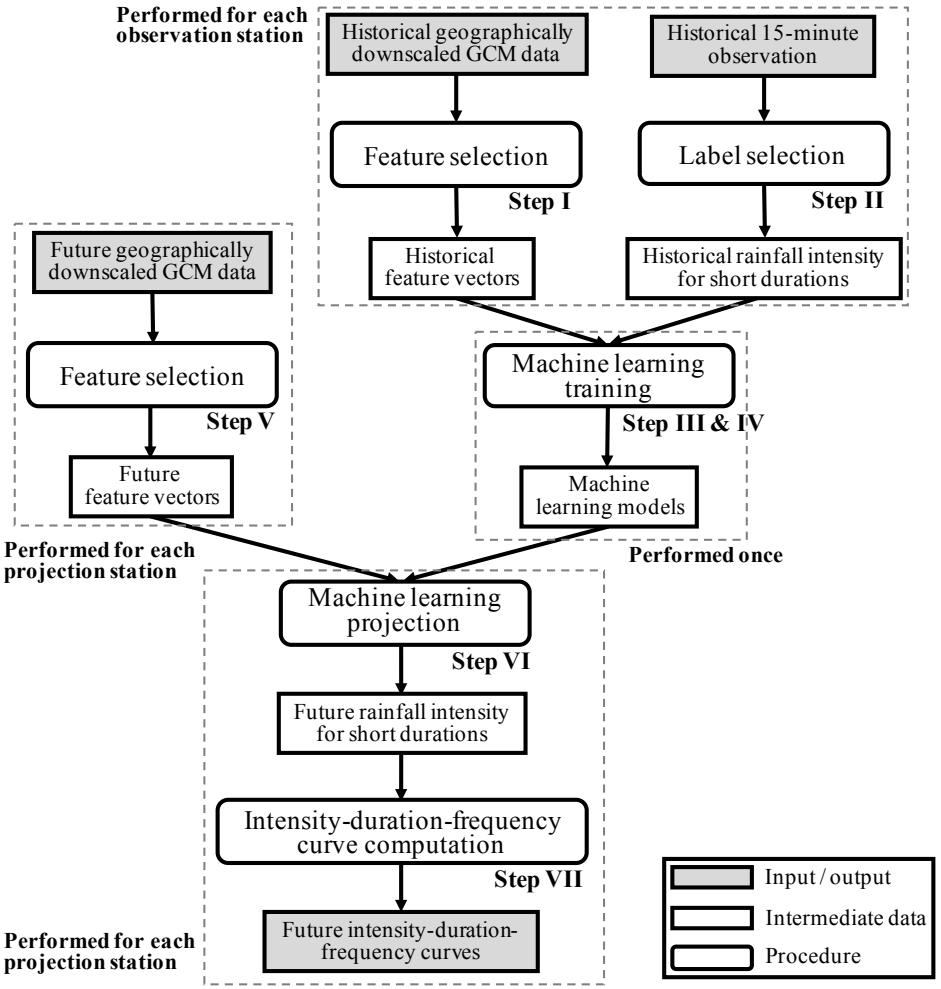

Figure 4.1: Overview of the proposed method

3. Use the above relationship as well as the properties for the projected entries, and then compute the target value of the projected entries.

The method discussed in the following text also works for the three steps above but in the context of short-duration intensity projection.

4.3.2 Detailed Steps

In the following, all steps of the proposed method are discussed in detail. In Figure 4.1, an overview of the procedure is illustrated.

4.3.2.1 Step I: Historical Feature Selection

The first step is to select features for the use of machine learning training. Every station represents a different data entry, and a set of features is extracted. The source of data used to extract the feature is downscaled GCM simulation data, which provides better a geographic resolution. In principle, it is possible to use the downscaled GCM data directly as features; however, in this case, the dimensions of the feature vector were too high for any machine learning algorithm to perform well. To reduce the dimensions of the features without affecting the learning accuracy, a set of features related to extreme precipitation and spatial information was selected. First, the following seven features were computed across all years for each station.

1. One-day and two-day precipitation intensities of the events with return periods of 2, 5, and 10 years.

2. Average daily precipitation.

The precipitation intensities are highly related to the short-duration intensities, because of the power law. The average precipitation provides a baseline on the average level of the precipitation.

Then, the average of the following 29 features across all years was computed for each station.

3. Number of rainy days.

4. Top 20 heaviest daily precipitation amounts in descending order.

5. Number of days with a daily precipitation of more than 5, 10, 15, 20, 30, 40, 50, and 60 mm.

The above three sets of features further describe some extra properties of the distribution of extreme precipitation. For example, the top heaviest daily precipitation provides more insights on how extreme precipitation tail distribution looks. The number of days with precipitation more than certain levels sketches the general trend of daily precipitation distribution.

Finally, the following 4 geographic features were extracted for each station.

6. Altitude of the location. This was obtained from the National Oceanic and Atmospheric Administration Climate Data Online (NOAA CDO).

7. The coordinates of the location, that is, latitude and longitude.

8. Climate division of the location. Since there are 344 climate divisions for the contiguous US [92], this feature had a value from 1 to 344. The use of climate division is to reenforce the geographic proximity between stations.

All features above provide insights on relative distance between different stations. The main intuition is that stations with geographic proximity should share similar intensity curves. Due to this reason, stations from different regions of the US can be distinguished by the model as their climate divisions are different. The above features are popular in the analysis of extreme precipitation, including the US Climate Extremes Index (CEI) and the Expert Team on Climate Change Detection and Indices (ETCCDI). They result in a feature vector with 40 dimensions for each

station. Note that due to the use of machine learning, it will be fairly easy to add more features in future research. This procedure needs to be performed for both historical observation stations as well as the stations used for future projections.

4.3.2.2 Step II: Label Selection

This study uses the IDF formula based on Equation 4.3, where IDF curves for all durations can be expressed as a single equation: for a given duration t and return period p, the intensity $I(t, p)$ is

$$I(t, p) = \frac{ap^m}{(t + c)^n}.$$

For most regression models, the output label is a scalar number, but Equation 4.3 has 4 parameters to be determined. To be able to determine all parameters, the proposed method selects four different points on the IDF curve as the label (Y). In the proposed method, the four selected points are (1) return period 2 years, duration 30 minutes, (2) return period 2 years, duration 120 minutes, (3) return period 5 years, duration 30 minutes, and (4) return period 5 years, duration 120 minutes. The precipitation intensity for these four points needs to be extracted from the training data. It is done by calculating the precipitation intensity of the corresponding events from the historical data directly.

Note that choosing any 4 or more points can be used to fit Equation 4.3. However, if points are selected to be separated as much as possible then the resulting curves are more robust to potential noise in the data. The above four points are

selected to be separated at the same time still located in short durations, which is the focus on this study.

Another potential method for selecting ML labels is to select parameters in Equation 4.3 directly, namely the values of a, c, m, n. In this potential method, all four parameters would be optimized by independent ML models. However, this can easily lead to local optimum parameter values that are far from being globally accurate. Therefore, this method is not selected, and the method based on the intensities of four selected points are used instead.

4.3.2.3 Step III: Model Selection

This step is used to select the ML model to learn the mapping from features to labels. Due to the nature of the projection, the machine learning algorithm should be able to work with continuous values, which means a regression algorithm is desired. The most powerful repression algorithms in machine learning are the Deep Neural Network (DNN) and the Gradient Boosting Tree (GBT) (see Appendix D). However, the DNN usually requires a large amount of data because all layers of the neural network need to be fitted. Given these considerations GBT is used as the main regression algorithm in this study.

4.3.2.4 Step IV: Future Feature Selection

This step is similar to Step I except that the feature selection is performed on future downscaled GCM data instead of the historical observation data.

4.3.2.5 Step V: Model Training

For each observation station, the features and label values are collected and used to train four models selected in previous steps. Each model can be used for projecting one data point on the future IDF curve.

4.3.2.6 Step VI: Machine-Learning Projection

To perform ML projection using GBT, three ML hyperparameters need to be decided: (1) the number of trees, which specifies the number of decision trees in the model; (2) the learning rate, which specifies the amount of contribution from each tree; and (3) the maximum depth, which specifies the maximum possible depth allowed in each decision tree. These hyperparameters can be determined by grid search with cross-validation, which is a common way for hyperparameter optimization and is supported in many ML software packages. After hyperparameters are decided, the model parameters can be decided as in the previous step. Note that due to the use of hyperparameter optimization, the validation is not completely independent to the data. There are numerous ways for validation to be conducted, which have been discussed in prior works in the context of hydrologic applications [132]. This work uses k-fold cross validation (see detailed discussion in Section 4.3.3). For each combination of model parameters, the validation is applied to find the best model parameters. After the model parameters have been selected and trained, projections are conducted on them. As a result, four data points on the projected IDF curves are obtained.

4.3.2.7 Step VII: IDF Curve Reconstruction

The last step is to use curve fitting to compute the IDF curves based on the four data points obtained above. The fitting algorithm used in this work is the expectation-maximization (EM) method with bounded conditions.

After step VI and the curve fitting as mentioned above, the parameters in Equation 4.3 are determined. Now the precipitation intensity for other combinations of return periods and durations can be computed from the equation directly. This study assumes that all combinations of return periods and durations follow this equation, which may not always be true. This assumption is validated in the next section before it is applied in the analysis.

4.3.3 Validation

4.3.3.1 k-fold Cross Validation

A k-fold cross-validation method is applied, since it is widely used and has extensive software support. The detailed steps are as follows:

1. Collect data from n stations. For a station, the data contains the downscaled GCM simulations of daily precipitation data and locally observed precipitation data with better resolution.

2. Partition n stations of data into k disjoint and equal-sized sets, namely $S_1, ..., S_k$. Repeat the following step (step 3) k times.

3. In the i-th repetition, use the i-th dataset as the test data (namely S_i), and the

remaining data are used as training data (namely $\{S_j\}_{j \neq i}$). Use the training data to train a machine learning model as described in the previous section and apply it to compute an IDF curve for stations in S_i. Calculate the error based on the local precipitation testing data.

4. Find the average of all errors in all k iterations above.

4.3.3.2 Validation of IDF Curves

Validation of the fitted IDF curves is performed by comparing the fitted precipitation intensity against the reference precipitation intensity provided from NOAA Atlas 14 [133], which provides the precipitation intensity for almost all states in the US.

The normalized root mean square error (NRMSE) metric and normalized mean absolute error (NMAE) are used, both of which measure the goodness-of-fit between the intensity from Atlas and the fitted ones. Similar metrics have been used to measure accuracy in prior works. For example, Chai et al. [110] compared RMSE and MAE when used for precipitation data and argued that both should be used when reporting errors. However, RMSE and MAE tend to be biased on data points with higher values. To avoid this bias, this study uses these metrics with normalization where the relative differences are computed.

The definition of NRMSE is as follows: suppose $O_{i,p}$ is the intensity of precipitation with the time interval i and return period p in the observation; suppose $E_{i,p}$ is the same value computed from the analysis. For $I = \{0.5\ hours, 1\ hours, 2\ hours\}$

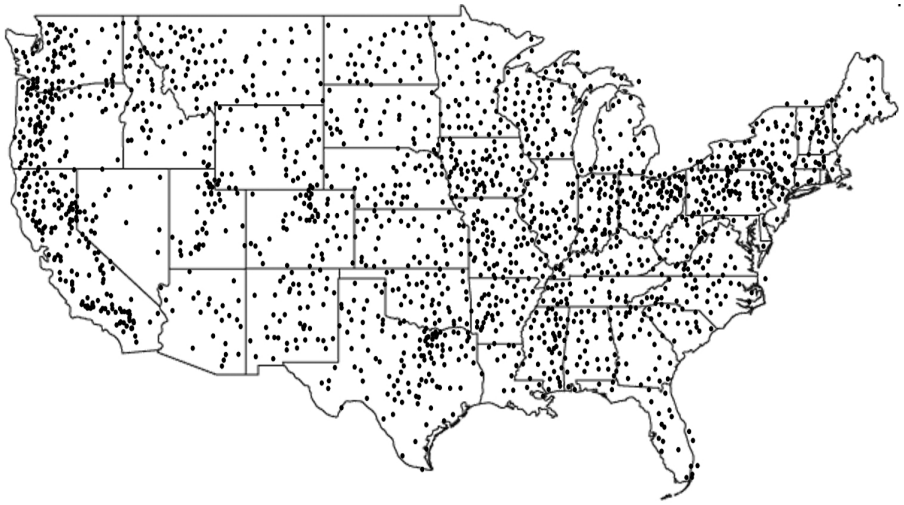

Figure 4.2: Geographic distribution of all observation stations used to train the gradient boosting tree model. All data were obtained from the National Oceanic and Atmospheric Administration Climate Data Online (NOAA CDO) [1].

and $P = \{2\ years, 5\ years, 10\ years, 50\ years\}$,

$$\text{NRMSE} = \sqrt{\frac{1}{|I| \times |P|} \sum_{i \in I, p \in P} \left(\frac{O_{i,p} - E_{i,p}}{O_{i,p}} \right)^2}. \tag{4.4}$$

The definition of NMAE is similar and can be computed as

$$\text{NMAE} = \frac{1}{|I| \times |P|} \sum_{i \in I, p \in P} \left| \frac{O_{i,p} - E_{i,p}}{O_{i,p}} \right|. \tag{4.5}$$

4.4 Analysis and Results

4.4.1 Data and Model Selection

Observation data were obtained from the data portal at the National Oceanic and Atmospheric Administration Climate Data Online (NOAA CDO) [1]. They provide historical year-round observations of data from 1970 to 2014 with a timescale of 15

Station ID	Name	State	Latitude	Longitude
COOP:043093	Florence Lake	California	37.27389	-118.97333
COOP:096879	Pearson	Georgia	31.2928	-82.8422
COOP:177325	Rumford	Maine	44.53083	-70.53722
COOP:234825	Lebanon	Missouri	37.68502	-92.69388
COOP:410569	Bay City	Texas	28.9798	-95.9749
COOP:253185	Genoa	Nebraska	41.4513	-97.7644
COOP:024586	Keams Canyon	Arizona	35.8109	-110.1932
COOP:447338	Rocky Mount	Virginia	36.9769	-79.8961

Table 4.2: Information about the eight representative stations

minutes. Among all observation stations, only those with more than 25 years of observation were selected. The spatial distribution of all stations selected is shown in Figure 4.2. In total, 1936 stations were selected. In this work, the study of IDF curve is performed on stations across the US so that there are enough data to train the ML model with high accuracy. The proposed method is applicable to a local region if enough data can be gathered to train a reliable model.

Reference precipitation intensity data used for validation were obtained from NOAA Atlas 14 project [133], where precipitation intensity data were available from all states except Washington, Oregon, Montana, Wyoming, and Idaho. These reference precipitation intensities were estimated by NOAA and were consistent with the actual precipitation intensity. More descriptions of the dataset can be found in Appendix E.

The downscaled GCM simulation data were based on Community Climate System Model 4 (CCSM4) with the NEX-GDDP downscaling method. The RCP 8.5 trajectory was extracted. The timescale of data was on a daily basis. The historical data were collected from 1970 to 2014, and the future period was from

2040 to 2099. The CCSM4 was developed by the National Center for Atmospheric Research (NCAR) in the USA. It consists of four different models, each simulating one component on the Earth's atmosphere, ocean, land surface, and sea-ice; it also includes one central coupler component. Note that the downscaled GCM simulation results were used instead of the GCM results so that the obtained results had a better spatial resolution. All downscaling data can be obtained from NASA website [134]. Since this study mainly focused on the methodology, only one downscaled GCM result was used. Note that model-to-model variation can be high and can potential influence the projection results.

The GBT models were trained based on data from 1936 stations. Eight representative stations were selected to show the projection results. They were selected to be spatially distributed across the US and have different IDF curve shapes. Details of the stations are summarized in Table 4.2.

4.4.2 Validation and Historical IDF curves

Figure 4.3 shows the historical IDF curves for all eight representative stations. There are three sets of data shown in each figure:

1. The ∘-shape data points represent precipitation intensity extracted from the historical data from NOAA CDO, with intensities of 30, 60, 90, and 120 minutes and return periods of 2 and 5 years.

2. The solid lines are IDF curves fitted based on the above observed data using Equation 4.3. This equation was used for all return periods, and four IDF

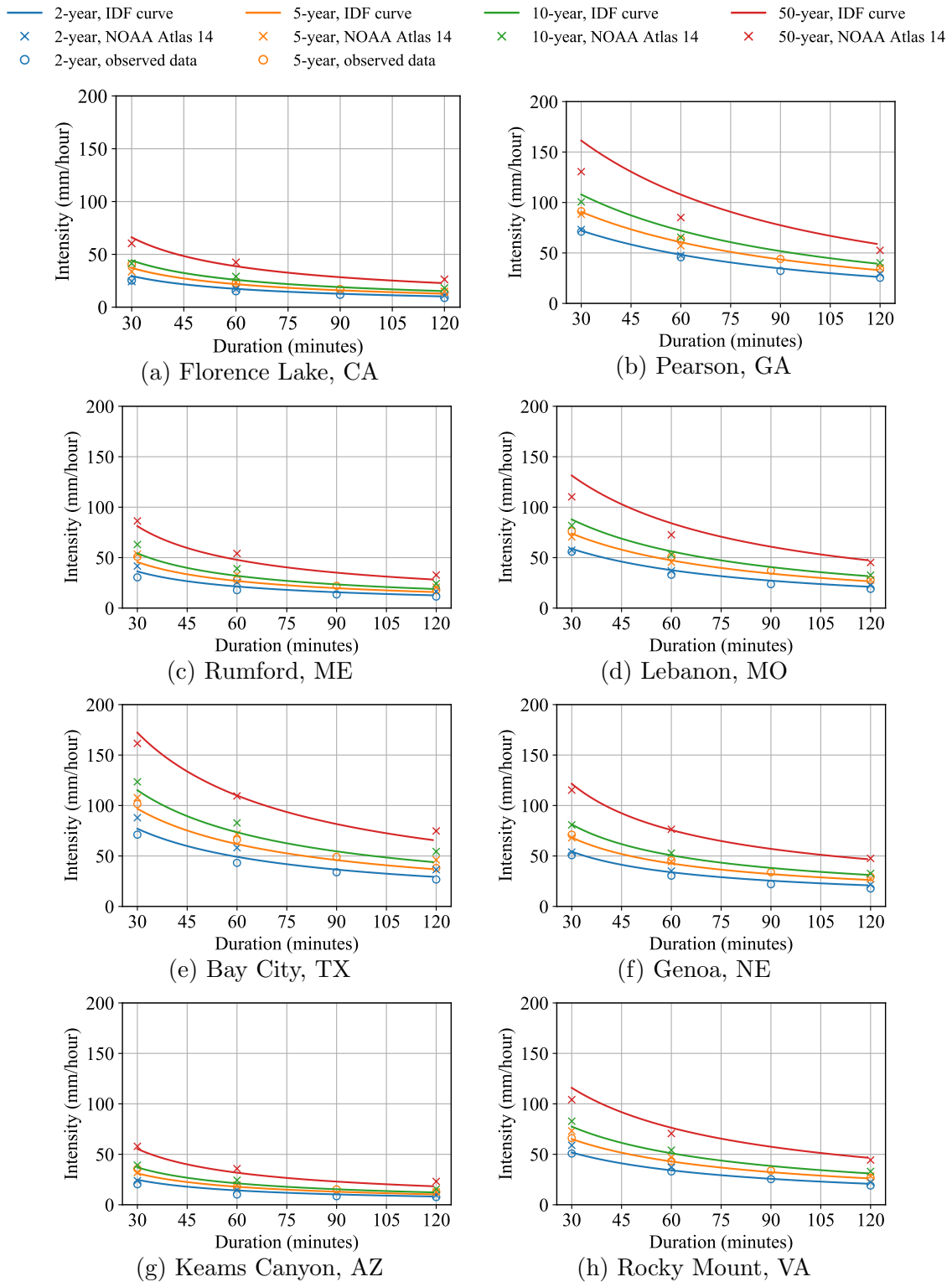

Figure 4.3: Historical Intensity–Duration–Frequency (IDF) curves. "∘" are observed intensities; "×" are Atlas 14 intensities; All solid lines were fitted using the observation intensity (in ∘) and plotted for high return periods.

curves were plotted for return periods of 2, 5, 10, and 50 years.

3. The $\times$-shape data points represent the precipitation intensity obtained from NOAA Atlas 14.

Since short-duration intensity is the focus of this study, duration was plotted from 30 minutes up to 120 minutes. The figure indicates that the shape of the IDF curves greatly depends on the location of the observation. Nevertheless, it is shown that the IDF curve for all figures fits well with the observed data and that the obtained IDF curves are consistent with the Atlas 14 precipitation intensity.

Each individual figure represents the historical precipitation intensity level in each region. The observation stations at Pearson, GA and Bay City, TX have the most extreme short-duration precipitation intensity, and with a 50-year return period, their 30-minute intensity could be as high as 150 mm/hr. Keams Canyon, AZ has a much lower level of precipitation intensity. Their 50-year return period 30-minute intensity is about 50 mm/hr.

To further quantitatively validate this approach, a comparison between fitted IDF curve and the IDF data from NOAA Atlas 14 was performed. A relative difference ratio was computed as follows, where positive values represent overestimates and negative values represent underestimates.

$$\text{Difference Ratio} = \frac{\text{Fitted intensity} - \text{Atlas intensity}}{\text{Atlas intensity}} \tag{4.6}$$

Table 4.3 summarizes the computed ratios for all eight stations picked in this study.

Duration (minutes)	Return Period (year)	CA	GA	ME	MO	TX	AZ	NE	VA
30	2	21%	-1%	-12%	2%	-12%	3%	0%	-12%
30	5	10%	2%	-14%	4%	-10%	-2%	0%	-10%
30	10	6%	7%	-13%	7%	-6%	-5%	0%	-6%
30	50	9%	23%	-5%	19%	6%	-4%	5%	11%
60	2	1%	1%	-16%	2%	-15%	-3%	-3%	-7%
60	5	-7%	6%	-18%	4%	-14%	-9%	-3%	-8%
60	10	-10%	10%	-18%	5%	-11%	-12%	-4%	-5%
60	50	-8%	26%	-11%	15%	0%	-11%	0%	8%
120	2	-8%	-10%	-23%	-6%	-19%	-14%	-3%	-7%
120	5	-14%	-6%	-23%	-5%	-20%	-19%	-4%	-8%
120	10	-15%	-2%	-22%	-3%	-19%	-21%	-4%	-6%
120	50	-13%	11%	-13%	4%	-12%	-21%	-2%	4%

Table 4.3: Relative difference between fitted IDF intensity and NOAA Atlas 14 intensity.

It can be observed from the table that most fitted intensity values are within 15% of the Atlas 14 intensity values. Even for cases where a higher difference is observed, they are still within the 25% of the difference. It is also observed that the difference ratios for 120-minutes duration is higher than shorter durations in general. Because the intensities for 120-minutes are much smaller than shorter durations, the resulting difference ratios becomes larger given the same error in intensity. TX and ME have the largest error where many intensities are below the Atlas 14 intensities, resulting in negative difference ratios. For these locations, the observed intensities are also much less than the Atlas 14 intensities. This is believed to be the reason that causes a larger error for these locations.

Table 4.4 shows the goodness-of-fit between the IDF curve fitted from the observations and the intensity data from NOAA Atlas 14. As discussed in Section 4.3.3, NRMSE and NMAE were used. Smaller values of NRMSE and NMAE

	CA	GA	ME	MO	TX	AZ	NE	VA
NRMSE	0.117	0.121	0.170	0.085	0.137	0.033	0.127	0.084
NMAE	0.107	0.092	0.163	0.068	0.124	0.028	0.108	0.081

Table 4.4: NRMSE and NMAE between fitted IDF intensity and the NOAA Atlas 14 intensity.

means higher accuracy. The table shows that the fitting errors are relatively small compared to the actual values of intensity. In Table 4.5, 44 stations from different states in the US are examined in a similar way with NRMSE and NMAE presented. NOAA Atlas 14 data from 5 states are not available and thus not included. AK is also not included due to lack of data. This table shows that even across a wide selection of areas, the error is relatively small with an average NRMSE and NMAE about 0.1.

4.4.3 Projection Results

Future precipitation intensity was projected following the steps described in the previous section. The projected results are shown in Figure 4.4 for years 2040 to 2069 and in Figure 4.5 for years 2070 to 2099. The historical IDF curves are also shown with dotted lines for comparison. These figures show that the precipitation intensities are projected to increase in all locations, although the amount of increase is different. In more detail, Bay City, TX, and Pearson, GA are projected to suffer from greater increases in precipitation intensity. The intensity will increase by around 50 mm/hour. The increases in Florence Lake, CA, and Keams Canyon, AZ are projected to be the smallest.

Station	Location	State	NRMSE	NMAE
010140	ALBERTA	AL	0.109	0.077
034839	MILLWOOD DAM	AR	0.122	0.11
026119	ORACLE 2 SE	AZ	0.057	0.051
048025	SAWYERS BAR RANGER STATION	CA	0.145	0.117
052790	EVERGREEN	CO	0.111	0.104
066942	ROCKVILLE	CT	0.09	0.077
076410	NEWARK UNIVERSITY FARM	DE	0.142	0.12
083538	GRACEVILLE 1 SW	FL	0.067	0.062
093312	FARGO	GA	0.133	0.117
510055	AHUIMANU LOOP	HI	0.061	0.053
130608	BELLEVUE L AND D 12	IA	0.087	0.075
114355	ILLINOIS CITY DAM 16	IL	0.064	0.06
120830	BLUFFTON 6 N	IN	0.149	0.128
146024	ONAGA 12 SSW	KS	0.049	0.04
153929	HODGENVILLE LINCOLN	KY	0.169	0.12
161411	CALHOUN RES STATION	LA	0.144	0.134
190998	BUFFUMVILLE LAKE	MA	0.182	0.174
180700	BELTSVILLE	MD	0.11	0.078
170273	AUGUSTA	ME	0.048	0.039
200662	BELLAIRE	MI	0.06	0.054
218323	TRACY	MN	0.111	0.107
230204	APPLETON CITY	MO	0.076	0.065
227276	RALEIGH 6 N	MS	0.052	0.045
311241	BURLINGTON	NC	0.126	0.118
325993	MINOT EXPERIMENT STATION	ND	0.048	0.044
250075	ALBION 7 W	NE	0.107	0.089
273182	FRANKLIN FALLS DAM	NH	0.085	0.075
281351	CAPE MAY 2 NW	NJ	0.155	0.141
292700	EAGLE NEST	NM	0.215	0.207
264698	LOVELOCK	NV	0.2	0.193
309442	WHITNEY POINT DAM	NY	0.058	0.049
332272	DOVER DAM	OH	0.103	0.097
340179	ALTUS IRIG RES STATION	OK	0.07	0.062
369367	WAYNESBURG 1 E	PA	0.136	0.126
375215	NEWPORT ROSE	RI	0.209	0.208
383468	GEORGETOWN 2 E	SC	0.158	0.146
391452	CARPENTER 4 NNE	SD	0.066	0.06
406170	MONTEREY	TN	0.157	0.129
414679	JUSTIN	TX	0.105	0.077
420086	ALTON	UT	0.14	0.123
446475	PAINTER 2 W	VA	0.108	0.1
433914	HIGHGATE FALLS	VT	0.101	0.09
473038	GENOA DAM 8	WI	0.049	0.044
463238	FREEMANSBURG 5 NE	WV	0.096	0.074
Average			0.110	0.097

Table 4.5: NRMSE and NMAE between fitted IDF intensity and the NOAA Atlas 14 intensity.

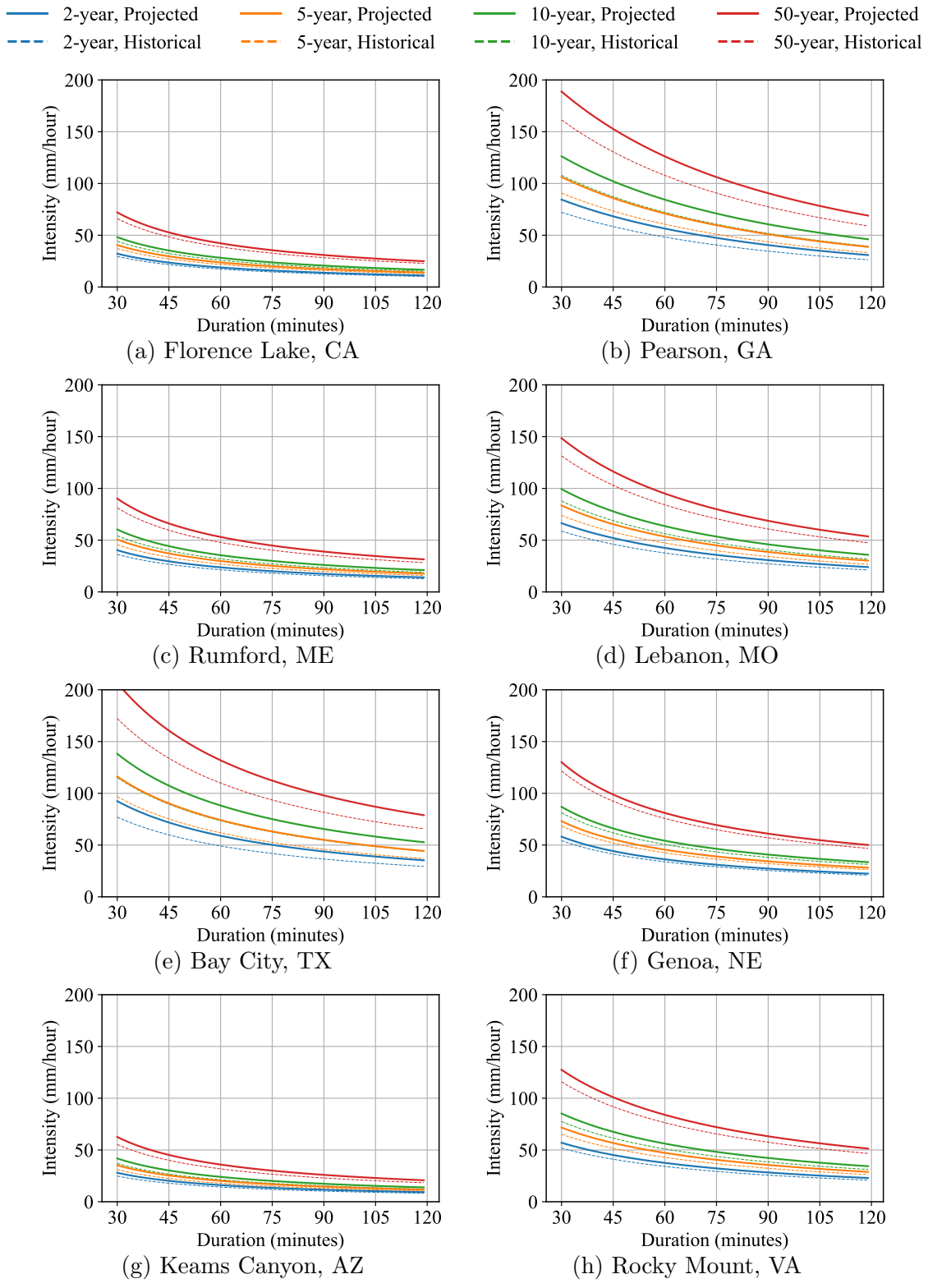

(a) Florence Lake, CA

(b) Pearson, GA

(c) Rumford, ME

(d) Lebanon, MO

(e) Bay City, TX

(f) Genoa, NE

(g) Keams Canyon, AZ

(h) Rocky Mount, VA

Figure 4.4: Projected IDF curves with a time period from 2040 to 2069. Dotted lines are for historical IDF curves; solid lines are for projected IDF curves.

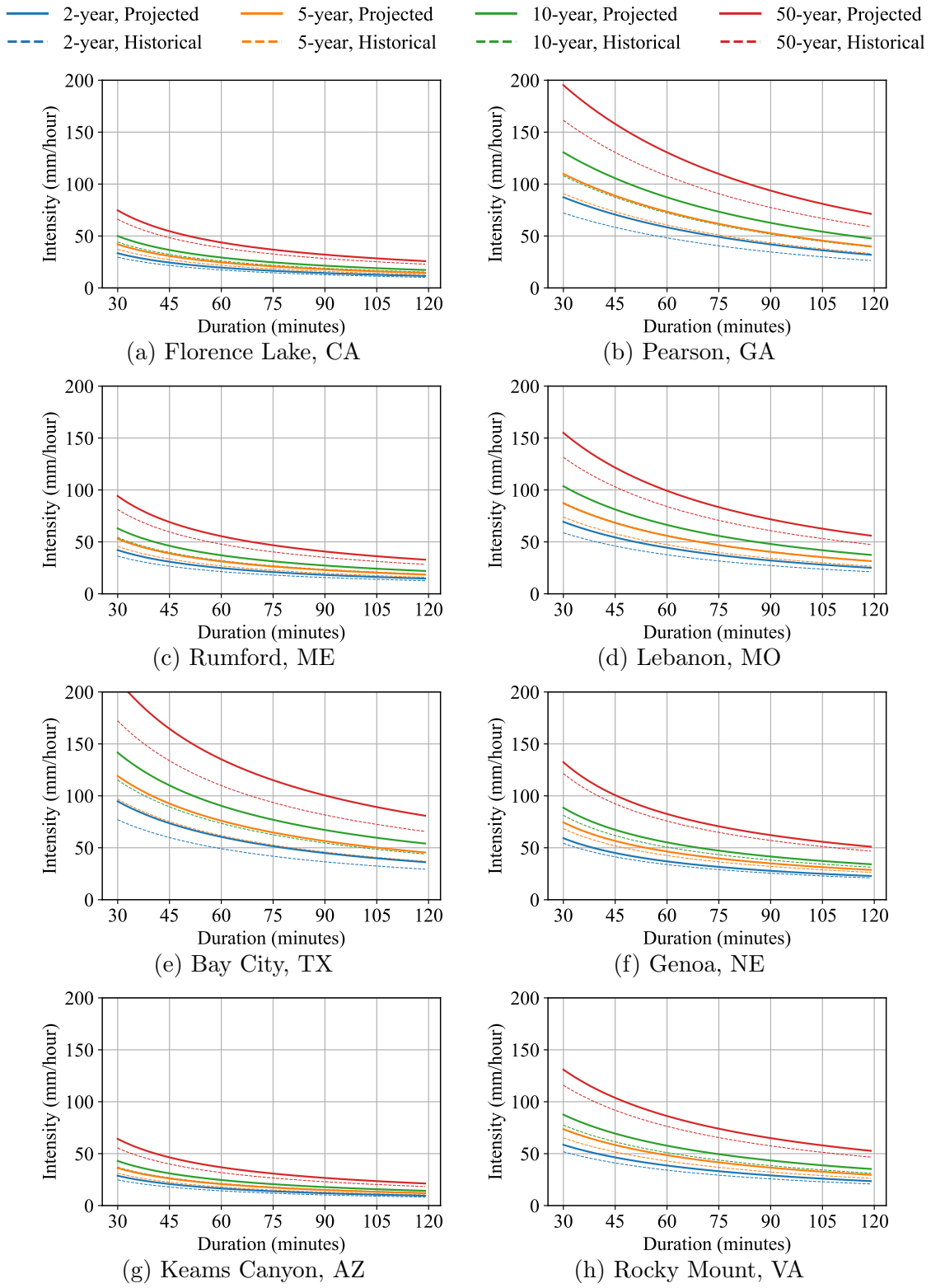

(a) Florence Lake, CA

(b) Pearson, GA

(c) Rumford, ME

(d) Lebanon, MO

(e) Bay City, TX

(f) Genoa, NE

(g) Keams Canyon, AZ

(h) Rocky Mount, VA

Figure 4.5: Projected IDF curves with a time period from 2070 to 2099. Dotted lines are for historical IDF curves; solid lines are for projected IDF curves.

The increase ratio is further calculated based on the projection, which demonstrates the relative amount of increase across short durations. These ratios are shown in Table 4.6. From the table, it is observed that the ratio of increase is higher for locations with historically higher precipitation intensity (e.g., GA, TX, MO). The highest ratio of increase is 23% for the selected representative stations. The ratio of increase in the US can be even higher than these selected stations, which is an interesting future work. It means that locations that suffers the most from the damage of extreme precipitation will witness even more extreme precipitation in the future, possibly because locations with higher intensities will be more vulnerable to climate change. The ratios are computed following the equation, as the average of all ratios at different locations on the IDF curves.

$$\text{ratio} = \frac{1}{|I| \times |P|} \times \sum_{i \in I, p \in P} \frac{Projection_{i,p}}{Historical_{i,p}} \tag{4.7}$$

where $I = \{30\,minutes, 1\,hours, 2\,hours\}$ and $P = \{2\,years, 5\,years, 10\,years, 50\,years\}$.

Location	CA	GA	ME	MO	TX	AZ	NE	VA
Ratio of Increase (2040–2069)	9%	17%	11%	13%	20%	13%	7%	10%
Ratio of Increase (2070–2099)	13%	21%	16%	18%	23%	16%	9%	13%

Table 4.6: Ratio of increase for the projected IDF curves for future periods based on downscaled GDDP GCM results using the CCSM4 downscaling method.

4.4.4 Intensity Analysis for a 500-year Return Period

Figure 4.6 shows the historical and projection results when the return period is 500 years. It can be observed that the relative increase is not as high as values for a smaller return period, but the absolute difference is higher.

4.5 Conclusion

The expected precipitation intensity of short durations significantly affects the design of drainage systems. This work proposed an alternative method to improve the projection of IDF curves for short durations. The method is based on a temporal downscaling approach, which produces information for short durations based on the information from long durations. In more detail, a machine-learning based approach is used, where daily precipitation downscaled GCM data are used as feature values, and the precipitation intensity is used as the label values. By obtaining multiple intensity points, future IDF curves are projected with different duration and return period. One caveat of this method is the use of IDF equation to derive precipitation intensity, where it is assumed that the precipitation intensity of different return periods and durations follow some mathematical equation. This should always be validated first before used.

By using this method, downscaled GCM simulation data obtained from NASA NEX-GDDP project were used for future IDF curve projection. The historical precipitation intensity was obtained from NOAA CDO 15-minute precipitation observed data. The data and IDF formula were further validated based on eight stations

across the US. By comparing the fitted precipitation intensity against the Atlas 14 intensity, high accuracy was found. The projection results show that an increase in precipitation intensity of 10% to 20% may be observed in the next few decades.

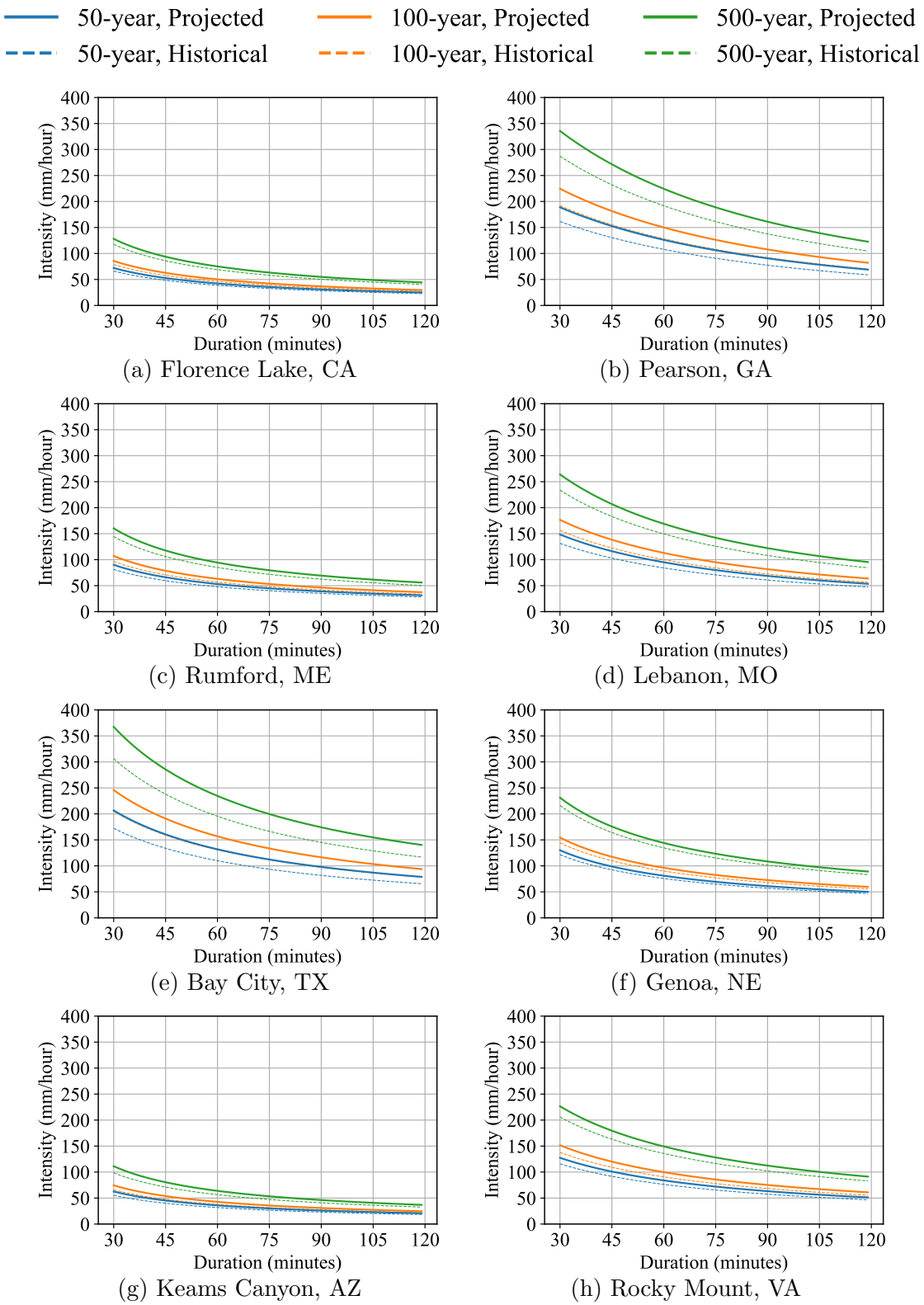

(a) Florence Lake, CA

(b) Pearson, GA

(c) Rumford, ME

(d) Lebanon, MO

(e) Bay City, TX

(f) Genoa, NE

(g) Keams Canyon, AZ

(h) Rocky Mount, VA

Figure 4.6: IDF curve for 500-year return period. Three curves are for historical, 2040 to 2069, and 2070 to 2099.

Chapter 5: Conclusions and Future Directions

5.1 Summary of Contribution

This dissertation presents a series of multi-discipline research, using state-of-the-art mathematical, statistical, and machine-learning technologies to solve important research questions in extreme precipitation projections. The results of this dissertation reconfirm the increasing trend of extreme precipitation and provide improved projection of future extreme precipitation.

5.1.1 Improving Extreme Precipitation Modeling for Better Serial Dependency using Markov Chains

In Chapter 2, an analytical method based on the Markov Chain and dynamic optimization was proposed to incorporate dependency between different days and non-stationarity. The method assumes that the precipitation in each day is a random variable where the distribution depends on the precipitation value of the previous day. The dependency is modeled as a Markov Chain, where different states represent different precipitation status. The whole precipitation process can then be described with the help of the Gamma distribution. The analytical framework is

mostly based on dynamic optimization and Monte Carlo simulation, where the first method can be used to derive the exact distribution mathematically, and the second method can be used to find highly accurate approximation for complicated events. Such a method is able to analyze extreme precipitation events, such as amount of consecutive precipitation. The validation is performed by analyzing the precipitation distribution of various events for three cities in the US, where in all cities a high accuracy is obtained. After validating the results based on three areas of the US, spanning more than five decades, it is concluded that this method can improve the analysis result significantly.

Many prior works with a similar goal use a GEV-based method, which can be limited in the types of events that they can analyze. Furthermore, independence assumption is indeed so that GEV analysis can be applied. Compared to these works, the new method proposed in this chapter is more flexible since it can analyze a wider set of events easily. The required assumption of the analysis is Markov assumptions, which are validated rigorously before being used. Therefore, the methods proposed in this chapter can be a good complementary analysis to GEV in many situations.

5.1.2 Improving Extreme Precipitation Projection based on Downscaled GCM using Copulas

Chapter 3 studies extreme precipitation projection on local areas. Most existing methods for future climate projections are based on GCM or downscaled GCM simulations, which are accurate for average-case precipitation. However, the accuracy

for extreme-case precipitation has not been studied thoroughly. This chapter systemically studies the performance of different downscaled GCM simulations in the context of extreme precipitation. The main method used in this study is based on copulas, which make it possible to split the marginal distribution and the interdependency of two correlated random variables. By using a bivariate copula, historical observed marginal distribution and copula are compared against ones obtained from the downscaled GCM simulations. It is then observed that, although the marginal distributions are similar, there is a significant difference between observed copulas and downscaled GCM copulas, which cause the analysis based on downscaled GCM inaccurate. To improve the accuracy for downscaled GCM simulations, another feature from the copula is used, where historical copulas are extracted and combined with future marginal distribution. This produces a new distribution for future precipitation with improved reliability. The results are validated in 18 combinations of downscaled GCM models and improved projection results are provided for the next century.

This work proposed a novel use of copula in extreme precipitation downscaling. By using copula to decompose the marginal distribution of the daily precipitation and the interdependency, this work is able to reduce the downscaling error significantly especially when used for extreme precipitation analysis. The observation that interdependency of daily precipitation stays mostly stable while the marginal distribution is becoming more extreme can be of high value to future research on understanding extreme precipitation.

5.1.3 Improving Future Intensity-Duration-Frequency Curve Projection for Short Periods using Machine Learning

Chapter 4 studies how to perform future projections of IDF curves, especially for short durations. Most prior works use GCM or downscaled GCM simulations to compute IDF curves, but these data are provided only on a daily basis for many recent downscaling methods, including NASA's openNEX project. Projecting IDF curves for short periods, such as one hour, using daily data can cause huge error due to the exponential tail of an IDF curve. Inspired by geographic downscaling, this chapter presents a method for temporal downscaling that can map precipitation data for long periods to ones for short periods. By further incorporating machine-learning, a high accuracy can be achieved. In more detail, the method computes a feature vector for each station and computes the precipitation intensity for each station. A machine-learning algorithm is used to model the feature-label relationship so that future precipitation intensity can be learned directly using future feature vectors. With the use of an advanced machine-learning algorithm, a high accuracy can be obtained. The IDF curve for future periods is projected in eight cities in the US, which are also validated with NOAA Atlas 14 intensity.

Many existing works on IDF curve projection considering climate change are focused on long-duration precipitation with a duration more than a day. These results cannot be directly used for short-duration projection because almost all GCM simulation data provides only daily results. This work provides novel methods based on ML to solve this problem. The main idea is to perform a temporal downscaling

and directly use them to obtain precipitation intensities for short durations. This idea sheds light on better approaches for future extreme IDF curve projections.

5.2 Future Directions

There are many interesting future directions following the results from this dissertation:

1. This dissertation mainly focuses on extreme precipitation, but the method used in this study can be applied to other extreme climate conditions with ease. Notably, it is believed that more complicated analysis taking multiple climate events (e.g., precipitation and wind speed) into consideration is also feasible using the method from this dissertation.

2. Correlation and dependency analysis can also be used to study climate events and social events. By using copulas, it is possible to explore the risk of climate change to real life by considering, for example, how car accidents have been affected by the increase in extreme precipitation.

3. Due to the need of short period precipitation data, a useful and important future direction is to perform extensive temporal downscaling for future GCM projection results with high reliability so that IDF curve computation for short periods can be made easier.

4. The study of extreme precipitation presented in this study mostly focuses on the accuracy for each station without considering too much about geographic

consistency. Future work should explore the level of geographic consistency that the methods provide and how to improve it without reducing the accuracy per station.

Appendix A: Gamma Distribution

Gamma distribution is one of the most popularly used distributions to model daily precipitation [91, 135]. It can be viewed as a general form of Erlang distribution, which represents the sum of a set of independent exponential distributions. The probabilistic density function of gamma distribution is

$$f(x) = \frac{1}{\Gamma(\alpha)} \left(\frac{x}{\beta}\right)^{\alpha-1} e^{-\frac{x}{\beta}} \tag{A.1}$$

where α and β are shape and scale parameters. Note that gamma distribution cannot take zero values. Therefore, when used to model daily precipitation, days with no precipitation cannot be included in the distribution.

Appendix B: Markov Chain Model

Markov chain model is a mathematical tool used to model how a sequence of events are dependent to each other. There are mainly three main components in a Markov chain model: 1) the state space; 2) the transitioning relation between different states; 3) the initial state distribution.

Let $X_1, \ldots, X_n$ is a sequence of events that can be dependent to each other. In general it is difficult to analyze them if the dependency can be arbitrary. However, in many cases, the dependency relationship between a sequence of random variables are regular. In particular, for time-series random variables, the event happening at time i only depends on the events happened before i, that is to say, X_i only depends on $X_1, \ldots, X_{i-1}$. Further, such dependency can often be memoryless, that is X_i only depends on k previous events. If a sequence of events satisfy these conditions, it is called as a Markov Process and the underlying sequence of events is called a Markov Chain. Mathematically speaking,

$$\Pr\{X_i | X_1, \ldots, X_{i-1}\} = \Pr\{X_i | X_1, \ldots, X_{i-k+1}\}$$

The state space of a Markov chain can be viewed as a finite set of labels each corresponds to some concrete events in the system being analyzed. The transiting

relationship describes how one can move from one state to another state in the next time-step. One important assumption in the Markov chain model is that the transition of states only depends on a limited number of prior states. The transitioning probability and therefore be viewed as a function of the current state and the prior states. When X_i can only take values from a finite set, such a Markov Chain is said to have a finite state space. Markov Chain has extensive applications in reality because of its ability to model dependency relationships.

Appendix C: Copula

Copula is a mathematical concept used to model the interdependency between two random variables. Assume that there are d random variables, namely $X_1, \ldots, X_d$, with marginal cumulative distribution functions (CDFs) $F_1(\cdot)$, $\ldots$, $F_d(\cdot)$, the joint CDF of these d random variables are defined to be

$$F(x_1, \ldots, x_d) = \Pr(X_1 \leq x_1, \ldots, X_d \leq x_d) \tag{C.1}$$

Given the above, the marginal CDF of each random variable X_i can be written as

$$F_i(x_i) = \Pr(X_i \leq x_i) = \int_{-\infty}^{\infty} \ldots \int_{-\infty}^{\infty} F(x_1, \ldots, x_d) dx_1 \ldots dx_{i-1} dx_{i+1} \ldots dx_d \tag{C.2}$$

According to the probability integral transform, for any random variable X with CDF $F_X(\cdot)$, it is always true that $F_X(X)$ follows a uniform distribution between 0 and 1. A copula of d random variables $X_1, \ldots, X_d$ is defined as

$$C(u_1, \ldots, u_d) \equiv \Pr\left(X_1 \leq F_1^{-1}(u_1), \ldots, X_d \leq F_d^{-1}(u_d)\right) \tag{C.3}$$

Applying probability integral transform, it can be further simplified:

$$\begin{aligned} C(u_1, \ldots, u_d) &= \Pr\left(F_1(X_1) \leq u_1, \ldots, F_d(X_d) \leq u_d\right) \\ &= \Pr\left(U_1 \leq u_1, \ldots, U_d \leq u_d\right) \end{aligned} \tag{C.4}$$

Here, U_i is integral transformed random variables of X_i following a uniform distribution between 0 and 1, and that $u_i \in [0, 1]$ for each $i \in \{1, \ldots, d\}$.

According to Sklar's theorem [136], one important property of copulas is that the copula function $C(\cdot)$, together with marginal distributions $F_1(\cdot)$, $\ldots$, $F_d(\cdot)$, completely describe the joint distribution of a set of random variables. That is,

$$F(x_1, \ldots, x_d) = C(F_1(x_1), \ldots, F_d(x_d)) \tag{C.5}$$

Since marginal distributions do not describe any dependency or correlation, it is the copula function that contains all dependency information. Copula has been important in understanding dependency of random variables because copulas are not related to the distributions themselves but only how distributions are correlated.

For bivariate cases, the above equation can be simplified as follows:

$$F(x_1, x_1) = C(F_1(x_1), F_2(x_2)) \tag{C.6}$$

Bivariate copulas can be presented using two-dimensional contour figures. For example, Figure C.1 shows the 3D plot and corresponding contour plot for the same copula. The maximum value is 1, which appears at $(1, 1)$. Since copula can take

values from 0 to 1, contour lines are plotted for 0.15, 0.3, 0.45, 0.6, 0.75, 0.9.

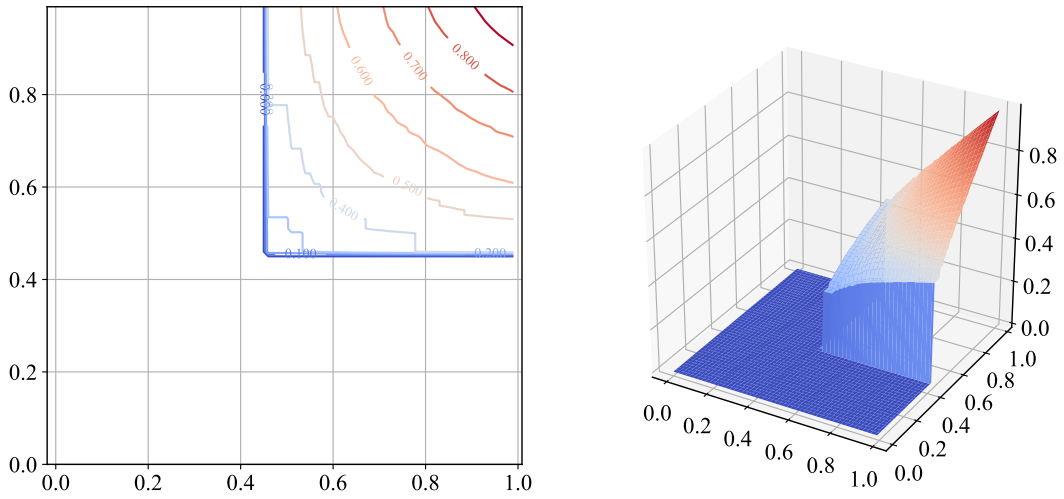

Figure C.1: Illustration of a bivariate copula function: (a) Contour plot; (b) Three-dimensional plot

C.1 Archimedean Copulas

Archimedean copulas a class of copulas that are useful in practice. Intuitively, Archimedean copulas are highly symmetric and have explicitly formulas with only one degree of freedom. This typically means that the shape of the copula is fixed and the strength of the copula can be easily tuned using this single parameter, and thus quantify the dependency beyond simple linear dependencies. Popular Archimedean copulas include Gumbel copula, Clayton copula and so on [137, 138, 139].

C.2 Empirical Copulas

Archimedean copulas may not always be applicable to all applications due to, for example, 1) all Archimedean copula models are parametric, but there may not be

enough data for a reliable fitting to obtain the parameter; and 2) the dependency between realistic random variables can be irregular and thus causes a high error if using these popular copula models.

To overcome the above difficulties, an empirical copula can be used instead. Empirical copulas are nonparametric and can be computed directly using samples drawn from the joint distribution. In more detail, the empirical marginal distribution of n pairs of first and the second random variables can be computed as follows respectively

$$\begin{aligned} F_1(x) &= \frac{1}{n-1} \sum_{i=1}^{n-1} I\left(X_i \leq x\right) \\ F_2(x) &= \frac{1}{n-1} \sum_{i=2}^{n} I\left(X_i \leq x\right) \end{aligned} \tag{C.7}$$

In the above equations, $I(\cdot)$ is an indicator random variable that has value 1 if the condition inside holds, and 0 otherwise. For example, $I\left(X_i \leq x\right)$ is 1 if $X_i \leq x$ is true, and 0 otherwise. The summation counts the number of days with precipitation less than x in the first $n-1$ days.

When n is reasonably large, both of them can be approximated using the same CDF, namely $F()$ as follows:

$$F_1(x) \approx F_2(x) \approx F(x) = \frac{1}{n} \sum_{i=1}^{n} I\left(X_i \leq x\right) \tag{C.8}$$

Now the empirical copula can be computed following the discrete version of proba-

bility integral transform by applying Eq. C.4:

$$\begin{aligned} C(u_1, u_2) &= \frac{1}{n-1} \sum_{i=1}^{n-1} I\left(F_1(X_i) \leq u_1, F_2(X_{i+1}) \leq u_2\right) \\ &\approx \frac{1}{n-1} \sum_{i=1}^{n-1} I\left(F(X_i) \leq u_1, F(X_{i+1}) \leq u_2\right) \end{aligned} \tag{C.9}$$

Although the above empirical copula is nonparametric, the computation cost can be much higher than a direct fitting to some formulas.

Appendix D: Machine Learning

Machine learning techniques have been mostly developed in the field of statistics and computer sciences as ways to learn specific inherent relational properties of the data without explicitly describing the details of the relationship.

Supervised machine learning is one kind of machine learning algorithm. Such algorithms can learn a relational property from one dataset and then apply the relation to other datasets to predict how the data should look given the predicted relation. These algorithms have been used in many related works on studying precipitation. For example, Foresti et al. [140] used neural networks to model extreme precipitation; A survey by Vandal et al. [141] used machine learning for statistical downscaling.

A supervised machine learning algorithm usually uses labeled data as the input and trains a model from it. This model can be used to predict the label of some unlabeled data. There are four concepts associated with any supervised machine learning algorithm:

- **Features.** Feature (X) refers to the properties of the data that are known for the training dataset and projection datasets.

- **Label.** Label (Y) refers to the property that is only known for the training

dataset and is unknown in the projection dataset. The goal is to predict the label for projection data using their features.

- **Training phase.** This is a procedure where a set of data is available, such that both features and labels are given for each data entry. The training phase takes these data entries as input and produces a compact description, namely the ML model, which describes the input–output relationship.

- **Prediction phase.** This is a procedure where a set of data, namely the testing data, is given but with features without labels only. The procedure also takes the model obtained above as input and outputs a label for each entry of the training data.

A machine learning model is said to be good if the predicted labels are consistent with their actual values. The task of a supervised machine learning algorithm is to determine the labels of all data in the testing set by using information from the training dataset. Depending on the nature of the problem and the structure of the data, some machine learning algorithms can be more useful than others. State-of-the-art supervised machine learning algorithms include the supported vector machine, the gradient boosting tree, the deep neural networks, etc.

Appendix E: Dataset Description

E.1 Precipitation Observation Dataset

In Chapter 2, 3 and 4, historical precipitation data with different range, duration, location are used. The Climate Data Online (CDO) platform maintains global historical weather and climate data (accessible at [1]).

The data are categorized into temperature, precipitation and wind data. These data are recorded with different durations, including hourly, daily, monthly, seasonal, and yearly data. Two different durations are used depending on the research focus in different chapters: observed daily precipitation data are used in Chapter 2 and 3; observed 15-minutes precipitation data are used in Chapter 4. The variables used in this research include station id, location information, date and precipitation values.

The data can be downloaded in comma separated values (.csv) file , which can then be processed using different softwares.

E.2 Downscaled Global Climate Model Dataset

In Chapter 3 and Chapter 4, three sets of publicly accessible downscaled GCM datasets are used. The Climate Model Data Services (CDS) holds NEX-GDDP

dataset, which can be accessed at [134]. The US Geological Survey (USGS) Geo Data Portal holds various downscaling datasets including LOCA and MACA datasets (accessible at [142]).

Generally, all three downscaled dataset contains outputs from various downscaled GCMs of CMIP5. The coverage varies with different spatial resolutions. The datasets provide results for historical period, and future projection period with two scenarios (RCP 4.5 and 8.5). Basic information and differences of these three datasets are summarized in Table E.1.

Data properties	GDDP [1]	LOCA [2]	MACA [3]
Historical period	1950 - 2005	1950 - 2005	1950 - 2005
Projection period	2006 - 2100	2006 - 2100	2006 - 2100
Future scenarios	RCP 4.5, 8.5	RCP 4.5, 8.5	RCP 4.5, 8.5
Source of models	CMIP5	CMIP5	CMIP5
Number of models	21	32	20
Spatial resolution	25 km	6.25 km	4 km
Coverage	the whole globe	the North America	Conterminous USA

[1] GDDP: NASA Earth Exchange Global Daily Downscaled Projections
[2] LOCA: Localized Constructed Analogs
[3] MACA: Multivariate Adaptive Constructed Analogs

Table E.1: Basic information of three downscaled GCM datasets

All three datasets include the following variables:

- pr - Average daily precipitation amount at surface (units: $kg/m^2/s$)
- tasmax - Maximum daily air temperature near surface
- tasmin - Minimum daily air temperature near surface

E.3 NOAA Atlas 14 Dataset

In Chapter 4, NOAA Atlas 14 dataset is used for comparison. NOAA's National Weather Service maintains data for Atlas 14 (accessible at [133]). The dataset provides precipitation frequency estimates for areas across the US. However, five states are not available currently: Washington, Oregon, Montana, Wyoming, and Idaho. This dataset is prepared by NOAA and is believed to be very reliable and accurate.

The precipitation frequency estimates from the dataset are based on frequency analysis of partial duration series. For each station, the duration ranges from 5 minutes to 60 days, while the return period ranges from 1 year to 1000 years.

Bibliography

[1] NOAA. Climate data online. `http://www.ncdc.noaa.gov/cdo-web/`, 2016. "[Online; accessed 30-March-2016]".

[2] USGCRP. Impacts, risks, and adaptation in the united states: Fourth national climate assessment. II:1515, 2018.

[3] IPCC. Summary for policymakers. in: Global warming of 1.5 degree. an ipcc special report on the impacts of global warming of 1.5 degree above pre-industrial levels and related global greenhouse gas emission pathways, in the context of strengthening the global response to the threat of climate change, sustainable development, and efforts to eradicate poverty. 2018.

[4] Climate Vulnerability Monitor. A guide to the cold calculus of a hot planet. In *DARA and the Climate Vulnerable Forum Climate Vulnerability Monitor-Madrid*, 2012.

[5] IPCC. Managing the Risks of Extreme Events and Disasters to Advance Climate Change Adaptation: Special Report of the Intergovernmental Panel on Climate Change. Cambridge University Press, 2012.

[6] David R Easterling, Gerald A Meehl, Camille Parmesan, Stanley A Changnon, Thomas R Karl, and Linda O Mearns. Climate extremes: observations, modeling, and impacts. *science*, 289(5487):2068–2074, 2000.

[7] LV Alexander, Xuebin Zhang, TC Peterson, John Caesar, B Gleason, AMG Klein Tank, M Haylock, Dean Collins, Blair Trewin, Fatemah Rahimzadeh, et al. Global observed changes in daily climate extremes of temperature and precipitation. *Journal of Geophysical Research: Atmospheres*, 111(D5), 2006.

[8] Franklin T Lombardo and Bilal M Ayyub. Analysis of washington, dc, wind and temperature extremes with examination of climate change for engineering applications. *ASCE-ASME Journal of Risk and Uncertainty in Engineering Systems, Part A: Civil Engineering*, 1(1):04014005, 2014.

[9] Chunlüe Zhou, Kaicun Wang, and Dan Qi. Attribution of the july 2016 extreme precipitation event over chinas wuhang. *Bulletin of the American Meteorological Society*, 99(1):S107–S112, 2018.

[10] Nicola Pedroni, E Zio, A Pasanisi, and M Couplet. Empirical comparison of two methods for the bayesian update of the parameters of probability distributions in a two-level hybrid probabilistic-possibilistic uncertainty framework for risk assessment. *ASCE-ASME Journal of Risk and Uncertainty in Engineering Systems, Part A: Civil Engineering*, 2(1):04015015, 2015.

[11] Xuan Guo and ZhiQiang Chen. Lifecycle multihazard framework for assessing flood scour and earthquake effects on bridge failure. *ASCE-ASME Journal of Risk and Uncertainty in Engineering Systems, Part A: Civil Engineering*, 2(2):C4015004, 2015.

[12] Dalia Kirschbaum, Robert Adler, David Adler, Christa Peters-Lidard, and George Huffman. Global distribution of extreme precipitation and high-impact landslides in 2010 relative to previous years. *Journal of Hydrometeorology*, 13(5):1536–1551, 2012.

[13] Alan K Knapp, Claus Beier, David D Briske, Aimée T Classen, Yiqi Luo, Markus Reichstein, Melinda D Smith, Stanley D Smith, Jesse E Bell, Philip A Fay, et al. Consequences of more extreme precipitation regimes for terrestrial ecosystems. *AIBS Bulletin*, 58(9):811–821, 2008.

[14] Philippe Lopez. Cloud and precipitation parameterizations in modeling and variational data assimilation: A review. *Journal of the Atmospheric Sciences*, 64(11):3766–3784, 2007.

[15] Keith J Beven and George M Hornberger. Assessing the effect of spatial pattern of precipitation in modeling stream flow hydrographs. *JAWRA Journal of the American Water Resources Association*, 18(5):823–829, 1982.

[16] Robert F Adler, George J Huffman, Alfred Chang, Ralph Ferraro, Ping-Ping Xie, John Janowiak, Bruno Rudolf, Udo Schneider, Scott Curtis, David Bolvin, et al. The version-2 global precipitation climatology project (gpcp) monthly precipitation analysis (1979–present). *Journal of hydrometeorology*, 4(6):1147–1167, 2003.

[17] Viviane BS Silva, Vernon E Kousky, Wei Shi, and R Wayne Higgins. An improved gridded historical daily precipitation analysis for brazil. *Journal of Hydrometeorology*, 8(4):847–861, 2007.

[18] George J Huffman, David T Bolvin, Eric J Nelkin, David B Wolff, Robert F Adler, Guojun Gu, Yang Hong, Kenneth P Bowman, and Erich F Stocker. The trmm multisatellite precipitation analysis (tmpa): Quasi-global, multiyear, combined-sensor precipitation estimates at fine scales. *Journal of hydrometeorology*, 8(1):38–55, 2007.

[19] Ana Paula Barros and Dennis P Lettenmaier. Dynamic modeling of orographically induced precipitation. *Reviews of geophysics*, 32(3):265–284, 1994.

[20] Lars S Hanson and Richard Vogel. The probability distribution of daily rainfall in the united states. In *World Environmental and Water Resources Congress*, pages 1–10, 2008.

[21] Yun Li, Wenju Cai, and EP Campbell. Statistical modeling of extreme rainfall in southwest western australia. *Journal of Climate*, 18(6):852–863, 2005.

[22] WW Ng and US Panu. Comparisons of traditional and novel stochastic models for the generation of daily precipitation occurrences. *Journal of hydrology*, 380(1-2):222–236, 2010.

[23] Kenneth E Kunkel, Karen Andsager, and David R Easterling. Long-term trends in extreme precipitation events over the conterminous united states and canada. *Journal of climate*, 12(8):2515–2527, 1999.

[24] Yuqing Wang and Li Zhou. Observed trends in extreme precipitation events in china during 1961–2001 and the associated changes in large-scale circulation. *Geophysical Research Letters*, 32(9), 2005.

[25] Ana Cristina Costa and Amílcar Soares. Trends in extreme precipitation indices derived from a daily rainfall database for the south of portugal. *International Journal of Climatology*, 29(13):1956–1975, 2009.

[26] K Toride, DL Cawthorne, K Ishida, ML Kavvas, and ML Anderson. Long-term trend analysis on total and extreme precipitation over shasta dam watershed. *The Science of the total environment*, 626:244–254, 2018.

[27] Daniel Cooley, Douglas Nychka, and Philippe Naveau. Bayesian spatial modeling of extreme precipitation return levels. *Journal of the American Statistical Association*, 102(479):824–840, 2007.

[28] Seita Emori and SJ Brown. Dynamic and thermodynamic changes in mean and extreme precipitation under changed climate. *Geophysical Research Letters*, 32(17), 2005.

[29] Levon Demirdjian, Yaping Zhou, and George J Huffman. Statistical modeling of extreme precipitation with trmm data. *Journal of Applied Meteorology and Climatology*, 57(1):15–30, 2018.

[30] Seung-Ki Min, Xuebin Zhang, Francis W Zwiers, and Gabriele C Hegerl. Human contribution to more-intense precipitation extremes. *Nature*, 470(7334):378, 2011.

[31] Paul A O'Gorman and Tapio Schneider. The physical basis for increases in precipitation extremes in simulations of 21st-century climate change. *Proceedings of the National Academy of Sciences*, 106(35):14773–14777, 2009.

[32] Stephan Pfahl, Paul A OGorman, and Erich M Fischer. Understanding the regional pattern of projected future changes in extreme precipitation. *Nature Climate Change*, 7(6):423, 2017.

[33] Andrea Libertino, Paola Allamano, Francesco Laio, and Pierluigi Claps. Regional-scale analysis of extreme precipitation from short and fragmented records. *Advances in Water Resources*, 112:147–159, 2018.

[34] Silvano Bertoldo, Claudio Lucianaz, and Marco Allegretti. Extreme rainfall event analysis using rain gauges in a variety of geographical situations. *ATMOSPHERIC AND CLIMATE SCIENCE*, 5(2):82–90, 2015.

[35] Linyin Cheng, Amir AghaKouchak, Eric Gilleland, and Richard W Katz. Nonstationary extreme value analysis in a changing climate. *Climatic change*, 127(2):353–369, 2014.

[36] Oli G. B. Sveinsson, Jose D. Salas, and Duane C. Boes. Regional Frequency Analysis of Extreme Precipitation in Northeastern Colorado and Fort Collins Flood of 1997. Journal of Hydrologic Engineering, 2002.

[37] PCD Milly, B Julio, F Malin, M Robert, W Zbigniew, P Dennis, and J Ronald. Stationarity is dead. *Ground Water News & Views*, 4(1):6–8, 2007.

[38] Richard W Katz. Statistical methods for nonstationary extremes. In *Extremes in a Changing Climate*, pages 15–37. Springer, 2013.

[39] Jonathan Jalbert, Anne-Catherine Favre, Claude Bélisle, and Jean-François Angers. A spatiotemporal model for extreme precipitation simulated by a climate model, with an application to assessing changes in return levels over north america. *Journal of the Royal Statistical Society: Series C (Applied Statistics)*, 66(5):941–962, 2017.

[40] Song Feng, Saralees Nadabajah, and Qi Hu. Modeling annual extreme precipitation in china using the generalized extreme value distribution. *Journal of the Meteorological Society of Japan*, 85(5):599–613, 2007.

[41] Ashok K Mishra and Vijay P Singh. Changes in extreme precipitation in texas. *Journal of Geophysical Research: Atmospheres*, 115(D14), 2010.

[42] Dao Nguyen Khoi and Hoang Thi Trang. Analysis of changes in precipitation and extremes events in ho chi minh city, vietnam. *Procedia Engineering*, 142:228–234, 2016.

[43] E Joetzjer, H Douville, C Delire, and P Ciais. Present-day and future amazonian precipitation in global climate models: Cmip5 versus cmip3. *Climate Dynamics*, 41(11-12):2921–2936, 2013.

[44] Timothy Andrews, Jonathan M Gregory, Mark J Webb, and Karl E Taylor. Forcing, feedbacks and climate sensitivity in cmip5 coupled atmosphere-ocean climate models. *Geophysical Research Letters*, 39(9), 2012.

[45] Karl E Taylor, Ronald J Stouffer, and Gerald A Meehl. An overview of cmip5 and the experiment design. *Bulletin of the American Meteorological Society*, 93(4):485–498, 2012.

[46] BC Hewitson and RG Crane. Climate downscaling: techniques and application. *Climate Research*, pages 85–95, 1996.

[47] BC Hewitson and RG Crane. Consensus between gcm climate change projections with empirical downscaling: precipitation downscaling over south africa. *International Journal of Climatology*, 26(10):1315–1337, 2006.

[48] Peter G Jones, Philip K Thornton, and Jens Heinke. Generating characteristic daily weather data using downscaled climate model data from the ipcc's fourth assessment. *ILRI*, 2009.

[49] Yun Bao and Xinyu Wen. Projection of china's near-and long-term climate in a new high-resolution daily downscaled dataset nex-gddp. *Journal of Meteorological Research*, 31(1):236–249, 2017.

[50] David W Pierce, Daniel R Cayan, and Bridget L Thrasher. Statistical downscaling using localized constructed analogs (loca). *Journal of Hydrometeorology*, 15(6):2558–2585, 2014.

[51] John T Abatzoglou and Timothy J Brown. A comparison of statistical downscaling methods suited for wildfire applications. *International Journal of Climatology*, 32(5):772–780, 2012.

[52] Alain Mailhot and Sophie Duchesne. Design criteria of urban drainage infrastructures under climate change. *Journal of Water Resources Planning and Management*, 136(2):201–208, 2009.

[53] Ajay Saini and Iris Tien. Impacts of climate change on the assessment of long-term structural reliability. *ASCE-ASME Journal of Risk and Uncertainty in Engineering Systems, Part A: Civil Engineering*, 3(3):04017003, 2017.

[54] Richard W Katz. Precipitation as a chain-dependent process. *Journal of Applied Meteorology*, 16(7):671–676, 1977.

[55] Senthamarai K Kannan and Jawahar A Farook. Stochastic simulation of precipitation using markov chain-mixed exponential model. *Applied Mathematical Sciences*, 65(9):3205–3212, 2015.

[56] Reza Hosseini, Nhu Le, and Jim Zidek. Selecting a binary markov model for a precipitation process. *Environmental and ecological statistics*, 18(4):795–820, 2011.

[57] Ying Sun, Michael L Stein, et al. A stochastic space-time model for intermittent precipitation occurrences. *The Annals of Applied Statistics*, 9(4):2110–2132, 2015.

[58] Hui Wan, Xuebin Zhang, and Elaine M Barrow. Stochastic modelling of daily precipitation for canada. *Atmosphere-Ocean*, 43(1):23–32, 2005.

[59] Mohammad Reza Najafi, Hamid Moradkhani, and Susan A Wherry. Statistical downscaling of precipitation using machine learning with optimal predictor selection. *Journal of Hydrologic Engineering*, 16(8):650–664, 2010.

[60] Umut Okkan and Gul Inan. Bayesian learning and relevance vector machines approach for downscaling of monthly precipitation. *Journal of Hydrologic Engineering*, 20(4):04014051, 2014.

[61] Elmira Hassanzadeh, Alireza Nazemi, and Amin Elshorbagy. Quantile-based downscaling of precipitation using genetic programming: application to idf curves in saskatoon. *Journal of Hydrologic Engineering*, 19(5):943–955, 2013.

[62] Jonas Olsson, CB Uvo, K Jinno, A Kawamura, K Nishiyama, N Koreeda, T Nakashima, and O Morita. Neural networks for rainfall forecasting by atmospheric downscaling. *Journal of Hydrologic Engineering*, 9(1):1–12, 2004.

[63] Manish Kumar Goyal, Donald H Burn, and CSP Ojha. Precipitation simulation based on k-nearest neighbor approach using gamma kernel. *Journal of Hydrologic Engineering*, 18(5):481–487, 2012.

[64] Megan C Kirchmeier-Young, David J Lorenz, and Daniel J Vimont. Extreme event verification for probabilistic downscaling. *Journal of Applied Meteorology and Climatology*, 55(11):2411–2430, 2016.

[65] Gerd Bürger, SR Sobie, AJ Cannon, AT Werner, and TQ Murdock. Downscaling extremes: An intercomparison of multiple methods for future climate. *Journal of Climate*, 26(10):3429–3449, 2013.

[66] Hugo G Hidalgo, Michael D Dettinger, and Daniel R Cayan. Downscaling with constructed analogues: Daily precipitation and temperature fields over the united states. *California Energy Commission PIER Final Project Report CEC-500-2007-123*, 2008.

[67] Michael K Tippett and Timothy DelSole. Constructed analogs and linear regression. *Monthly Weather Review*, 141(7):2519–2525, 2013.

[68] K. van der Wiel, S. B. Kapnick, G. J. van Oldenborgh, K. Whan, S. Philip, G. A. Vecchi, R. K. Singh, J. Arrighi, and H. Cullen. Rapid attribution of the august 2016 flood-inducing extreme precipitation in south louisiana to climate change. *Hydrology and Earth System Sciences Discussions*, 2016:1–40, 2016.

[69] Daniele Norbiato, Marco Borga, Marco Sangati, and Francesco Zanon. Regional frequency analysis of extreme precipitation in the eastern italian alps and the august 29, 2003 flash flood. *Journal of hydrology*, 345(3-4):149–166, 2007.

[70] Henrik Madsen, Deborah Lawrence, Michel Lang, Marta Martinkova, and TR Kjeldsen. Review of trend analysis and climate change projections of extreme precipitation and floods in europe. *Journal of Hydrology*, 519:3634–3650, 2014.

[71] Lakshmi Krishnamurthy, Gabriel A Vecchi, Xiaosong Yang, Karin van der Wiel, V Balaji, Sarah B Kapnick, Liwei Jia, Fanrong Zeng, Karen Paffendorf, and Seth Underwood. Causes and probability of occurrence of extreme precipitation events like chennai 2015. *Journal of Climate*, (2018), 2018.

[72] Linyin Cheng and Amir AghaKouchak. Nonstationary precipitation intensity-duration-frequency curves for infrastructure design in a changing climate. *Scientific reports*, 4:7093, 2014.

[73] Andreas Langousis and Daniele Veneziano. Intensity-duration-frequency curves from scaling representations of rainfall. *Water Resources Research*, 43(2), 2007.

[74] Ibrahim H Elsebaie. Developing rainfall intensity–duration–frequency relationship for two regions in saudi arabia. *Journal of King Saud University-Engineering Sciences*, 24(2):131–140, 2012.

[75] ASCE Standard Committee. Flood resistant design and construction. Technical report, Reston, Va, 2005.

[76] Roger T. Kilgore, George (Rudy) Herrmann, Wilbert O. Thomas Jr., and David B. Thompson. Highways in the river environment- floodplains, extreme events, risk, and resilience. Technical report, Federal Highway Administration, 2016.

[77] Huiling Hu and Bilal M Ayyub. Extreme precipitation analysis and prediction for a changing climate. *ASCE-ASME Journal of Risk and Uncertainty in Engineering Systems, Part A: Civil Engineering*, 4(3):04018029, 2018.

[78] Bilal M Ayyub and Richard H McCuen. *Probability, statistics, and reliability for engineers and scientists*. CRC press, 2016.

[79] Boris Vladimirovich Gnedenko. On a local limit theorem of the theory of probability. *Uspekhi Matematicheskikh Nauk*, 3(3):187–194, 1948.

[80] Marcelino Q Villafuerte and Jun Matsumoto. Significant influences of global mean temperature and enso on extreme rainfall in southeast asia. *Journal of Climate*, 28(5):1905–1919, 2015.

[81] Hongwei Shang, Jun Yan, Mekonnen Gebremichael, and Semu M Ayalew. Trend analysis of extreme precipitation in the northwestern highlands of ethiopia with a case study of debre markos. *Hydrology and Earth System Sciences*, 15(6):1937–1944, 2011.

[82] Richard W Katz. Statistics of extremes in climate change. *Climatic Change*, 100(1):71–76, 2010.

[83] Norbert A Agana, Mohammad Gorji Sefidmazgi, and Abdollah Homaifar. Analysis of nonstationary extreme events. In *MAICS*, pages 7–11, 2015.

[84] Richard W Katz, Marc B Parlange, and Philippe Naveau. Statistics of extremes in hydrology. *Advances in water resources*, 25(8):1287–1304, 2002.

[85] D Panagoulia, P Economou, and C Caroni. Stationary and nonstationary generalized extreme value modelling of extreme precipitation over a mountainous area under climate change. *Environmetrics*, 25(1):29–43, 2014.

[86] Demetris Koutsoyiannis. Statistics of extremes and estimation of extreme rainfall: Ii. empirical investigation of long rainfall records/statistiques de valeurs extrêmes et estimation de précipitations extrêmes: Ii. recherche empirique sur de longues séries de précipitations. *Hydrological Sciences Journal*, 49(4), 2004.

[87] Viatcheslav V Kharin, Francis W Zwiers, Xuebin Zhang, and Gabriele C Hegerl. Changes in temperature and precipitation extremes in the ipcc ensemble of global coupled model simulations. *Journal of Climate*, 20(8):1419–1444, 2007.

[88] AMG Klein Tank and GP Können. Trends in indices of daily temperature and precipitation extremes in europe, 1946–99. *Journal of climate*, 16(22):3665–3680, 2003.

[89] Olga Zolina, Alice Kapala, Clemens Simmer, and Sergey K Gulev. Analysis of extreme precipitation over europe from different reanalyses: a comparative assessment. *Global and Planetary Change*, 44(1-4):129–161, 2004.

[90] Singiresu S. Rao. Dynamic programming, in engineering optimization: Theory and practice. John Wiley and Sons, Inc., 2009.

[91] Gregory J Husak, Joel Michaelsen, and Chris Funk. Use of the gamma distribution to represent monthly rainfall in africa for drought monitoring applications. *International Journal of Climatology*, 27(7):935–944, 2007.

[92] NOAA. Climate division. `https://www.ncdc.noaa.gov/monitoring-references/maps/us-climate-divisions.php`, 2016. "[Online; accessed 20-Feburary-2019]".

[93] VB Bagdonavicius and MS Nikulin. Chi-squared goodness-of-fit test for right censored data. *International Journal of Applied Mathematics and Statistics*, 24(SI-11A):30–50, 2011.

[94] Huiling Hu and Bilal M Ayyub. Validating and enhancing extreme precipitation projections by downscaled global climate model results and copula methods. *Journal of Hydrologic Engineering*, 24(7):04019019, 2019.

[95] JM Melillo, TC Richmond, and GW Yohe. Climate change impacts in the united states: The third national climate assessment. us global change research program, 841 pp. doi: 10.7930/j0z31wj2. *Online at: nca2014. globalchange. gov*, 2014.

[96] Richard H McCuen et al. *Hydrologic analysis and design*, volume 3. Prentice Hall, 2016.

[97] Mohammad Karamouz, Sara Nazif, and Zahra Zahmatkesh. Self-organizing gaussian-based downscaling of climate data for simulation of urban drainage systems. *Journal of Irrigation and Drainage Engineering*, 139(2):98–112, 2013.

[98] Zachary T Schuster, Kenneth W Potter, and David S Liebl. Assessing the effects of climate change on precipitation and flood damage in wisconsin. *Journal of Hydrologic Engineering*, 17(8):888–894, 2011.

[99] Yongkang Xue, Ratko Vasic, Zavisa Janjic, Fedor Mesinger, and Kenneth E Mitchell. Assessment of dynamic downscaling of the continental us regional climate using the eta/ssib regional climate model. *Journal of Climate*, 20(16):4172–4193, 2007.

[100] Bertrand Denis, René Laprise, Daniel Caya, and Jean Côté. Downscaling ability of one-way nested regional climate models: the big-brother experiment. *Climate Dynamics*, 18(8):627–646, 2002.

[101] René Laprise. Resolved scales and nonlinear interactions in limited-area models. *Journal of the atmospheric sciences*, 60(5):768–779, 2003.

[102] Andrew W Wood, Lai R Leung, V Sridhar, and DP Lettenmaier. Hydrologic implications of dynamical and statistical approaches to downscaling climate model outputs. *Climatic change*, 62(1-3):189–216, 2004.

[103] Edwin P Maurer. The utility of daily large-scale climate data in the assessment of climate change impacts on daily streamflow in california. 2010.

[104] DL De Luca. Analysis and modelling of rainfall fields at different resolutions in southern italy. *Hydrological Sciences Journal*, 59(8):1536–1558, 2014.

[105] Bellie Sivakumar. Is a chaotic multi-fractal approach for rainfall possible? *Hydrological Processes*, 15(6):943–955, 2001.

[106] Li-Pen Wang, Christian Onof, and Čedo Maksimović. Analysis of sub-daily rainfall sequences based upon a semi-deterministic multiplicative cascade method. In *Proceedings of international workshop on advances in statistical hydrology*, pages 24–25, 2010.

[107] Robert L Wilby, TML Wigley, D Conway, PD Jones, BC Hewitson, J Main, and DS Wilks. Statistical downscaling of general circulation model output: a comparison of methods. *Water resources research*, 34(11):2995–3008, 1998.

[108] Markus G Donat, Lisa V Alexander, H Yang, I Durre, R Vose, and J Caesar. Global land-based datasets for monitoring climatic extremes. *Bulletin of the American Meteorological Society*, 94(7):997–1006, 2013.

[109] AI Agbonaye and OC Izinyon. Best-fit probability distribution model for rainfall frequency analysis of three cities in south eastern nigeria. *Nigerian Journal of Environmental Sciences and Technology (NIJEST) Vol*, 1(1):34–42, 2017.

[110] Tianfeng Chai and Roland R Draxler. Root mean square error (rmse) or mean absolute error (mae)?–arguments against avoiding rmse in the literature. *Geoscientific model development*, 7(3):1247–1250, 2014.

[111] N Schaller, I Mahlstein, J Cermak, and Reto Knutti. Analyzing precipitation projections: A comparison of different approaches to climate model evaluation. *Journal of Geophysical Research: Atmospheres*, 116(D10), 2011.

[112] Salvatore Grimaldi and Francesco Serinaldi. Design hyetograph analysis with 3-copula function. *Hydrological Sciences Journal*, 51(2):223–238, 2006.

[113] G Salvadori and C De Michele. Multivariate multiparameter extreme value models and return periods: A copula approach. *Water resources research*, 46(10), 2010.

[114] Sander Vandenberghe, NEC Verhoest, C Onof, and Bernard De Baets. A comparative copula-based bivariate frequency analysis of observed and simulated storm events: A case study on bartlett-lewis modeled rainfall. *Water Resources Research*, 47(7), 2011.

[115] Davide Luciano De Luca and Daniela Biondi. Bivariate return period for design hyetograph and relationship with t-year design flood peak. *Water*, 9(9):673, 2017.

[116] IG Watterson and MR Dix. Simulated changes due to global warming in daily precipitation means and extremes and their interpretation using the gamma distribution. *Journal of Geophysical Research: Atmospheres*, 108(D13), 2003.

[117] Huiling Hu and Bilal M. Ayyub. Machine learning for projecting extreme precipitation intensity for short durations in a changing climate. *Geosciences Special Issue on Climate Prediction of Extreme Events*, 2019.

[118] Demetris Koutsoyiannis, Demosthenes Kozonis, and Alexandros Manetas. A mathematical framework for studying rainfall intensity-duration-frequency relationships. *Journal of Hydrology*, 206(1-2):118–135, 1998.

[119] CM Tfwala, LD van Rensburg, R Schall, SM Mosia, and P Dlamini. Precipitation intensity-duration-frequency curves and their uncertainties for ghaap plateau. *Climate Risk Management*, 16:1–9, 2017.

[120] John Bougadis and Kaz Adamowski. Scaling model of a rainfall intensity-duration-frequency relationship. *Hydrological Processes*, 20(17):3747–3757, 2006.

[121] J Blanchet, D Ceresetti, G Molinié, and J-D Creutin. A regional gev scale-invariant framework for intensity–duration–frequency analysis. *Journal of hydrology*, 540:82–95, 2016.

[122] S Das. Distribution selection for hydrologic frequency analysis using subsampling method. In *IOP Conference Series: Earth and Environmental Science*, volume 39, page 012059. IOP Publishing, 2016.

[123] Jose Manuel Hidalgo-Muñoz, D Argüeso, D Calandria-Hernández, SR Gámiz-Fortis, MJ Esteban-Parra, and Y Castro-Díez. Extreme value analysis of precipitation series in the south of iberian peninsula. In *Universidad de Granada. Granada, Spain. AMS supported meetings. https://ams. confex. com/ams/pdfpapers/159994. pdf*, 2010.

[124] Charles W Sherman. Frequency and intensity of excessive rainfalls at boston, massachusetts. *Transactions of the American Society of Civil Engineers*, 95(1):951–960, 1931.

[125] Ven Te Chow et al. Hydrologic determination of waterway areas for the design of drainage structures in small drainage basins. Technical report, University of Illinois at Urbana Champaign, College of Engineering , 1962.

[126] Merrill M Bernard. Formulas for rainfall intensities of long duration. *Transactions of the American Society of Civil Engineers*, 96(1):592–606, 1932.

[127] JO Haerter, P Berg, and S Hagemann. Heavy rain intensity distributions on varying time scales and at different temperatures. *Journal of Geophysical Research: Atmospheres*, 115(D17), 2010.

[128] Vijay P Singh and Lan Zhang. Idf curves using the frank archimedean copula. *Journal of Hydrologic Engineering*, 12(6):651–662, 2007.

[129] Ankit Jain and Rochak Pandey. Progressive improvements in basic intensity-duration-frequency curves deriving approaches: A review. 2017.

[130] Abdul Qayoom Dar, Humairah Maqbool, and Syeedah Raazia. An empirical formula to estimate rainfall intensity in kupwara region of kashmir valley, j and k, india. In *MATEC Web of Conferences*, volume 57, page 03010. EDP Sciences, 2016.

[131] DW Pierce and DR Cayan. Downscaling humidity with localized constructed analogs (loca) over the conterminous united states. *Climate dynamics*, 47(1-2):411–431, 2016.

[132] Shivam Tripathi and Rao S Govindaraju. On selection of kernel parametes in relevance vector machines for hydrologic applications. *Stochastic Environmental Research and Risk Assessment*, 21(6):747–764, 2007.

[133] NOAA. Noaa atlas 14. `https://hdsc.nws.noaa.gov/hdsc/pfds/`, 2017. "[Online; accessed March-2019]".

[134] NASA. The nasa earth exchange global daily downscaled projections. `https://nex.nasa.gov/nex/projects/1356`, 2019. "[Online; accessed Feburary-2019]".

[135] Daniel S Wilks. Maximum likelihood estimation for the gamma distribution using data containing zeros. *Journal of Climate*, 3(12):1495–1501, 1990.

[136] Fabrizio Durante, Juan Fernández-Sánchez, and Carlo Sempi. *How to Prove Sklar's Theorem*, pages 85–90. Springer Berlin Heidelberg, Berlin, Heidelberg, 2013.

[137] L Zhang and Vijay P Singh. Bivariate rainfall frequency distributions using archimedean copulas. *Journal of Hydrology*, 332(1):93–109, 2007.

[138] Qiang Zhang, Jianfeng Li, and Vijay P Singh. Application of archimedean copulas in the analysis of the precipitation extremes: effects of precipitation changes. *Theoretical and applied climatology*, 107(1-2):255–264, 2012.

[139] Yang Wang, Chuanzhe Li, Jia Liu, Fuliang Yu, Qingtai Qiu, Jiyang Tian, and Mengjie Zhang. Multivariate analysis of joint probability of different rainfall frequencies based on copulas. *Water*, 9(3):198, 2017.

[140] Loris Foresti, Alexei Pozdnoukhov, Devis Tuia, and Mikhail Kanevski. Extreme precipitation modelling using geostatistics and machine learning algorithms. In *geoENV VII–Geostatistics for Environmental Applications*, pages 41–52. Springer, 2010.

[141] Thomas Vandal, Evan Kodra, and Auroop R Ganguly. Intercomparison of machine learning methods for statistical downscaling: The case of daily and extreme precipitation. *Theoretical and Applied Climatology*, pages 1–14, 2017.

[142] USGS. The us geological survey (usgs) geo data portal. `https://cida.usgs.gov/gdp/`, 2019. "[Online; accessed Feburary-2019]".